Stratocumulus predictions with a Large-Eddy Simulation Model

With DALES on cloud nine?

By

Floris Heuff

in partial fulfilment of the requirements for the degree of

Master of Science
in Geoscience and Remote Sensing

at the Delft University of Technology,
to be defended publicly on 28 January 2016.

Supervisor:	Dr S.R. De Roode	
Thesis committee:	Prof. Dr A.P. Siebesma	TU Delft
	Dr M. De Graaf	TU Delft

TUDelft

Abstract

In this study the prediction of stratocumulus occurrence by the Large-Eddy Simulation model DALES was investigated. The performance of DALES was compared with that of the large-scale weather model RACMO. A method was developed which can consistently initialise the model by assimilation of observations in addition to large-scale weather model results. This method was then applied to four days in winter on which stratocumulus occurred. The results were analysed with the use of the liquid water path (LWP) budget analysis, which analyses the contributions of the relevant processes to the LWP tendency. A sensitivity study was then conducted, which investigated the effects of uncertainties in the initialisation of the model by applying variations to the initialisation parameters that effect the LWP tendency.

DALES outperformed RACMO in predicting stratocumulus occurrence. The model results also showed to be robust to the applied variations, i.e. the stratocumulus did not rapidly dissolve. These variations can have a great effect on the LWP, however.

A model like DALES has a spin up time in which the fields grow from having small turbulent motions to being fully turbulent. Therefore a method was developed to initialise DALES with fully turbulent motions. The method was then applied to the Cold Air Outbreak case of January 31 2010. The results showed that initialising DALES in this way is successful, and that large scale structures were present at initialisation.

Table of Contents

1 General Introduction

"Aren't the clouds beautiful? They look like big balls of cotton... I could just lie here all day, and watch them drift by... If you use your imagination, you can see lots of things in the cloud formations... What do you think you see, Linus?"

"Well, those clouds up there look like the map of the British Honduras on the Caribbean... That cloud up there looks a little like the profile of Thomas Eakins, the famous painter and sculptor... And that group of clouds over there gives me the impression of the stoning of Stephen... I can see the apostle Paul standing there to one side..."

"Uh huh... That's very good... What do you see in the clouds, Charlie Brown?"

"Well, I was going to say I saw a ducky and a horsie, but I changed my mind!"

− Charles M. Schulz, The Complete Peanuts, Vol. 5: 1959-1960

Clouds come in many shapes and sizes, as Mr Schulz so pointedly described. They range from small tufts called cirrocumulus occurring at heights from five to twelve kilometres to enormous thunderclouds that span the entire troposphere. A schematic picture showing the different kinds is given in figure 1.1.

Clouds play a very important role in the climate system; they a have cooling effect by contributing a lot to the earth's albedo, reflecting a large portion of the incoming solar radiation back to space and thereby reducing the amount of energy reaching the earth's surface. On the other hand, clouds also absorb infrared radiation emitted by the earth's surface, trapping warmth in the atmosphere and increasing the greenhouse effect, giving them a warming effect as well.

This thesis focuses on one particular type of cloud called stratocumulus and the modelling thereof. Here in the Netherlands, stratocumulus is a very familiar cloud. The dreary, grey days the Netherlands are famous for are usually caused by these low-hanging clouds. The name of this type of cloud derives from the Latin words *stratus*, which means flattened layer, and *cumulus*, which means heap or mass. They occur as a distinct extensive layer or sheet of grey to white low clouds, in the shape of more or less regular clumps or patches often arranged in bands or rolls that lie across the wind and that can be accompanied by a weak drizzle. Typically, stratocumulus clouds occur over or near cold ocean surfaces. On average they cover about one fifth of the earth's surface on the annual mean. Their high frequency of occurrence, persistence and their large impact on the albedo make stratocumulus clouds of particular importance to the climate system (van der Dussen, 2015).

Many aspects of the behaviour of stratocumulus clouds are poorly understood, despite having a substantial research focus. On a basic level, this is because a stratocumulus cloud system is a tight coupling of radiation, turbulence and cloud microphysical processes occurring over a wide range of scales from millimetres to kilometres. (Wood, 2012). Modelling this is a difficult process, as conventional weather and climate models have a coarse resolution and because of this, processes that occur on smaller scales than the resolution of a cell, including the processes that control the formation and dissolving of clouds, will have to be parametrised. For example, the vertical resolution in these models is close to the depth of the stratocumulus layer itself. As a consequence of these difficulties, models have trouble representing stratocumulus clouds
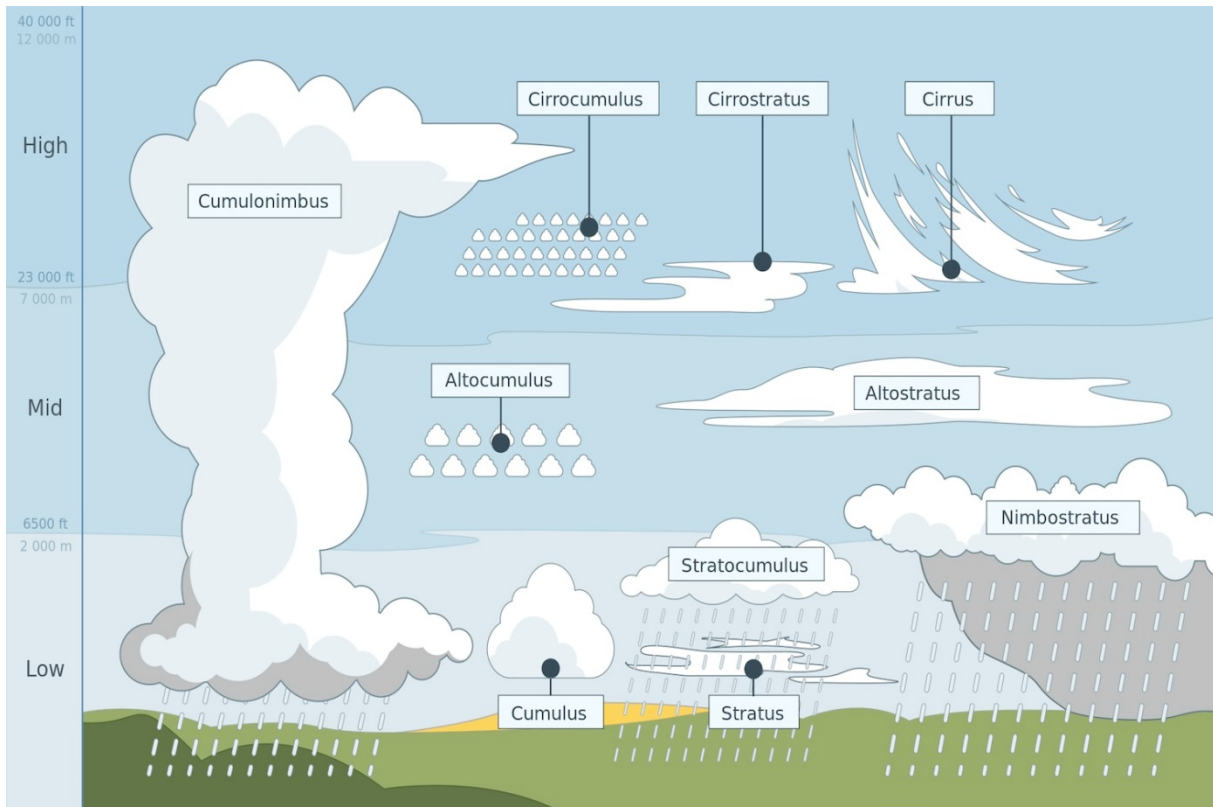

Figure 1.1 – The many types of clouds in the troposphere. *(Source:* http://sciencelearn.org.nz/Science-Stories/Navigating-Without-Instruments/Images/Cloud-types)

Large-eddy simulation (LES) models however seem to give better results when modelling stratocumulus clouds (Jacobs et al., 2012). An LES model has a much higher resolution, typically tens of metres in the horizontal and vertical directions, compared to other forecast models, which typically have a resolution of kilometres in the horizontally and hundreds of meters in the vertically. The higher resolution means many processes are calculated explicitly instead of being parameterised.

The finer resolution of LES models has a drawback: it is computationally very expensive to simulate very large domains, making it less feasible to forecast weather or to use it for global climate models. However, more insight into the processes controlling stratocumulus can be gained using an LES model. This in turn can aid in improving the parametrisation in large-scale models. Also, in this study it is assessed if the use of LES models for predicting the temporal evolution of stratocumulus clouds can be beneficial for the solar industry and for airports.

The solar industry could benefit greatly from better forecasts of stratocumulus clouds. The clouds can reflect more than fifty percent of the solar radiation back to space, which affects the amount of electricity that can be produced. A power plant tries to match their production to demand so as not to waste electricity. Solar power plants especially, have high variability in their capacity because of clouds,

which means they have to rely on buffers to help them overcome deficits. Having better and more reliable information regarding clouds helps anticipating their production capacity.

Research Aims

The aim of this thesis is to investigate the possibility of using an LES model to create better stratocumulus forecasts. This is a continuation of work done by Marijke Schuurbiers in 2014. In her work she found that the use of an LES model together with observational data has the potential to come to better stratocumulus predictions as compared to large scale weather models.

The questions addressed in this thesis are:

- Can the LES model be initialised by assimilating observations in addition to large scale weather model results?
- How do the LES results compare to the observational data?
- Does the LES model produce better predictions than the large scale weather model?
- How sensitive are the model's results to uncertainties in the observed initial vertical profiles?
- Which conditions like the inversion jumps and the cloud droplet concentration have the biggest influence on the evolution of the model?
- How does a simulation initialised with fully turbulent motions perform compared to a simulation that is not initialised with fully turbulent motions?

1.1 Outline

This thesis is divided into several chapters. Chapter 2 contains background information useful for readers that are unfamiliar with the topics discussed. Readers that are familiar with this topic can turn Chapter 2 aside and continue to Chapter 3, which describes the methods and the different data sources used to determine the initialisation profiles required to run the LES model. These methods are then applied to several days on which stratocumulus occurred. Chapter 4 investigates the effect of perturbing the system by small variations in the initial profiles. The emphasis herein is on the effect of the inversion jumps of heat and moisture. Chapter 5 investigates a method to initialise the LES model fully turbulent, by applying to a Cold Air Outbreak. A summary of the conclusions and recommendations are given in Chapter 6.

2 Theoretical Background

2.1 Structure of the Atmosphere
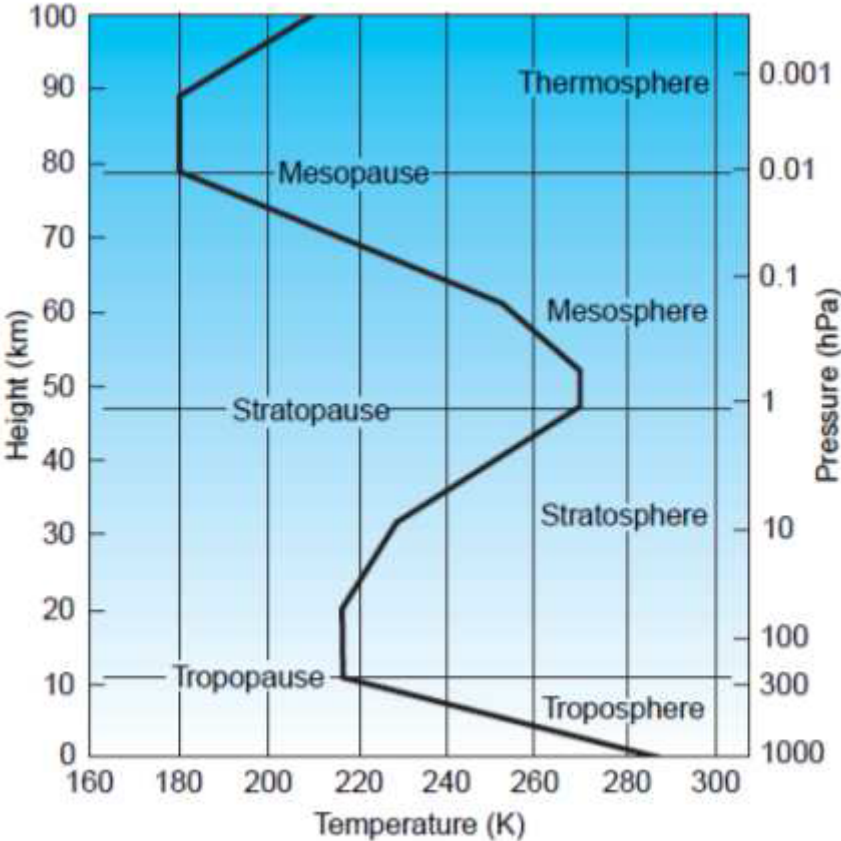
Figure 2.1 – **A typical mid-latitude vertical temperature profile as represented by the US Standard Atmosphere (Wallace and Hobbes, 2006).**

Figure 2.1 displays the different atmospheric layers that can be observed from the vertical temperature profile. Descending from the top of the atmosphere the first layer crossed is the *thermosphere*. It is here that very shortwave UV radiation is absorbed by oxygen heating the atmosphere. Moving down through the thermosphere, passing the *mesopause* at around 80 km, the temperature starts increasing again through the *mesosphere* to reach a maximum in the *stratopause*, at around 50 km. Here the medium wave length UV is absorbed by ozone. Underneath the stratopause we find the *stratosphere*, which is highly stratified and poorly mixed, as its name suggests, with long

residence times for particles ejected into it, for example by volcanos. Below the *tropopause* at around 8 to 16 km (depending on the season and latitude) is the *troposphere.* Moving down to the surface the temperature increases strongly. The troposphere contains around 85% of the atmosphere's mass and essentially all water vapour. Everything that is classified as weather happens within the troposphere (Marshall and Plumb, 2008).

The earth's surface is the bottom boundary of the troposphere. The part of the troposphere that is most affected by the surface is called the *atmospheric boundary layer (ABL).*The thickness of the boundary is quite variable. Normally it is around 1 to 2 km thick, which is the bottom 10% to 20% of the troposphere, but it can vary from a few meters to 4 km or more. On top of the boundary layer lies a stable layer called an *inversion,* which separates the boundary layer from the remainder of the troposphere above called the *free atmosphere.* The inversion prevents turbulence, aerosols and moisture to reach the free atmosphere, causing the free atmosphere to be relatively unaffected by the surface (Wallace and Hobbs, 2006).

2.2 Thermodynamics

To read this thesis some knowledge of variables and concepts that are being used in this type of research is required. The following section will explain and derive these to help the reader understand the different topics discussed.

2.2.1 Potential temperature

In atmospheric research one deals a lot with variables like pressure (i.e. high or low pressure systems), temperature (i.e. can I wear shorts today?) and humidity (i.e. Sahara desert or rain forest). Pressure and temperature are linked to each other through the ideal gas law:

$$p = \rho R_d T \tag{2.1}$$

With p the pressure, ρ the density of the gas in question, R_d the specific gas constant of dry air and T the absolute temperature in Kelvin.

Assuming the atmosphere is in equilibrium, which is called hydrostatic equilibrium, the pressure decreases as one goes up in the atmosphere. This expressed by the following equation:

$$dp = -\rho g \ dz \tag{2.2}$$

with g the gravitational constant.

The expression can be interpreted by thinking of the atmosphere as layers of air that are stacked onto each other. The stack at the bottom has to carry all the layers on top of it, thus feeling the largest pressure, while moving up each consecutive layer will feel less and less pressure. Now, if the density and the gravitational constant are known one could calculate the pressure, and indirectly the temperature, at different heights. However, this is not as straightforward as it seems, because of the density ρ in the expression. From the ideal gas law it follows that ρ depends on pressure:

$$\rho = \frac{p}{R_d T} \tag{2.3}$$

This means that the change in pressure with height is also influenced by the pressure itself. Thus, in order to find the pressure and temperature at different heights another step is needed.

Consider an air parcel at the earth's surface. During the day this parcel is warmed up by the sun acting to decrease its density causing it to rise up in the air, because it is warmer than its surroundings. This parcel obeys the first law of thermodynamics (conservation of energy) which is:

$$dQ = c_p dT - \frac{1}{\rho} dp \tag{2.4}$$

with c_p the constant pressure specific heat. Note that eq. 2.1 and eq. 2.2 have been used at this point. This law states that the change of energy dQ of the parcel by exchange of heat with its environment is related to the change in temperature and the change in pressure. Assuming the rising of the parcel is an adiabatic process, meaning no heat is exchanged with the environment at all, $dQ = 0$. Then, using the ideal gas law, ρ can be substituted giving the following expression:

$$\frac{dp}{p} = \frac{c_p}{R_d} \frac{dT}{T} \tag{2.5}$$

This differential equation can be rewritten, using $d \ln x = \frac{1}{x} dx$:

$$d \ln T - \frac{R_d}{c_p} d \ln p = 0 \ or \frac{T}{p^{\frac{R_d}{c_p}}} = constant \tag{2.6}$$

The potential temperature θ is defined as:

$$\theta = T \left(\frac{p_0}{p} \right)^{\frac{R_d}{c_p}} \tag{2.7}$$

The potential temperature θ is the temperature that a parcel with temperature T and pressure p will have if it is displaced adiabatically to a pressure p_0, a pressure value at a particular reference level. It then follows from eq. (2.7), using (2.6):

$$\frac{d\theta}{\theta} = \frac{dT}{T} - \frac{R_d}{c_p} \frac{dp}{p} = 0 \tag{2.8}$$

Unlike T, θ is conserved under adiabatic displacements. This means $\frac{d\theta}{dz} = 0$ and, using eq. 2.7 that

$$\frac{dT}{dz} = -\frac{g}{c_p} = -9.8 \frac{K}{km} \tag{2.9}$$

This is called the dry adiabatic lapse rate of the atmosphere.

Finally a relation is obtained that relates one of the atmospheric variables directly to height, assuming parcels can ascend and descend adiabatically.

The potential temperature provides an easy tool to determine whether a parcel will ascend or descend; if its potential temperature is higher than the potential temperature of the atmosphere it will ascend and if it is cooler it will descend.

2.2.2 Moisture

So far it was assumed that the atmosphere was free of water or moisture. This, of course, is not the case. Air contains water, both as vapour and as liquid. The amount of water in the atmosphere is expressed through the total specific humidity q_t, which is the sum of the specific humidity and liquid water specific humidity:

$$q_t = q_v + q_l \tag{2.10}$$

The specific humidity is the ratio of the mass of water vapour to the total mass (water vapour + liquid water + air) per unit volume. Similarly the liquid water specific humidity is the ratio of the mass of liquid water to the total mass.

The total specific humidity is a conserved quantity under phase transitions, meaning it remains the same. The potential temperature θ however is *not*. In the previous section the parcel was considered to

be dry, i.e. it contained no water. In the case it does contain water vapour this will condense when the parcel has cooled down enough during its ascend. The condensation of water vapour into liquid water releases energy into the air, warming up the parcel, increasing its temperature. dQ is no longer zero and instead equal to $dQ = L_v dq_l$, with L_v the latent heat of condensation. Similar to the derivation of the potential temperature the *liquid potential temperature* θ_l can be derived, which is given in its linear approximation by:

$$\theta_l = \theta - \frac{L_v}{c_p \Pi} q_l \tag{2.11}$$

It is easy to see that the liquid potential temperature is equal to the potential temperature when $q_l = 0$. The term with q_l accounts for the heat released by condensation. The benefit of using θ_l is that it is conserved under phase transitions.

2.3 Stratocumulus Clouds

The following section on stratocumulus clouds contains parts of the work of van der Dussen (2015).

2.3.1 Global stratocumulus occurrence

Stratocumulus clouds are the earth's most common cloud type and cover large parts of the globe. Approximately four-fifths of all stratocumuli are located over ocean regions. The low sea surface temperature in combination with large scale subsidence of relatively warmer air creates statically stable lower-tropospheric conditions, under which stratocumuli tend to form (Klein and Hartmann, 1993). These conditions are often found just off the coast in the subtropics and also for example sometimes over the North Sea, which is the area that is the focus of this study.

However, the stratocumulus occurrences in the subtropics are a fine example to illustrate their formation. The main catalyst behind this is the Hadley circulation. A schematic of this circulation is shown in Figure 2.2. This circulation is driven by the differential heating of the earth's surface by the sun. The equator receives most of the sun's energy while the poles receive the least, causing the surface temperature to be highest near the equator. This causes a mean uplift of the warm air up to 20 km that flows through the high troposphere pole wards. This relatively warm air descends in the subtropics, typically around 30° latitude. This descent of air is associated with persistent high-pressure systems.

The descending air is relatively warm compared to the air below, causing a thermal inversion. As explained in the previous section air with a potential temperature higher than its surroundings will start to rise. However, because of the warmer air descending from above, the potential temperature suddenly starts increasing at a certain height, acting as a lid that prevents the cooler air coming from below to ascend any further. This ascending air from the surface brings along moisture and when enough of it builds up under the inversion and the air becomes saturated, stratocumulus clouds can form just below.

2.3.2 Physics of Stratocumulus

Radiation

Stratocumulus clouds thicker than a hundred metre can be treated as a back body that emits infrared radiation according to Plancks's Law. This emission causes a large energy loss at the top of the cloud layer, since it absorbs less from the clear atmosphere above, resulting in a cooling tendency called cloud-top radiative cooling. It has two important effects that tend to thicken the cloud. First, it lowers the temperature of the cloud enhancing the condensation of water. Second, the cooling at the top destabilises the boundary because the air at the top gets heavier and starts sinking, which causes mixing by turbulence, not only by heating of the surface, but also by radiative cooling at the top (Lilly, 1968; Nicholls 1989; Bretheron et al., 1999). Therefore the air in a stratocumulus topped boundary layer is often well mixed. Because of the increased turbulence the moisture evaporated from the surface can easily reach the clouds thickening it.

As mentioned previously, stratocumulus clouds also interact with solar radiation Up to 80% (depending on the thickness) is reflected back into space, but a portion is absorbed as well, which warms the cloud. This compensates for the cooling during the day and therefore stratocumulus is often less thick during the day than during the night (Turton and Nicholls, 1987; Caldwell and Bretherton, 2009).
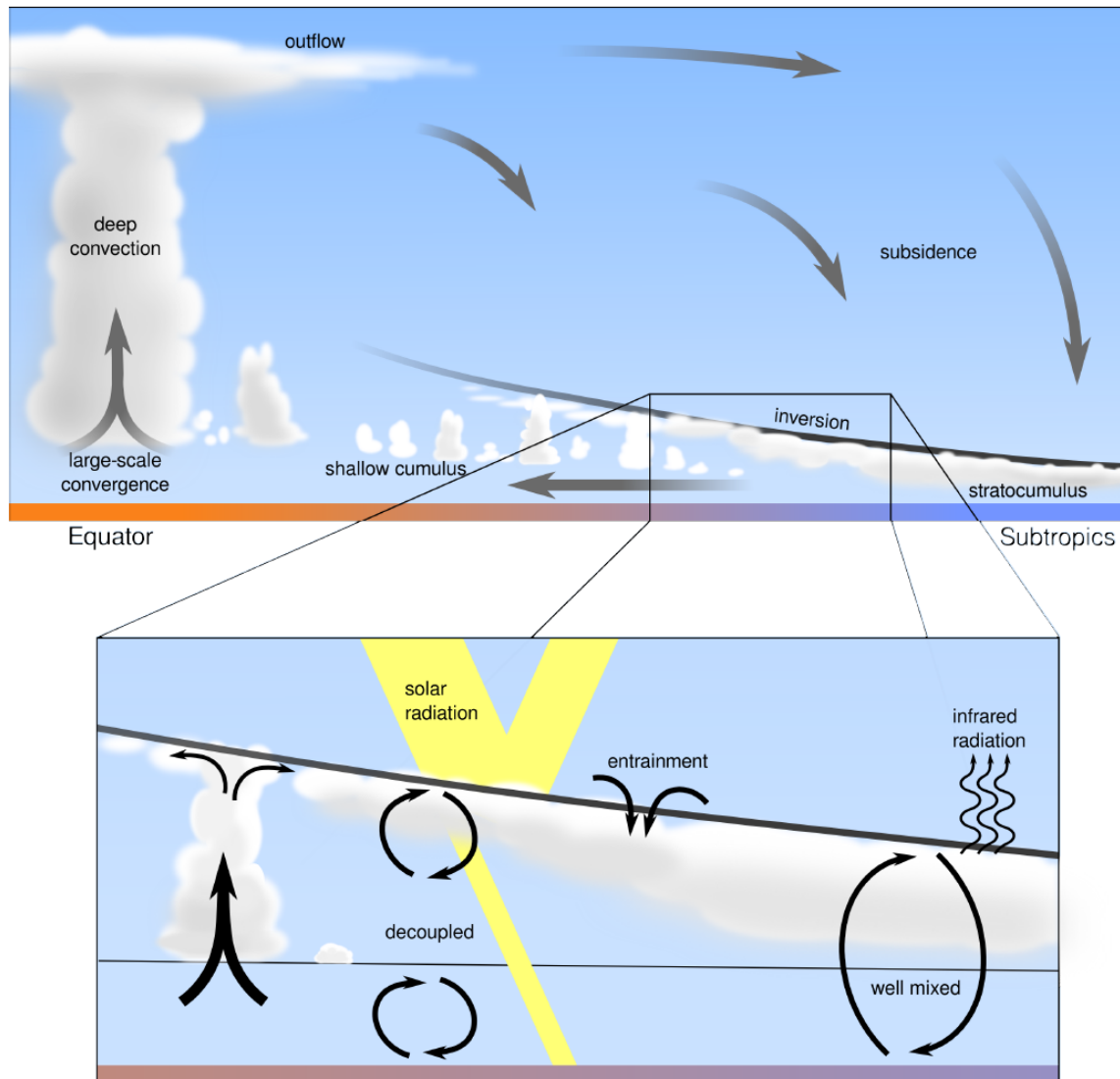

Figure 2.2 – A schematic representation of the Hadley circulation and the cloud types that typically occur within this large-scale circulation. The bottom panel zooms in on the stratocumulus regime within the Hadley circulation (Van der Dussen, 2015).

Entrainment

Despite the thermal inversion at the top, air from the free troposphere is still being dragged into the boundary layer due to the mixing turbulence. This is called entrainment. Entrainment increases the height of the boundary layer while also thickening the stratocumulus layer. It also has a cloud thinning effect, because the air being dragged in is usually warmer and drier than the air in the cloud. Of these two competing effects, the latter process usually dominates (Randall, 1984; de Roode et al., 2014). Enhanced entrainment is therefore often thought of as an important reason for the break-up of stratocumulus clouds. (Randall,1980; Deardorff, 1980a; de Roode and Duynkerke, 1997).

The rate of entrainment depends on many factors like the strength of the inversion, the radiative cooling, evaporative cooling and the turbulence of the cloud. (Nicholls and Turton, 1986; Moeng, 2000;

Stevens, 2002). This makes it difficult to model the entrainment rate. Also, the entrainment velocity is only a few $cm\ s^{-1}$ which makes it hard to accurately measure it (de Roode and Duynkerke, 1997; Faloona et al., 2005; Carman et al., 2012). Therefore entrainment remains an active field of research.

Microphysics

Stratocumulus clouds generate little precipitation because of their shallowness of only a few hundred metres. However, the slow descend of cloud droplets called sedimentation is important to the evolution of the stratocumulus layer, because it reduces the liquid water specific humidity near the cloud top. This reduces the potential for evaporative cooling when cloud air mixes with warm and dry free tropospheric air, which leads to a reduced entrainment rate (Stevens et al., 1998; Uchida et al., 2010). Therefore microphysics still plays an important role, albeit indirect, on the thickness of a stratocumulus cloud (Ackerman et al., 2004).

Decoupling

It was mentioned in the section on radiation that stratocumulus topped boundary layers are often well mixed. Through this mixing humidity is typically homogenously distributed with height through the boundary layer, especially for boundary layers where the inversion is located below one kilometre. However, if the boundary layer deepens due to entrainment, the mixing caused by cloud-top radiative cooling is no longer strong enough to mix the entirety of the boundary layer, which can cause the layer to separate into a stratocumulus layer at top that is mixed by radiative cooling and a sub cloud that is mixed by turbulence from the surface. Between the two layers a transition layer is formed with air that is relatively quiescent. This phenomenon is called decoupling. (Wyant et al., 1997; Park et al., 2004; Wood and Bretherton, 2004).

2.4 Large Eddy Simulation (LES)

The atmosphere is governed by a set of conservation equations for moisture, temperature, mass and momentum. The last two are governed by the so called Navier-Stokes equations. These equations describe the motion of a viscous fluid and are used to describe the physics of many things like ocean currents, air flow around a wing of an aircraft or, in this particular case, the weather.

2.4.1 Conservation of Mass

The conservation of mass is described in the continuity equation:

$$\frac{D\rho}{Dt} + \rho\overrightarrow{\nabla} \cdot \vec{u} = 0 \tag{2.12}$$

where $\vec{u}$ is the wind velocity vector, ρ the density and $\frac{D}{Dt}$ the Lagrangian derivative. Assuming that the air is incompressible this reduces to:

$$\overrightarrow{\nabla} \cdot \vec{u} = 0 \tag{2.13}$$

2.4.2 Conservation of Momentum

The momentum equations are given by:

$$\frac{D\vec{u}}{Dt} = \frac{\partial \vec{u}}{\partial t} + \vec{u} \cdot \overrightarrow{\nabla}\vec{u} = -\frac{1}{\rho_0}\overrightarrow{\nabla}p - 2\Omega \times \vec{u} + \vec{F}_u \tag{2.14}$$

where p is the pressure, Ω_i is the angular velocity vector representing the earth's rotation. $\vec{F}_u$ represents other forces on the momentum equation including gravity.

2.4.3 Conservation of temperature and moisture

The conservation equation for θ_l and q_t can be written as follows:

$$\frac{D\varphi}{Dt} = \frac{\partial \varphi}{\partial t} + \vec{u} \cdot \overrightarrow{\nabla}\varphi = S_\varphi \tag{2.15}$$

where φ is θ_l or q_t and S_φ the sink/source terms that may apply.

The problem with these equations is that they cannot be solved analytically and have to be solved using numerical methods. Ideally this would be done using a Direct Numerical Simulation (DNS), where the smallest scales are calculated directly. However, this is computationally too expensive which means a different method has to be used.

2.4.4 Filtered equations

An LES model is less computationally demanding, although still high compared to that of current weather forecast models. It uses a fine three-dimensional grid and deals with the problem of solving the conservation equations by dividing the problem into two parts. The first part is to explicitly solve the motions, often called eddies, which contain most of the turbulent energy and the transport of energy and moisture on a fine enough grid. The motions and transport that are smaller than grid resolution are filtered out of the conservation equations using a low-pass filter. The second part is to then solve these motions and transport using a sub-grid model. A schematic of this is shown in Figure 2.3. The first panel displays the turbulent atmosphere, containing both very large eddies and very small eddies. This atmosphere is modelled in the LES model on a grid, displayed in panel 2. The eddies smaller than the chosen resolution are modelled by the sub-grid, leaving only the large eddies to be solved numerically with the conservation equations, displayed in panel 3.
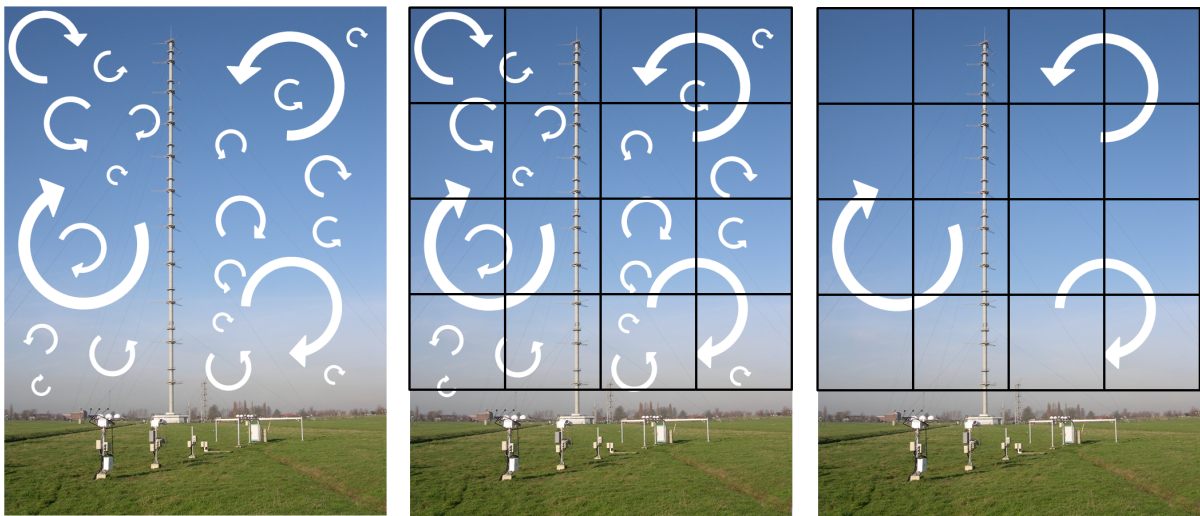

Figure 2.3 – Schematic of an LES model. Panel 1 displays the turbulent atmosphere with all scales present. The second panel displays the same atmosphere modelled in an LES model. Smaller scales than the grid resolution cannot be solved directly and will be solved in the sub-grid model. Panel 3 shows the large eddies that are solved directly.

The filtered equation for temperature and moisture is as follows, where $\tilde{\varphi}$ indicates a filtered variable.

$$\frac{\partial \tilde{\varphi}}{\partial t} = \underbrace{-\frac{1}{\rho_0}\overrightarrow{\nabla} \cdot \rho_0 \vec{\tilde{u}}\tilde{\varphi}}_{resolved} \underbrace{-\frac{1}{\rho_0}\overrightarrow{\nabla} \cdot \rho_0 \widetilde{\vec{u}^s\varphi^s}}_{sub-grid} - \underbrace{w\frac{\partial \tilde{\varphi}}{\partial z}}_{subsidence}$$
$$- \underbrace{\vec{u}_h \cdot \overrightarrow{\nabla}_h \varphi}_{LS\ advection} + \underbrace{\frac{1}{\tau}(\varphi - \langle\varphi\rangle)}_{relaxation} + \underbrace{S_\varphi}_{sources} \tag{2.16}$$

$$\frac{\partial \tilde{\vec{u}}}{\partial t} = \underbrace{-\frac{1}{\rho_0}\overrightarrow{\nabla} \cdot \rho_0 \vec{\tilde{u}}\tilde{\vec{u}}}_{resolved} \underbrace{-\frac{1}{\rho_0}\overrightarrow{\nabla} \cdot \rho_0 \widetilde{\vec{u}^s\vec{u}^s}}_{sub-grid} - \underbrace{w\frac{\partial \widetilde{\vec{u}_h}}{\partial z}}_{subsidence}$$
$$- \underbrace{\vec{u}_h \cdot \overrightarrow{\nabla}_h \vec{u}}_{LS\ advection} + \underbrace{\frac{1}{\tau}(\vec{u}_h - \langle\vec{u}_h\rangle)}_{relaxation} + \underset{sources}{\vec{F}_{\vec{u}}}$$
$$- \underbrace{2\Omega \times \left(\tilde{\vec{u}} - \vec{u}_g\right)}_{Coriolis\ \&\ LS\ pressure} - \underbrace{\overrightarrow{\nabla}\pi}_{pressure} - \underbrace{\frac{\tilde{\theta}_v - \langle\theta_v\rangle}{\langle\theta_v\rangle}g\hat{\vec{k}}}_{buoyancy} \tag{2.17}$$

In these equations h denotes the horizontal components. ρ is replaced by ρ_0, the density at the surface, according to the Boussinesq approximation, which assumes that the variation in the density is negligibly small. The first two terms in eq. (2.16) and (2.17) represent the turbulent transport on the resolved and sub-filter scale. The third and fourth term represent the vertical and horizontal components of transport on large scales. The fifth term is used to relax an LES state to a desired end state. This will be discussed in detail in Chapter 5. The Coriolis term in eq. (2.17) represents the large-scale pressure gradients. π is the modified pressure, written as $\pi = \frac{\tilde{p}-p_e}{\rho_0} + \frac{2}{3}e$, where $p - p_e$ is the pressure difference with the environment and e is the sub-grid kinetic energy. The buoyancy forces are represented through fluctuations in the virtual potential temperature θ_v. They only act in the vertical direction, which is indicated by $\hat{\vec{k}}$, the vertical unit vector.

By using these filtered conservation equations the computational cost is reduced by orders of magnitude compared to that of a DNS model. The ability of an LES model to capture the complex interaction between turbulence and clouds makes it a great tool to model stratocumulus clouds (Ackerman et al., 2009). Radiation, evaporative cooling and microphysical processes influencing turbulence are typically represented well. Also, an LES model is capable of capturing the sharp jumps in temperature and humidity at the inversion, which is so typical for stratocumulus (Stevens et al.,1999).

2.5 Data Sources

The following section covers the different data sources used to make initialise DALES. This includes some of the instruments used to measure the atmosphere.

2.5.1 The Cabauw Experimental Site for Atmospheric Research

In the centre of the Netherlands at $51.971° N, 4.927° E$ the Cabauw Experimental Site for Atmospheric Research (CESAR) is located, which is maintained by the Royal Netherlands Meteorological Institute (KNMI). The site houses a lot of instruments to monitor the atmosphere and land surface processes. Some of these instruments are attached to a 213 metre high tower that measures several atmospheric variables, like the temperature, humidity and wind at different heights. Other observations include clouds, aerosols, greenhouse gases, surface fluxes, hydrology and infra-sound.

This research makes use of the tower's measurements, a ceilometer that measures the cloud base, a pyrometer that measures the cloud cover and a microwave radiometer that measures the liquid water path.

The KNMI operates a LD-40 ceilometer, which is a LIDAR (LIght Detection and Ranging) system. Such a system transmits laser pulses vertically and measures the backscattered signal as a function of time. The strength of the return signal depends on the amount of particles in volume a certain distance away. The time interval between the transmission and the reception of the signal determines the distance. Each laser pulse results in a vertical profile of the particle concentration within the atmosphere. These profiles are usually averaged in order to increase the signal to noise ratio. (De Haij et al., 2007)

The presence of clouds or water droplets gives a very strong return signal compared to that of the background, which makes it easy to identify cloud heights. However, other particles in the atmosphere are just as easily detected, i.e. dust, rain, smoke, etc. and may cause false readings.

The NubiScope is a pyrometer, which has an infrared sensor. It scans the sky continuously measuring temperature. Scanning clouds in the sky generally shows significant temperature differences according to the height of the layer measured. Higher clouds principally show lower temperatures. The lowest temperature is measured in cloudless sky. In each layer the temperature increases from zenith to horizon. This „horizon-effect" is most noticeable in cloudless sky and nearly unnoticeable in low clouds. The NubiScope uses the information to obtain the correct relation of temperature and height and by doing so different types of cloud cover can be identified.[1]

The HATPRO is microwave radiometer that can estimate the liquid water path (LWP). The liquid water path is the integrated liquid water content with height. The radiometer measures the thermal radiation of the atmosphere. Depending on the selected frequency bands the emission of microwave radiation of different gasses, liquid water or ice crystals can be measured. The total emissivity of the atmosphere in the range from 20 to 60 GHz depends on the total amount of liquid water in the atmospheric column. From this the LWP can be estimated. [2]

2.5.2 Radiosonde

The radiosonde is a weather balloon released once a day at midnight at the KNMI measurement site de Bilt, which is located near Utrecht and about 30 km away from Cabauw. The weather balloon measures the temperature, humidity and pressure. The wind speed and direction are derived from its location and speed. Weather balloons can go as high as 17kilometre to 25 kilometre, so their measurements cover the entire troposphere. During the period of 2011-2012, the focus of this research, the weather balloon was released twice a day at midnight and noon.

2.5.3 RACMO

Variables required to run DALES that are not available from measurements are obtained from the regional atmospheric climate model (RACMO) which the KNMI runs daily in forecast mode. RACMO is initialised near Cabauw by an analysis from the European Centre for Medium-Range Weather Forecasts (ECMWF) and forced at the boundaries by an ECMWF forecast. ECMWF makes forecasts based on the data collected from radiosondes throughout Europe. The duration of such a simulation is only a few days in order to remain close to the analysis state with which the 3D RACMO forecast was initialised. (Neggers, et al., 2010). The grid column in RACMO that coincides with Cabauw is used in this work. RACMO provides many different variables, ranging from surface fluxes, to incoming radiation, to advection terms.

---

[1] src: http://nubiscope.eu/Desciption/description.html)

[2]   src: https://www.tropos.de/en/research/projects-infrastructures-technology/technology-at-tropos/remote-sensing/microwave-radiometer/)

3 Prescribing DALES by assimilating observations and regional weather forecast models.

3.1 Introduction

For this research the Dutch Atmospheric Large-Eddy Simulation (DALES) model is used (Heus et al., 2010). DALES requires several input files to start the simulation. These are simple text files that contain information on the state of the atmosphere. These profiles can be idealised profiles for academic cases or they can be based on actual measurements. One issue with the latter approach is that not all required variables (e.g. large scale forcings) and profiles (e.g. inversion height/strength) are available from measurements and therefore certain assumptions and interpolations have to be made. This chapter discusses the methods used to combine different measurements and data sets to create these profiles in a consistent manner. The developed method will then be applied to selected cases of stratocumulus occurrence. Finally, this chapter is concluded with a comparison of the DALES predictions with the results from RACMO and the measurements made at Cabauw.

3.2 Methodology

For this particular work DALES version 4.0 is used. The amount of files that are needed depends on the type of initialisation. The model can be used in different modes and has many add-ons which can be used or left out. For example one can choose to use time dependent or time independent fluxes, use different kind of microphysics schemes or radiation schemes.

Table 3.1 gives an overview of the required files and the variables prescribed in them. These variables are taken or have to be derived from the data sources mentioned earlier. An overview of the used variables is provided in Table 3.2. Additionally, in order to determine the inversion height the liquid water path and cloud base are used. The NubiScope is also mentioned, although it is not used for prescribing profiles. Instead it will be used to identify days on which stratocumulus occurred.

FILENAME	DESCRIPTION	VARIABLES PRESCRIBED
namoptions	Prescribes the different options available.	Domain size, grid size, runtime, date, etc.
prof.inp	Prescribes the atmospheric profile	$\theta_l, q_t, u, v, e_{12}$
ls_scale.inp	Prescribes the time-independent large scale forcings.	$u_{geo}, v_{geo}, \overline{w}, \theta_{l,adv}, q_{t,adv}$
scalar.inp	Prescribes time-independent large scale forcings for scalars	-
ls_flux.inp	Prescribes the time-dependent large scale forcing and time dependent surface fluxes	$u_{geo}, v_{geo}, \overline{w}, \theta_{l,adv}, q_{t,adv}$ $\theta_l\ (surface)$
ls_fluxsv.inp	Prescribes time-dependent large scale forcings for scalars and surface fluxes.	drizzle
backrad.inp	Prescribes the variables needed to calculate the radiation.	p, q_v, q_l, T, O_3
nudge.inp	Prescribes the nudging time and atmospheric profiles	$\theta_l, q_t, u, v, e_{12}, t_n$

Table 3.1 − **List of input files required to run DALES. The variables prescribed in each file are listed.**

Tower/Cabauw	$T, q_t, WS, WD, SWD, LWU, LHF, SHF$
RACMO	$p, T, q_v, q_l, u, v, u_{geo}, v_{geo}, \overline{w}, T_{adv}, q_{t,adv}$
Radiosonde	T, q_v, WS, WD
LD-40	z_b
HATPRO	LWP
NubiScope	$cloudcover$

Table 3.2 − **List of instruments and models used. For each source the variables provided by them is listed.**

3.2.1 Prescribing DALES profiles

namoptions

In appendix A a namoptions file can be found that belongs to the simulations performed. This file is used to configure the different options available in the model. These include the grid size, the domain size and the length of the simulation as well as the location, the time and date. Also different schemes for the calculation of radiation, the surface physics and microphysics can be selected. All available options can be found in the manual (Heus et al., 2010).

prof.inp

The initial state of the atmosphere needs to be specified at each height level by using the values of the liquid potential temperature (θ_l), the total specific humidity (q_t), the zonal and meridional wind components (u, v) and the initial subgrid turbulent kinetic energy (e_{12}). These profiles are determined using the measurements from CESAR and the results from RACMO, except the subgrid TKE, which is usually taken to be $1.0 \frac{m^2}{s^2}$ in the boundary layer.

Assuming the boundary layer is well mixed and that θ_l and q_t are constant up to the inversion, the mean values of θ_l and q_t as measured by the tower are used to determine the profile up to the inversion. Above the inversion the θ_l and q_t profiles are taken from RACMO. These profiles are interpolated linearly to estimate their values at the prescribed heights.

Both the tower data as well as the RACMO data provide the temperature. Therefore, first the temperature has to be converted to liquid potential temperature using eq. (2.11). In the case of RACMO this is straightforward as RACMO data contain pressure values and the liquid water specific humidity.

The tower does not have any pressure measurements, which is why the pressure is determined using the ideal gas law (eq. (2.1)) and the expression for hydrostatic equilibrium (eq. (2.2)). It is convenient to write the ideal gas law in terms of the virtual temperature T_v:

$$T_v = T(1 - q_l + 0.61q_v) \tag{3.1}$$

$$dp = -\frac{p}{R_d T_v} g \, dz \tag{3.2}$$

Since it is assumed that θ_l and q_t are constant up to the inversion, it is possible to derive the pressure profile iteratively with the surface pressure p_0 and T using eq. (3.2).

Using the expression (eq. (3.3)) for the saturation specific humidity the amount of water vapour and liquid water can be determined.

$$q_s(T, p) = \frac{R_d}{R_v} \frac{e_s(T)}{p} \tag{3.3}$$

with e_s the saturation vapour pressure (from the Clausius-Clapeyron relation) which is only dependent on temperature.

From the expression for the liquid water path (LWP) the inversion height can be calculated.

$$LWP = \int_{z_b}^{z_{inv}} \rho q_l dz \tag{3.4}$$

with ρ the density of the atmosphere.

The calculated moist adiabatic profile is integrated with height to the point the LWP matches the LWP measured by HATPRO. This gives the cloud layer thickness. Together with the cloud base measurement from LIDAR the inversion height is determined. Note that by using this method no radiosonde measurements are required to determine the inversion height.

The height at which the relative humidity ($RH = \frac{q_v}{q_s}$) reaches 100% and condensation occurs depends on both the temperature and the total specific humidity. This allows the user to slightly adjust the θ_l and/or q_t profiles to initialise DALES as close as possible to the measured cloud base height, while a certain amount of freedom remains to initialise the model, for example to investigate the effect of increasing the temperature and specific humidity slightly, while keeping the cloud base height at the same level.

ls_flux.inp and ls_fluxsv.inp

The geostrophic winds, the large scale subsidence and the large scale advection tendencies of θ_l and q_t prescribe the large scale forcings in the file ls_flux.inp. These profiles are taken from RACMO after conversion of T_{adv} to $\theta_{l,adv}$ and interpolated linearly to match the height profile. The x-gradient and y-gradient of q_t can also be specified here, but are not used here. These profiles are prescribed hourly.

The subsidence is derived from the vertical pressure velocity.

$$w_{subs} = -\frac{1}{\rho g} \omega \tag{3.5}$$

The ls_flux.inp file also prescribes the time-dependent surface fluxes. These include the surface pressure and depending on the surface scheme the latent and sensible heat flux (isurf=4 in namoptions) or the surface temperature (isurf=2). Here, the surface temperature is used. This surface scheme assumes that the surface is saturated with moisture.

The surface temperature and surface pressure are taken from the Cabauw measurements. The surface temperature is calculated from the long wave upward radiation (eq. (3.6)). Their values are prescribed hourly.

$$T = \left(\frac{LWU}{\sigma}\right)^{\frac{1}{4}} \tag{3.6}$$

The ls_fluxsv.inp can be used to prescribe large scale forcing for scalars. However, in this study the scalars, used for drizzle, are not subject to any large scale forcings and therefore set at zero.

backrad.inp

This file is used to calculate the radiation. It requires the pressure, water vapour specific humidity, liquid water specific humidity and temperature. These can be taken directly from RACMO without any conversion or interpolation. It also takes an ozone profile if so desired by the user.

nudge.inp

The nudge file can be used to steer the model to a certain final profile of the atmosphere. The use of this option will be discussed in Chapter 5.

3.2.2 Stratocumulus case selection criteria

In the work of Schuurbiers (2014) a method to detect stratocumulus under a strong thermal inversion was developed. The method used four criteria to select days on which stratocumulus occurred. They are listed in Table 3.3. The following section will explain the reasoning behind these criteria.

	Criterion	Selection	Source
	$LTS > 15\ K$	Inversion present	RACMO
	$\overline{w} < 0\ ms^{-1}$	Subsidence region	RACMO
	$z_b < 1\ km$	Low cloud base	Observation, RACMO
	$cc \geq 0.9$	Homogenous cloud	Observation, RACMO

Table 3.3 – **Criteria used to determine days on which stratocumulus occurred according to Schuurbiers (2014).**

As discussed in section 2.3 stratocumulus clouds occur under a strong thermal inversion. However, the tower at Cabauw does not have any measurements higher than 200 metre. The radiosonde measurements could be used instead, but those are only available at midnight and noon unfortunately. This leaves RACMO, which is initialised with radiosonde data, to check for time periods with strong inversions. This has one problem; the vertical resolution of RACMO is too coarse to accurately capture the inversion layer that is very shallow (typically between 20 – 50 m). Instead as an alternative the lower-tropospheric stability (LTS) is used to find strong inversion as a first criterion. The LTS is defined as the difference of the potential temperature between 700 hPa and 1000 hPa, which is approximately between 3 km and the earth's surface. A high LTS is likely to be associated with a strong inversion (Klein and Hartmann, 1993).

Usually the inversion is a result of subsidence. Therefore the second criterion is that the average vertical velocity has to be negative (downwards) between the surface and 3 km. The vertical velocity cannot be measured by any instruments and has to be taken from RACMO as well. Satisfaction of the first two criteria is indicative of stable weather conditions and thus excludes deep convection (unstable weather).

The third criterion that is used is the height of the cloud base. Stratocumulus clouds belong to low clouds with a base lower than 2 km. As noted in section 2.3.2 stratocumulus can be decoupled if the cloud base is between 1 and 2 km. Hence the selection aims to select cases which are initially well-mixed.

The final criterion is the cloud cover. Stratocumulus clouds are known for their uniformity and that the cloud fraction inside the stratocumulus is close to 1 (de Roode, 2004). Hence the criterion for a cloud cover of 0.9 or higher.

Applying these criteria resulted in a list of days in 2011 and 2012 on which stratocumulus occurred. A modified version of this list is shown in appendix B. The list contains the date and time of its occurrence and the length of time the stratocumulus persisted. Also, only days have been listed for which the required data is available. This list will be used to select particular cases based on time of year. A selection of cases in all seasons is preferred to investigate whether the method of initialisation can be used throughout the year.

3.3 Results

3.3.1 Selection

An issue that surfaced during the selection of the cases is that the RACMO selection criteria might be too stringent. Observations show that February 18 2011 has a persistent stratocumulus occurrence, however this not reflected in the list of Schuurbiers. Instead, on this day there are gaps in time where no stratocumulus is identified. More cases on different days were found which also had gaps in time. All gaps were caused by a violation of the RACMO criterion for subsidence. In weather models like RACMO the vertical velocity often has a big uncertainty associated with it, because of the way it is calculated; it is a residual term of the horizontal velocity components that balances the total flow in and out of the system. A slight modelling error in the horizontal velocities can cause the vertical velocity to switch signs, especially when the vertical velocity is small. Another consideration is the fact that the criterion averages up from 3 km down to the surface and not down to the top of the cloud layer, which could cause a negative vertical velocity above the cloud layer to be missed. For this reason criterion 2 is changed to vertical velocity of less than 1 $mm\ s^{-1}$. The LTS criterion 1 is also adjusted from larger than 15 K to larger than 12 K, because Klein and Hartmann (1993) still identified stratocumulus cases below 15 K, albeit with a frequency of occurrence of less than 20%. Days that do not have a significant period of stratocumulus around noon are excluded as well, because it is preferred to initialise simulations around this time to be able to compare the profiles with measurements made by the radiosonde. Table 3.4 lists the possible cases based on these adjusted criteria.

From the list of stratocumulus observations four cases have been selected, although all cases could have been used. These days are February 18 2011, November 6 2011, January 29 2012 and March 13 2012. It is noticeable that there are no days during late spring or summer that meet the set requirements. In an effort to find cases during late spring and summer criteria 1 and 2 are dropped entirely and criteria 3 and 4 are changed to be purely based on observations. These changes are motivated by the fact that there are known cases where stratocumulus is observed, but where RACMO simulates a clear sky (Schuurbiers, 2014). However, this brings along the risk that there is no strong inversion, that the stratocumulus layer is decoupled or that the atmosphere is unstable due to the absence of subsidence. These issues will be checked for in the results. A table of the additional dates in late spring and summer is shown in Table 3.5. The selected days are June 19 2011, June 25 2011, August 11 2011, June 3 2012 and July 31 2012. This brings to a total of nine cases.

Date	Time	Duration	Date	Time	Duration
18-2-2011	0:00	0:15:00	**26-12-2011**	12:30	0:10:20
28-2-2011	3:00	0:15:50	**27-12-2011**	5:10	0:10:40
1-3-2011	4:40	0:10:50	**29-1-2012**	10:40	0:14:40
5-3-2011	13:20	0:03:40	**5-3-2012**	13:30	0:03:00
20-9-2011	9:50	0:04:20	**13-3-2012**	9:30	1:07:40
17-10-2011	6:50	0:08:30	**28-4-2012**	12:00	0:09:10
6-11-2011	7:40	0:08:30	**24-10-2012**	8:50	0:08:00
7-11-2011	7:30	0:07:10	**25-10-2012**	14:00	0:03:00
10-11-2011	12:10	0:23:50	**12-11-2012**	9:20	0:04:50
13-11-2011	12:20	0:05:10	**13-11-2012**	13:10	0:05:10
21-12-2011	10:40	0:04:10	**19-11-2012**	12:10	0:03:10

Table 3.4 – List of days with possible stratocumulus occurrence according to the four selection criteria. Selected days are highlighted.

Date	Time	Duration	Date	Time	Duration
28-5-2011	13:00	0:10:40	**12-9-2011**	6:30	0:07:50
13-6-2011	0:30	0:14:20	**17-9-2011**	13:00	0:05:10
19-6-2011	10:30	0:08:20	**31-5-2012**	9:10	0:11:30
20-6-2011	13:30	0:04:00	**3-6-2012**	1:10	1:13:30
24-6-2011	22:40	1:05:40	**9-6-2012**	5:00	0:10:00
11-8-2011	10:40	0:23:50	**11-6-2012**	22:00	0:18:50
13-8-2011	11:40	0:05:10	**10-7-2012**	10:50	0:04:30
28-8-2011	10:00	0:04:10	**17-7-2012**	12:00	0:05:20
31-8-2011	8:10	0:07:00	**18-7-2012**	11:10	0:03:10
6-9-2011	9:50	0:13:20	**31-7-2012**	7:20	0:14:50
8-9-2011	5:40	0:09:20	**8-8-2012**	9:50	0:06:00
9-9-2011	4:20	0:18:10	**14-9-2012**	4:10	0:11:10

Table 3.5 – List of days with possible stratocumulus occurrence during late spring and summer based on just observations. Selected days are highlighted.

3.3.2 Initialisation

All simulations will be initialised at 12:00 UTC. This way the profiles created as described in the previous sections can be compared to the radiosonde measurements at the KNMI in de Bilt. De Bilt is located within 30 km of the Cabauw measurement site, so it is assumed that the profiles measured by the radiosonde are identical to atmospheric profile at Cabauw. The initialisation profiles for February 18 2011 are displayed in Figure 3.1. All other profiles can be found in appendix C. Table 3.6 gives an overview of all selected cases.
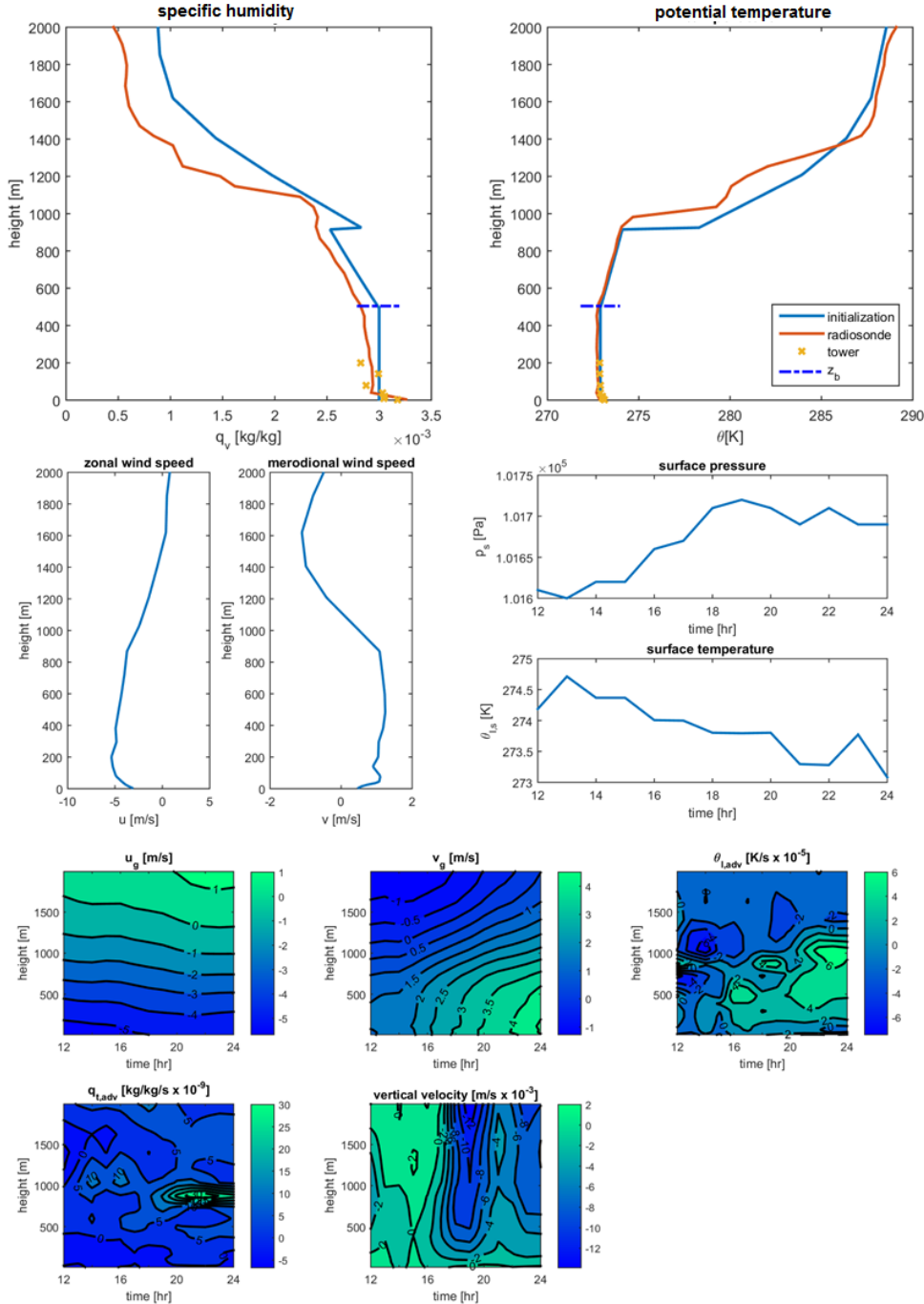
Figure 3.1 – The initialisation profiles for February 18 2011. Time is in UTC. The top panel shows a comparison of initialisation profiles with radiosonde measurements. The left panel is a comparison of the specific humidity q_v, the right panel of the potential temperature θ. The middle panel shows the wind vectors and the surface profiles. The bottom panel shows the forcings profiles. Time is in UTC.

Case Number and date:	LTS [K] RACMO	$\overline{w}$ [mm s^{-1}]		$\overline{w}\,(z > z_i)$ [mm s^{-1}]	cloud base [m]	thickness [m]	$\Delta\theta$ [K]	Δq_t [$\frac{g}{kg}$]
1: 2011-02-18	16.7	-0.42		0.12	504	412	5.41	-0.17
2: 2011-11-06	19.1	-0.055		-0.24	458	288	3.61	-0.60
3: 2012-01-29	13.8	-12.5		-15.1	495	266	3.01	-0.61
4: 2012-03-13	22.5	-7.6		-9.80	693	361	5.98	-1.21
Summer:								
5: 2011-06-19	10.5	8.7		8.1	358	424	1.15	-0.35
6: 2011-06-25	18.8	12.5		13.7	184	550	3.39	-2.50
7: 2011-08-11	11.8	27.2		36.3	906	405	4.47	-0.34
8: 2012-06-03	19.5	12.9		17.4	358	649	5.15	-1.31
9: 2012-07-31	12.3	7.0		8.70	946	533	2.83	-0.78

Table 3.6 – **List of the selected days with stratocumulus occurrence according to all four criteria (top) and criteria 3 and 4 (bottom). The left half shows selection criteria 1 and 2 and the Randall and Deardroff Criterion. The other half contains the vertical velocity above the inversion, the cloud base height, the cloud layer thickness and the inversion jumps.**

Figure 3.1 shows a comparison of the initial potential temperature and specific humidity with the radiosonde measurements on February 18. It shows that the prescribed θ profile coincides nicely with the one measured by the radiosonde; the cloud base is located at the same height as that found from the relative humidity measured by the radiosonde. The same holds for the inversion height. The prescribed q_v profile fits not equally well, although the cloud base and inversion layer are still recognisable by the peaks in the radiosonde profile. This is due to uncertainty in the humidity measurements made by the radiosonde (Schuurbiers, 2014). For the other runs similar plots can be found in appendix C. The other three cases selected with during winter (Nov 6, Jan 29, Mar 13) also follow the same profiles as the ones measured by the radiosonde.

In contrast to the four winter cases, the five summer cases (Jun 19, Jun 25, Aug 11, Jun 3, and Jul 31) do not coincide well with the radiosonde profiles. The θ profiles of these days are displayed in Figure 3.2. The most striking feature in the prescribed profile for June 19 is the negative θ jump at the inversion. This indicates there is no strong thermal inversion on this day. This is also found in the measurements made by the radiosonde. The θ profile of June 25 has a similar shape to that of the measurements, although it is offset slightly. The prescribed profile has a very low cloud base below 200 m and a small jump at the inversion; however, the cloud base height and inversion height are not noticeable in the measurements. Although June 3 follows the radiosonde profile relatively well compared to the other measurements, the radiosonde measurements show no inversion. August 11 and July 31 both have an inversion that does not coincide with the measurements. Also, in both cases the height of the cloud base is unclear; the measurements show two peaks which could indicate a two cloud layer system. This is further supported by the fact that the cloud base is close to one kilometre making it likely it is a decoupled system. For a decoupled system the developed methodology is not suitable, because the boundary layer is not well-mixed (Wood and Bretherton, 2004).

Table 3.6 reveals more issues with the selected days. The table contains the first two criteria for selection (based on RACMO and observations) together with the following variables calculated during the creation of the profiles: the vertical velocity above the inversion, the cloud base height, the cloud layer thickness and the inversion jumps. All values are calculated at 12:00 UTC. The values calculated for the winter cases are in line with the values that are expected for stratocumulus occurrence; a cloud bases below one kilometre, a shallow layer thickness between 200 and 500 m (Wood, 2012) and a negative vertical velocity above the inversion. February 18 is an exception with a small positive vertical velocity. However, when inspecting the values for the summer cases the values for the vertical velocity attract attention, because they are relatively large and positive, which implies that no large scale

subsidence is present. The values for the calculated cloud thickness are all larger than 400 m with June 25, June 3, and July 31 having a cloud thickness larger than 500 m. Also note that the selection criterion for the subsidence is violated in all five summer cases and that none of them would have been selected if this criterion had been used. The problems outlined for all five cases resulted in the omission of these cases for further analysis.
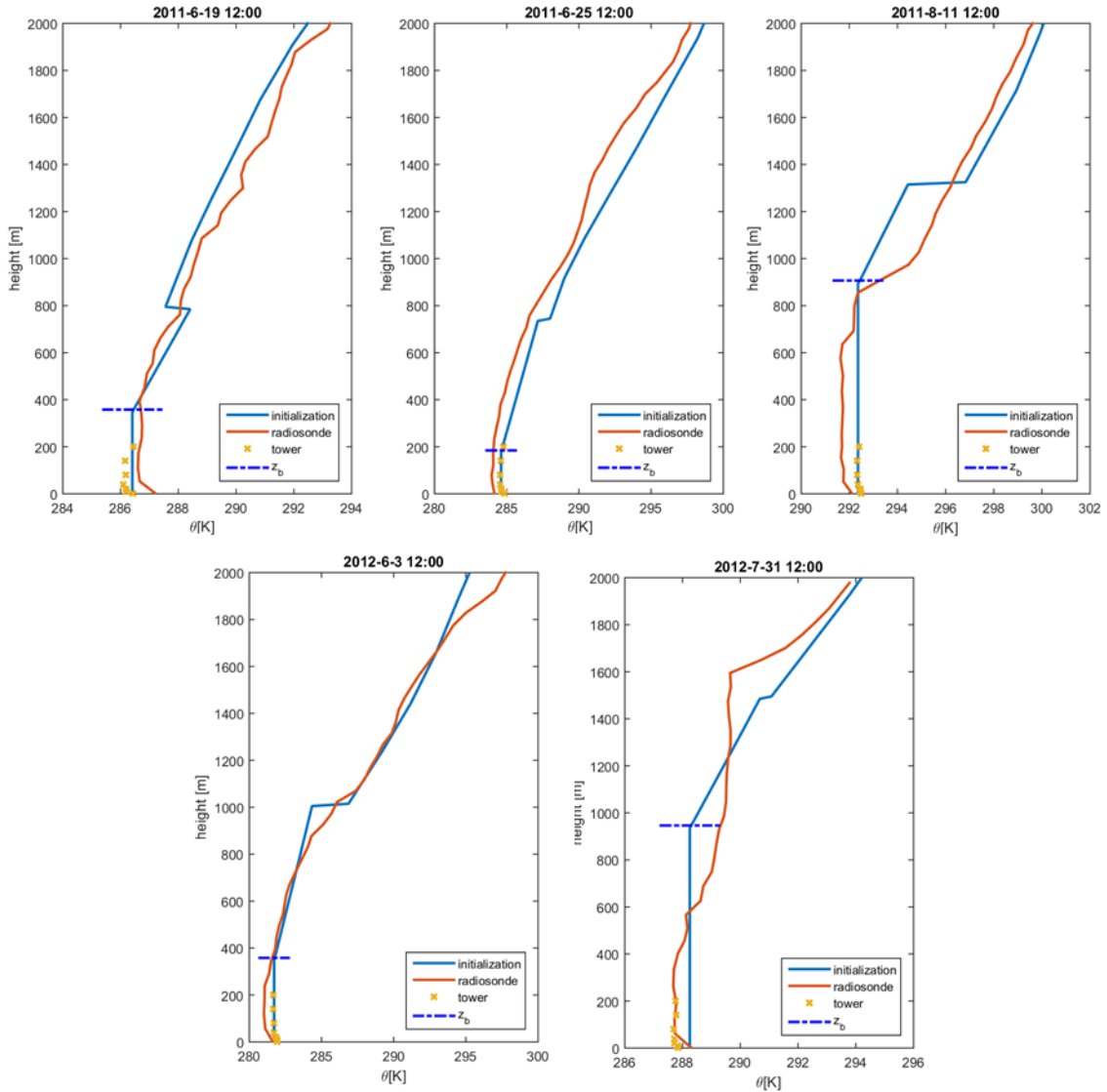

Figure 3.2 – Comparison of the **θ** profiles with radiosonde measurements of June 19, June 2015 and August 11 2011 and June 3 and July 31 2012. For all four days the initialisation profile and the measurements do not agree.

After making the profiles the buoyancy reversal criterion at the top of the cloud layer is checked. This has been suggested as one of the major mechanisms responsible for the dissolving of stratocumulus layers (Randall (1980) and Deardorff (1980a)). The thought behind this criterion is that under certain inversion conditions parcels being entrained can become negatively buoyant by mixing with the saturated air inside the clouds. Extra turbulent kinetic energy is generated by these sinking parcels causing additional entrainment. Such runaway entrainment could rapidly warm and dry the stratocumulus layer, causing it to break up. (Lilly, 1968). Randall (1980) and Deardorff (1980a) formulated a criterion for this process to occur. This criterion can be written in terms of the inversion jumps Δq_t and $\Delta \theta_l$:

23

$$\kappa = 1 + \frac{c_p}{L_v}\frac{\Delta\theta_l}{\Delta q_t} \tag{3.7}$$

where κ is the inversion stability parameter. Siems et al. (1990) showed that by using this equation the criterion can be written as $\kappa > \kappa_{BR} = 0.23$. However, van der Dussen et al. (2014) showed that the criterion alone is not sufficient for rapid cloud break up, but that it also depends on the turbulent humidity flux at the cloud base and the entrainment efficiency. Nevertheless, the cloud-thinning tendency due to entrainment increases rapidly with κ, making cloud breakup inevitable for sufficiently large values of κ. Therefore all runs are checked for this criterion to make sure the stratocumulus layer does not rapidly dissolve at the very start of the simulation.

For each run κ is determined (see Figure 3.3). All four winter cases lie well below the criterion and should not be affected by rapid thinning. (All case numbers can be found in Table 3.6).
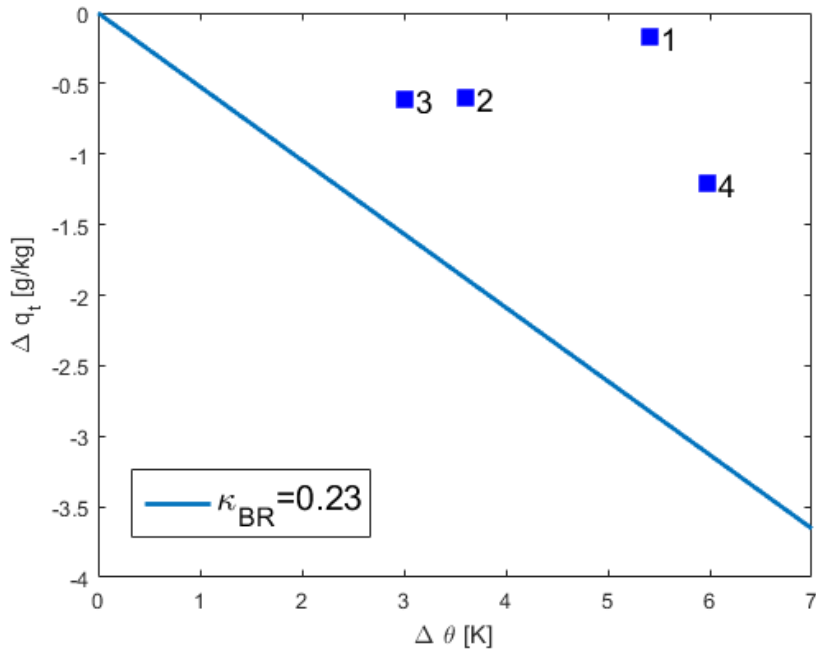
Figure 3.3 – Inversion stability parameter plot of the four winter cases. The blue line indicates the buoyancy reversal criterion formulated by Randall (1980) and Deardorff (1980a) with $\kappa_{br} = 0.23$.

3.3.3 DALES performance

All winter cases are initialised at 12:00 UTC on a domain of $6.4 \times 6.4 \times 2.0$ km^3 using a 120 x 120 x 200 grid. The duration of each simulation is 12 hours. Each run is then analysed by comparing the calculated cloud base, cloud top, liquid water path and shortwave down welling radiation (SWD) to those of the observations and RACMO. Recall that one of the aims of this study is to explore whether DALES produces better results than RACMO. Note that there are no measurements for the cloud top. The results are shown in Figure 3.4.

The results of the winter cases show that DALES successfully simulated stratocumulus and that the results are similar to the observations. Notably, DALES gives excellent results when estimating the cloud base and the SWD, which coincide very well with the observations. Especially February 18 2011 stands out; the cloud base, the LWP and cloud base all resemble the measurements closely. March 13 2012 also resembles the measurements well: The cloud base is only slightly higher than the measurements, which can be explained by the fact that DALES underestimates the LWP during the same period (13:00 – 16:00). In general the estimated LWP by DALES is the least accurate, which is noticeable on all four winter days. Especially on November 6 2011 and January 29 the results show large discrepancies in the LWP. On November 6 the measurements show a decrease in the values of the LWP between 12:00 and 16:00. DALES does not capture this decrease, but instead estimates a large increase. On January 29 DALES predicts a stratocumulus layer that grows thicker as the day progresses. This is not observed in the measurements; the LWP measured by HATPRO remains relatively constant throughout the day.

A possible cause for this thickening of the cloud layer is the assumption that the surface is saturated. For this reason the calculated latent heat flux is compared to the measurements. See Figure 3.4. It is clear that DALES does in fact overestimate the latent heat flux, but it does so for all four winter cases. This is unexpected, because on March 13 the LWP is underestimated. Clearly, the assumption that surface is saturated is not the (only) cause for the thickening of the cloud layer. More importantly, another problem surfaced; the latent heat surface flux persists after the sun has set. This is unexpected, because the latent heat flux is part of an energy balance driven by solar radiation (Stull, 1988).

Three out of four days show differences between the estimated and measured SWD at 12:00. February 18 is the only day on which the estimates and measurements are similar. These differences are not expected, because on all four days at 12:00 the estimated LWP is equal to the measured LWP and one would expect the SWD on these days to behave similarly to February 18.

It is clear from Figure 3.4 that DALES produced better results than RACMO on February 18. RACMO slightly overestimates the cloud base height, underestimates the LWP and has done a very poor job at predicting the incoming solar radiation. The latter is a reoccurring problem with RACMO; on the other three cases the estimated SWD is much too high as well, regardless of the estimated cloud base and LWP. On November 6 the cloud base and LWP estimated by RACMO match the measurements more closely than the cloud base and LWP estimated by DALES. Nevertheless, the SWD is still much too high. November 6 is the only day where RACMO performs better than DALES; on January 29 RACMO only finds a shallow layer of stratocumulus between 16:00 and 20:00, which dissolves afterwards. On March 13 RACMO finds a cloud base that is much lower than the cloud base measured by LIDAR.
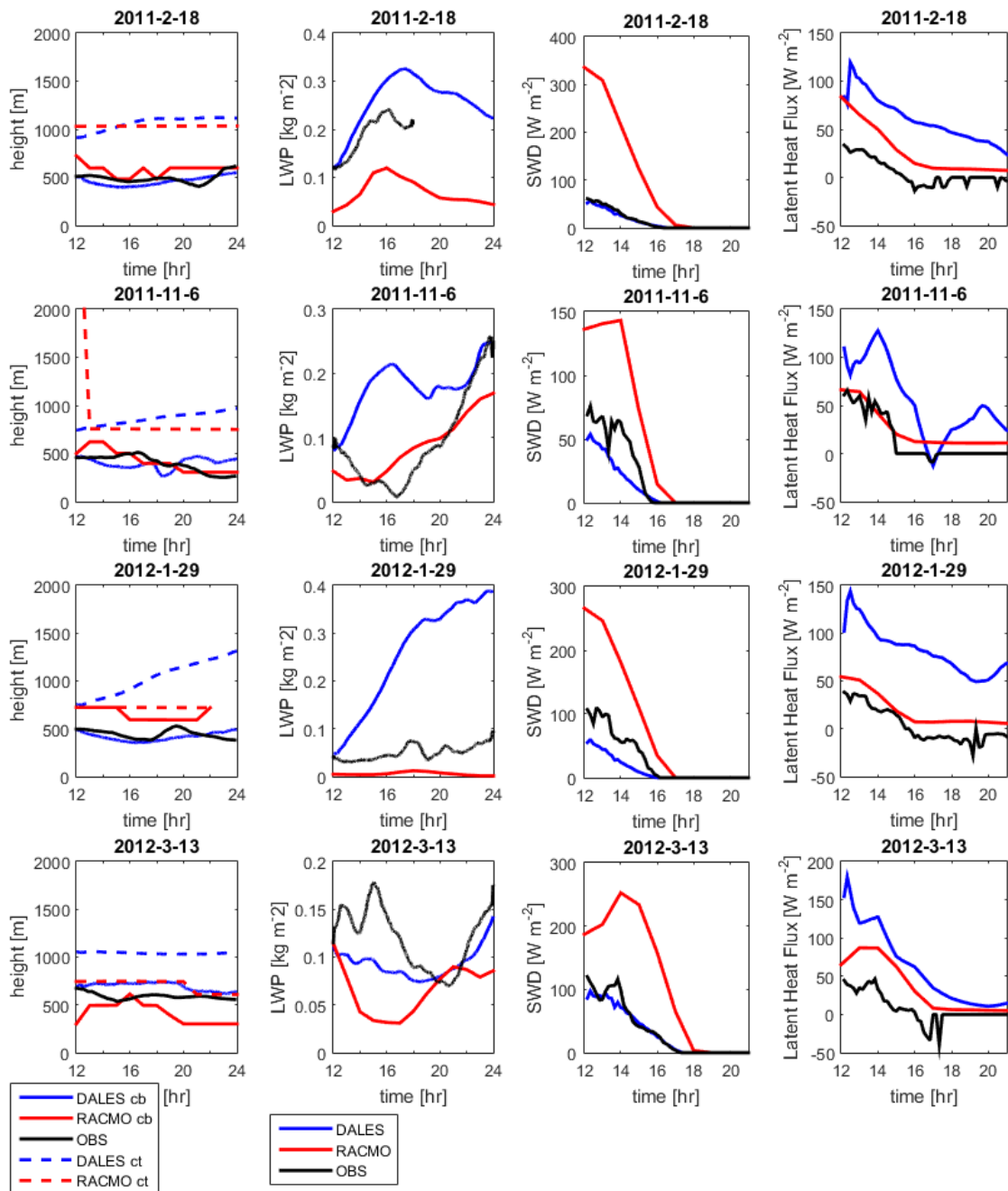
Figure 3.4 - Comparison of the cloud base (first panel), the LWP (second panel), shortwave down welling radiation (third panel) and latent heat flux (fourth panel) as calculated by DALES (blue) with RACMO (red) and observations (black) for the four selected winter cases. The left panel also includes the cloud top height calculated by DALES and RACMO. Time is in UTC.

26

3.4 Discussion and Conclusions

In this chapter the developed method to create DALES initialisation profiles in a consistent manner was described. Profiles are created by assimilating observations done at Cabauw in addition to RACMO results. It uses no radiosonde data, which makes it possible to initialise DALES at any time of day. The inversion height is estimated using the LWP and cloud base height measurements. This method was then applied to nine selected days on which stratocumulus were identified. The first four cases were selected based on four criteria for the LTS, subsidence, cloud cover and cloud base. All four of these cases occurred during winter or late fall, which led to a selection of five additional cases during summer based on just cloud cover and cloud base height.

All profiles were compared to radiosonde measurements. The four winter cases all agreed with the radiosonde measurements. The determined cloud layer thickness and cloud base height together with the presence of subsidence confirm that is very likely that a well-mixed stratocumulus-topped boundary layer was present on these days.

The developed method is not suitable for the selected summer days, because the assumption for a well-mixed stratocumulus-topped boundary layer was incorrect. The created profiles show large differences with the measured profiles. These radiosonde profiles are not corresponding to the typical profile of a well-mixed stratocumulus-topped boundary layer. The inversion heights for three cases (Jun 19, Jun 25, Jun 6) are hard to identify, because there is no clear inversion. The radiosonde profiles of the other two cases (Aug 11, July 31) show a possible decoupled system, because two temperature jumps can be distinguished from the radiosonde profiles. For these reasons the summer cases are not used any further. This also demonstrates that the selection based on just the cloud base height and cloud cover is not reliable to find days on which stratocumulus occurred, and that LTS and subsidence criteria are needed.

The remaining winter cases were then checked for the buoyancy reversal criterion, which is indicative of a strong potential for evaporative cooling at the cloud top and rapid cloud thinning. None of the cases satisfied this criterion and it is therefore expected that none of the winter days are affected by rapid cloud thinning.

In the final section the performance of DALES was analysed. The DALES model runs done on the four selected winter days were compared with observations done at Cabauw and results from RACMO. The DALES runs done at February 18 2011 and March 13 2012 DALES clearly outperformed RACMO, giving better results in predicting the evolution of the system. November 6 2011 and January 29 2012 performed less well in comparison; on both days DALES estimated an increase of the LWP where no such increase was observed. The DALES run on January 29 still produced better results than RACMO. However, November 6 did not. This could be explained by the fact that the stratocumulus occurrence that day is part of a large weather front, which large scale models generally predict well.

A possible reason for this thickening of the cloud layer is the used assumption that the surface is saturated. This assumption was used, because the interactive surface model for DALES is difficult to use and outside the scope of this research. Although DALES does in fact overestimate the latent heat flux, it overestimates it for all four cases, indicating that there are other causes for the thickening besides the saturation of the surface. A more detailed analysis of this assumption is done in the next chapter. There, variations are made to the latent heat flux and the effect these changes have on the LWP is investigated. More importantly, it was also noted that a considerable surface latent heat flux persisted after the sun had set, which is unexpected given the fact that the latent heat flux is driven by shortwave solar radiation. This most likely caused by the chosen surface scheme as well, which does not take radiation into account, but calculates the surface fluxes from the surface temperature.

The positive DALES results are reflected in the predictions for the incoming shortwave solar radiation; DALES estimates the incoming radiation very accurately. For February 18 and March 13, the

incoming radiation is almost equal to the measured values. RACMO is notably bad at predicting the incoming radiation, finding values that are two to three times higher than the measured values. However, the SWD has a notable feature; at 12:00 the difference between the SWD estimated by DALES and the measurements is different for all four winter days. This is unexpected, because on all four days LWP matches the measurements. A possible explanation for this is the effect that the cleanness of the air has on the optical thickness of the cloud. In the next chapter this is further investigated.

4 Factors controlling the formation and dissipation of stratocumulus clouds

4.1 Introduction

In the following section a method called LWP Budget Analysis (van der Dussen et al., 2014) is used. This method enables one to analyse the contribution of the relevant processes to the LWP tendency. The change of the LWP in time is determined by processes such as the entrainment, the subsidence and the absorbed radiation. For example it is easy to understand that a cloud will dissolve if the only process at work is the sun warming the cloud, but that a cloud will tend to thicken if moisture is added to the system. By inspecting these elements individually it is easier to identify what caused a possible change in the behaviour of the cloud system.

This method is used to investigate the stratocumulus cases discussed in the previous chapter in more detail and gain more understanding of the relevant processes controlling the formation and dissipation of stratocumulus. The contribution of the large scale advection to the LWP will receive some extra attention to make sure this term does not dominate all other LWP contributions. Otherwise there is little benefit in the use of a model like DALES for the predication of stratocumulus.

The differences discussed in the previous chapter are investigated by a sensitivity analysis that focusses on the effect of varying the inversion jumps for temperature and humidity, the droplet concentration and the latent heat surface flux. All have uncertainties attached to them, which will be discussed further down. The droplet concentration is related to the cleanness of air, which was mentioned as a possible cause for the difference observed in the estimated SWD. Particles in the air serve as condensation nuclei for water droplets. If the air is clean, it contains fewer particles and fewer water droplets can form. The latent heat surface flux was also mentioned in the previous chapter as a possible cause for the incorrect estimation of the LWP.

4.2 Theory

For a well-mixed stratocumulus-topped boundary layer q_l^t is a function of q_t and θ_l and the inversion height z_i (Randall 1984).

$$\frac{\partial q_l^t}{\partial t} = \frac{\partial q_l^t}{\partial q_t}\frac{\partial q_t}{\partial t} + \frac{\partial q_l^t}{\partial \theta_l}\frac{\partial \theta_l}{\partial t} + \frac{\partial q_l^t}{\partial z_i}\frac{\partial z_i}{\partial t} \tag{4.1}$$

Using the trapezoidal rule, q_l^t can be related to the LWP assuming q_l varies approximately linearly with height in the cloud:

$$\frac{\partial q_l}{\partial z} = -\Gamma_{q_l} \tag{4.2}$$

$$LWP = \int_0^\infty \rho q_l dz \approx \frac{1}{2}\rho h q_l^t \tag{4.3}$$

Here ρ is the density of the air and h is the thickness of the cloud layer. Γ_{q_l} is the lapse rate of the liquid water specific humidity. Integration of the lapse rate gives:

$$q_l^t = -\Gamma_{q_l} h \tag{4.4}$$

such that the LWP can be written as:

$$\frac{\partial LWP}{\partial t} = -\frac{1}{2}\frac{\partial}{\partial t}\left(\rho \Gamma_{q_l} h^2\right) \approx \rho h \frac{\partial q_l^t}{\partial t} \tag{4.5}$$

This can be rewritten to:

$$\frac{1}{\rho h}\frac{\partial LWP}{\partial t} = \eta\frac{\partial q_t}{\partial t} - \Pi\gamma\eta\frac{\partial \theta_l}{\partial t} - \Gamma_{q_l}[w_e + \overline{w}(z_i)] \tag{4.6}$$

with

$$\frac{\partial q_l^t}{\partial q_t} = \eta \tag{4.7}$$

$$\frac{\partial q_l^t}{\partial \theta_l} = -\Pi\gamma\eta \tag{4.8}$$

$$\eta = \left(1 + \frac{L_v\gamma}{c_p}\right)^{-1} \tag{4.9}$$

The factor η accounts for the latent heat release and uptake associated with the condensation and evaporation of liquid water and depends mainly on temperature. $\gamma = \frac{\partial q_s}{\partial T}$ is the change of the saturation specific humidity with temperature.

The time derivatives of q_t and θ_l are governed by their Reynolds-averaged budget equations:

$$\frac{\partial q_t}{\partial t} = -\frac{\partial \overline{w'q_t'}}{\partial z} - \boldsymbol{v}\cdot\nabla\, q_t - \frac{\partial P}{\partial z} \tag{4.10}$$

$$\frac{\partial \theta_l}{\partial t} = -\frac{\partial \overline{w'\theta_l'}}{\partial z} - \boldsymbol{v} \cdot \nabla \, \theta_l - \frac{1}{\Pi} \frac{\partial F_{rad}}{\partial z} + \frac{L_v}{c_p \Pi} \frac{\partial P}{\partial z} \tag{4.11}$$

They include the effects of precipitation P $(m \, s^{-1})$ and net radiative fluxes F_{rad} $(K \, ms^{-1})$. The overbars have been omitted for notional convenience, except for the turbulent fluxes.

The change of the inversion height with time is related to the entrainment rate and subsidence as follows:

$$\frac{\partial z_i}{\partial t} = w_e + \overline{w}(z_i) - u_h \cdot \nabla_h z_i \tag{4.12}$$

When assuming a well-mixed atmosphere, eq. (4.10) and (4.11) are straightforward to integrate from cloud base height, denoted by a superscript b, to the cloud top resulting in

$$h\frac{\partial q_t}{\partial t} = w_e \Delta q_t + \overline{w'q_t'}^b - \int_{z_b}^{z_t} \frac{\partial q_{t,adv}}{\partial t} dz - \delta P \tag{4.13}$$

$$h\frac{\partial \theta_l}{\partial t} = w_e \Delta \theta_l + \overline{w'\theta_l'}^b - \int_{z_b}^{z_t} \frac{\partial q_{t,adv}}{\partial t} dz - \frac{1}{\Pi} \delta F_{rad} + \frac{L_v}{c_p \Pi} \delta P \tag{4.14}$$

Through the use of the flux-jump relation $(\overline{w'\phi'}^t = -w_e \Delta \phi)$ the fluxes at the top of the inversion are related to the entrainment and inversion jumps. δ indicates the difference between cloud top and cloud base.

$\mathbf{v} \cdot \nabla q_t$ and $\mathbf{v} \cdot \nabla \theta_l$ are the large scale advection terms. If it is assumed that the model moves along with the mean large scale wind or if one assumes horizontal homogeneity then these terms are zero. In this study the model is at a fixed position and these terms have to be accounted for.
The advection terms in the LES model are taken from the tendencies provided by RACMO:

$$\int_{z_b}^{z_t} \boldsymbol{v} \cdot \nabla \, \theta_l = \int_{z_b}^{z_t} \frac{\partial \theta_{l,adv}}{\partial t} dz \tag{4.15}$$

$$\int_{z_b}^{z_t} \boldsymbol{v} \cdot \nabla \, q_t = \int_{z_b}^{z_t} \frac{\partial q_{t,adv}}{\partial t} dz \tag{4.16}$$

4.3 Methodology

4.3.1 Budget equation

When substituting all the derived quantities in the previous section into the relation for $\frac{\partial LWP}{\partial t}$ an equation is obtained that can be easily split into different contributions for the total LWP tendency:

$$Ent = \rho w_e (\eta \Delta q_t - \Pi \gamma \eta \Delta \theta_l - h \Gamma_{q_l}) \tag{4.17}$$

$$Base = \rho \eta (\overline{w'q_t'}^b - \Pi \gamma \overline{w'\theta_l'}^b) \tag{4.18}$$

$$Rad = \rho \eta \gamma \delta F_{rad} \tag{4.19}$$

$$Prec = -\rho \delta P \tag{4.20}$$

$$Subs = -\rho h \Gamma_{q_l} \overline{w}(z_i) \tag{4.21}$$

$$Adv = \frac{1}{h}(\eta \int_{z_b}^{z_i} \frac{\partial q_{t,adv}}{\partial t} - \eta\gamma\Pi \int_{z_b}^{z_i} \frac{\partial \theta_{l,adv}}{\partial t}) \tag{4.22}$$

$$\frac{\partial LWP}{\partial t} = Ent + Base + Rad + Prec + Subs + Adv \tag{4.23}$$

To evaluate the different contributions the cloud base and the top have to be determined from DALES results. For stratocumulus the cloud base is defined as the minimum height where the slab averaged cloud fraction exceeds 0.4. The top of the inversion is taken as the cloud top. The lower and upper boundaries of the inversion layer are determined using the profile of the variance of θ_l,

$$z_i^+ = z, where \; \overline{\theta_l'^2} = 0.05 \max(\theta_l'^2) \; and \; z > z_{max} \tag{4.24}$$

$$z_i^- = z, where \; \overline{\theta_l'^2} = 0.05 \max(\theta_l'^2) \; and \; z < z_{max} \tag{4.25}$$

Linear interpolation is used between grid levels to determine z_i^+ and z_i^-. By using these values and the cloud base height all variables in the budget equation can be evaluated using output from DALES.

4.3.2 Perturbation of the system

Three out of six contributions to the LWP tendency can be influenced by changing parameters in the model. These are the entrainment, the base and the precipitation contributions.

The entrainment contribution depends on the inversion jumps for q_t and θ_l. These are varied by changing the temperature and humidity profiles used above the inversion, which either increases or decreases the jumps. To estimate the role of the radiation forcing, the entrainment rate w_e can be crudely approximated in terms of the net radiative fluxes δF_{rad} and the liquid potential temperature $\Delta\theta_l$ (Stevens et al., 2005):

$$w_e = A\frac{\delta F_{rad}}{\Delta\theta_l} \tag{4.26}$$

Here A is the entrainment efficiency which is in the order of unity. Substituting this relation into the flux jump relations gives:

$$\overline{w'q_t'}^t = -\Delta q_t A\frac{\delta F_{rad}}{\Delta\theta_l} \tag{4.27}$$

$$\overline{w'\theta_l'}^t = -A \; \delta F_{rad} \tag{4.28}$$

Eq. (4.27) shows that the humidity flux at the top is inversely proportional to the $\Delta\theta_l$ jump, meaning that by increasing the temperature jump, the humidity flux is inhibited. The second relation shows that the temperature flux at the top is independent of the temperature jump. From these two relations it is therefore expected that changing the temperature jump will influence the humidity flux at the top of the cloud layer, but that the temperature flux will remain relatively unchanged.

The base contribution can be influenced by varying the surface fluxes. A simple modification to the code is made which allows one to scale the calculated latent and sensible heat flux.

Finally the precipitation contribution can be influenced by changing the raindrop number concentration. The precipitation is inversely proportional to the droplet concentration. DALES uses advanced schemes to calculate the precipitation (see Heus et al., 2010). However the inverse proportionality remains. This effect is known as the second indirect aerosol effect (Albrechts, 1989).

Aerosols serve as condensation nuclei on which cloud droplets form. As water droplets grow at some point they will become too heavy and fall down as rain. However, if the aerosol concentration increases more water droplets will form that are on average smaller in size. These droplets are lighter and reduce the precipitation efficiency thereby extending the lifetime of clouds. Clean air contains less aerosols while unclean air contains more.

4.4 Results

The results are split into two parts. The first section will introduce the LWP budget analysis with a detailed description of its application to February 18 2011. February 18 was the best performing winter case and will serve as a reference. It will also help the reader to understand what the budget analysis entails. The second part will focus on the sensitivity analysis. The LWP budget analysis is also used here to investigate the effect of the applied variations to the initialisation parameters on the LWP tendencies.

The application of variations to the inversion jumps, the surface fluxes and the number of cloud droplets is motivated by the fact that there are uncertainties in the values of these quantities. The inversion jumps are not prescribed directly; the magnitude of the jumps is determined by calculating the difference between the tower measurements and the RACMO results above the inversion. RACMO has an inherit uncertainty in its vertical profiles due to its coarse resolution, which averages $100 - 200$ m around the inversion height. Currently it not possible to measure the inversion jumps directly

Another uncertainty is the cleanness of the air, i.e. the amount of aerosols the air contains. So far the number of cloud droplets was set at $100 \ cm^{-3}$, which is a standard value. No measurements were available to determine more representative values. However, varying this value within a range of values that is typically observed in stratocumulus should give insight into the effect this has on the LWP tendency.

Finally, DALES assumes that the surface is saturated, which is likely to overestimate the latent heat flux. A better surface module for DALES is ready to use, but because the scope of the research is on the LWP tendency, and in particular the effects of the initialization of atmospheric properties, there was no time left to consider the soil moisture effect on the latent heat fluxes. The effect of the latter is has to be acknowledged however and therefore some simplified experiments have been performed in with the magnitude of the maximum possible latent heat flux (i.e. for a saturated surface) systematically decreased.

4.4.1   Budget Analysis of February 18 2011

The LWP tendency of February 18 2011 and its different contributions are shown in Figure 4.1. The figure shows that the LWP tendency (thick black line) determined using Eq. (4.23) agrees well with the actual LWP tendency (dotted black line). Notably, the actual LWP tendency is smoother than the sum of the contributions. The following paragraph will explain the effect each of the contributions has on the LWP tendency.

The simulation starts at 12:00 UTC. At this time the LWP tendency is dominated by the contributions of the radiation, the entrainment and the base fluxes. The contribution of the radiation to the LWP tendency is positive and causes the stratocumulus layer to thicken. This contribution increases as the day progresses; during the day the longwave radiative cooling is offset by the sun heating the stratocumulus layer, which has a thinning effect on the clouds reducing the LWP tendency. This warming effect decreases until the sun sets at 17:00. The radiation contribution to LWP tendency is solely due to longwave radiative cooling from this point on.

The increase of radiative cooling also increases the production of turbulence in the cloud layer, which increases the entrainment and turbulent fluxes (eq. (4.26)) at the stratocumulus base. The entrainment contribution is negative, thereby having a thinning effect on the cloud. The base fluxes are positive and cause the stratocumulus layer to thicken. The base contribution reaches a maximum value around 17:00, the same time the sun sets. After this time the base contributions diminish. This can be attributed to an increase of the subsidence, which was relatively small in the first five hours. It starts

negative, is slightly positive between 14:00 and 16:00 and then becomes negative again. The subsidence has a thinning effect, because it pushes the top of the cloud layer down (van der Dussen, 2013).

The thickening of the cloud that happens during the first couple of hours triggers precipitation. The precipitation has a thinning tendency. It keeps increasing until 17:30 (see Figure 4.1), which is around the same time the LWP reaches its maximum (see Figure 3.4). At that point the LWP starts decreasing. The precipitation contribution also diminishes in this period. The feedback of the LWP on the generation of precipitation acts as a buffering mechanism, levelling out variations of the LWP on timescales of several hours (van der Dussen, 2013).

The advection contribution is relatively small, has a thickening effect and is almost constant during the entire simulation. Advection can have a thinning or thickening tendency depending on the large scale moisture and temperature tendencies. If for example a lot of dry air is entering the domain, the advection will have a thinning tendency. What is important to note is that the advection term is relatively small and that it does not dominate the other contributions. This is found in the other three cases as well, indicating it does in fact make sense to use a model like DALES.
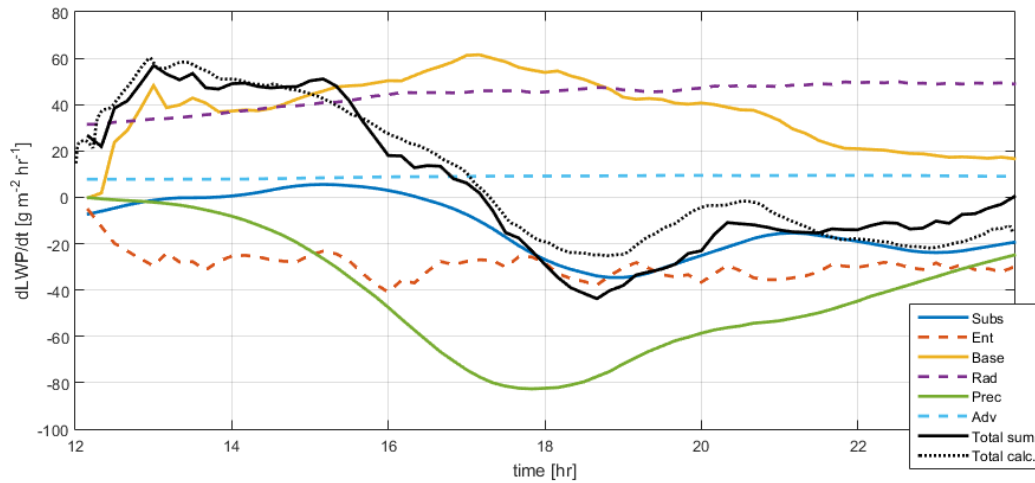
Figure 4.1 – **The tendency of the liquid water path as of a function of time (dotted black line) determined by DALES for February 18 2011, together with the six different contributions according to Eq. (4.23). The thick black line is the sum of the different contributions. Time is in UTC.**

4.4.2 Sensitivity Analysis

Now that the reader is more familiar with the budget analysis it is used to investigate the variations applied to the initial parameters. An overview of the changes is given in Table 4.1 and Table 4.2, resulting in a total of 11 additional simulations for each day; four runs with changes to the inversion jumps, four runs with changes to the cloud droplet density and three runs which have their q_t surface flux reduced. The variations in the number of cloud droplets and the latent heat flux are the same for all four days. The inversion jump variations are slightly different per day.

ID	Jumps	Number of cloud droplets cm^{-3})	Latent heat flux factor
000	$\Delta q_t = -1.7 \times 10^{-4}$ $\Delta\theta_l = 5.4\ K$	100	1
001	$\Delta q_t = -1 \times 10^{-4}$ $\Delta\theta_l = 2\ K$	100	1
002	$\Delta q_t = -1 \times 10^{-4}$ $\Delta\theta_l = 8\ K$	100	1
003	$\Delta q_t = -3 \times 10^{-3}$ $\Delta\theta_l = 2\ K$	100	1
004	$\Delta q_t = -3 \times 10^{-3}$ $\Delta\theta_l = 8\ K$	100	1
010	$\Delta q_t = -1.7 \times 10^{-4}$ $\Delta\theta_l = 5.4\ K$	50	1
020	$\Delta q_t = -1.7 \times 10^{-4}$ $\Delta\theta_l = 5.4\ K$	75	1
030	$\Delta q_t = -1.7 \times 10^{-4}$ $\Delta\theta_l = 5.4\ K$	150	1
040	$\Delta q_t = -1.7 \times 10^{-4}$ $\Delta\theta_l = 5.4\ K$	200	1
100	$\Delta q_t = -1.7 \times 10^{-4}$ $\Delta\theta_l = 5.4\ K$	100	0.25
200	$\Delta q_t = -1.7 \times 10^{-4}$ $\Delta\theta_l = 5.4\ K$	100	0.5
300	$\Delta q_t = -1.7 \times 10^{-4}$ $\Delta\theta_l = 5.4\ K$	100	0.75

Table 4.1 – Runs performed on February 18 2011, together with the variations applied to each individual run. The reference run is ID 000.

ID	2011-11-06	2012-01-29	2012-03-13
000	$\Delta q_t = -6.0 \times 10^{-4}$ $\Delta\theta_l = 3.6\ K$	$\Delta q_t = -6.1 \times 10^{-4}$ $\Delta\theta_l = 3\ K$	$\Delta q_t = -12 \times 10^{-4}$ $\Delta\theta_l = 5.7\ K$
001	$\Delta q_t = -1 \times 10^{-4}$ $\Delta\theta_l = 2\ K$	$\Delta q_t = -1 \times 10^{-4}$ $\Delta\theta_l = 2\ K$	$\Delta q_t = -1 \times 10^{-4}$ $\Delta\theta_l = 2\ K$
002	$\Delta q_t = -1 \times 10^{-4}$ $\Delta\theta_l = 8\ K$	$\Delta q_t = -1 \times 10^{-4}$ $\Delta\theta_l = 8\ K$	$\Delta q_t = -1 \times 10^{-4}$ $\Delta\theta_l = 8\ K$
003	$\Delta q_t = -4 \times 10^{-3}$ $\Delta\theta_l = 2\ K$	$\Delta q_t = -5 \times 10^{-3}$ $\Delta\theta_l = 2\ K$	$\Delta q_t = -2 \times 10^{-3}$ $\Delta\theta_l = 2\ K$
004	$\Delta q_t = -4 \times 10^{-3}$ $\Delta\theta_l = 8\ K$	$\Delta q_t = -5 \times 10^{-3}$ $\Delta\theta_l = 8\ K$	$\Delta q_t = -2 \times 10^{-3}$ $\Delta\theta_l = 8\ K$

Table 4.2 – Variations in inversion jumps used for November 6 2011, January 29 2012 and March 13 2012.

First the variations in inversion jumps will be discussed. In Figure 4.2 - Figure 4.5 the effects of these changes can be seen together with the LWP for all four days. The subsidence, radiation and advection tendencies are not displayed, because they vary very little compared to the other three tendencies. In the legend a small (large) Δq_t jump is indicated by wet (dry) and a small (large) $\Delta\theta_l$ jump is indicated by cold (warm).

Comparing the four days one thing stands out: The application of the variations to the inversion jumps has little effect of the sum of LWP tendencies. This is also reflected in the total LWP, which varies slightly in magnitude. The entrainment contribution to the LWP tendency is affected by the change in inversion jumps (eq. (4.17)), but is compensated by the base tendency. This can be explained by the fact that the θ_l flux and q_t flux behave approximately linearly with height between the surface and the inversion height in a well-mixed boundary layer (Wallace and Hobbs, 2006). For example, an increase of the q_t flux at the top of the stratocumulus layer caused by a larger Δq_t jump (eq. (4.27)), will also increase the q_t flux at the base of the stratocumulus layer, albeit it slightly less due to the linear relation. This causes the layer to slightly thicken, as was already observed in plots of the LWP. If the layer grows sufficiently thick due to this small offset and enough rainwater can form, the precipitation tendency starts increasing significantly, which has a thinning effect on the cloud layer.

The simulations performed with a large Δq_t jump and small $\Delta\theta_l$ jump (ID 003) attract attention, because of the large, fluctuating entrainment tendencies. The jumps all satisfy the buoyancy reversal criterion, which causes enhanced entrainment. On February 18 the increase in base tendencies is enough to compensate this effect, however, on November 6 and March 13 this enhanced entrainment leads to rapid thinning of the cloud layer. January 29 is the exception and is not affected.

January 29 does stand out though: The entrainment tendency in run 001 starts varying significantly after 21:00. The cause for this variation is the fact that the inversion disappears around that time and the boundary layer increases in height. The height dependency of the entrainment tendency (eq. (4.17)) causes the entrainment contribution to blow up. This prompted more investigation into using two small jumps and revealed that by choosing small jumps there is the risk that inversion is not strong enough and that the boundary layer can grow. Although not very noticeable, something similar happened on March 13 (ID 001). The defined jumps were not large enough for a strong inversion and the inversion quickly disappeared. However, a very strong inversion lay at 1200 m and the growth was halted. This is also the reason that run 001 on March 13 is the only run with this ID that has the largest reduction in LWP.

Finally, on February 18 and November 6 the runs with a large Δq_t and large $\Delta\theta_l$ (ID 004) also stand out. The jumps are so large that the entrainment tendency cannot be compensated by the base tendency. This thins the stratocumulus, which is very clear on November 6 where the LWP is reduced significantly.
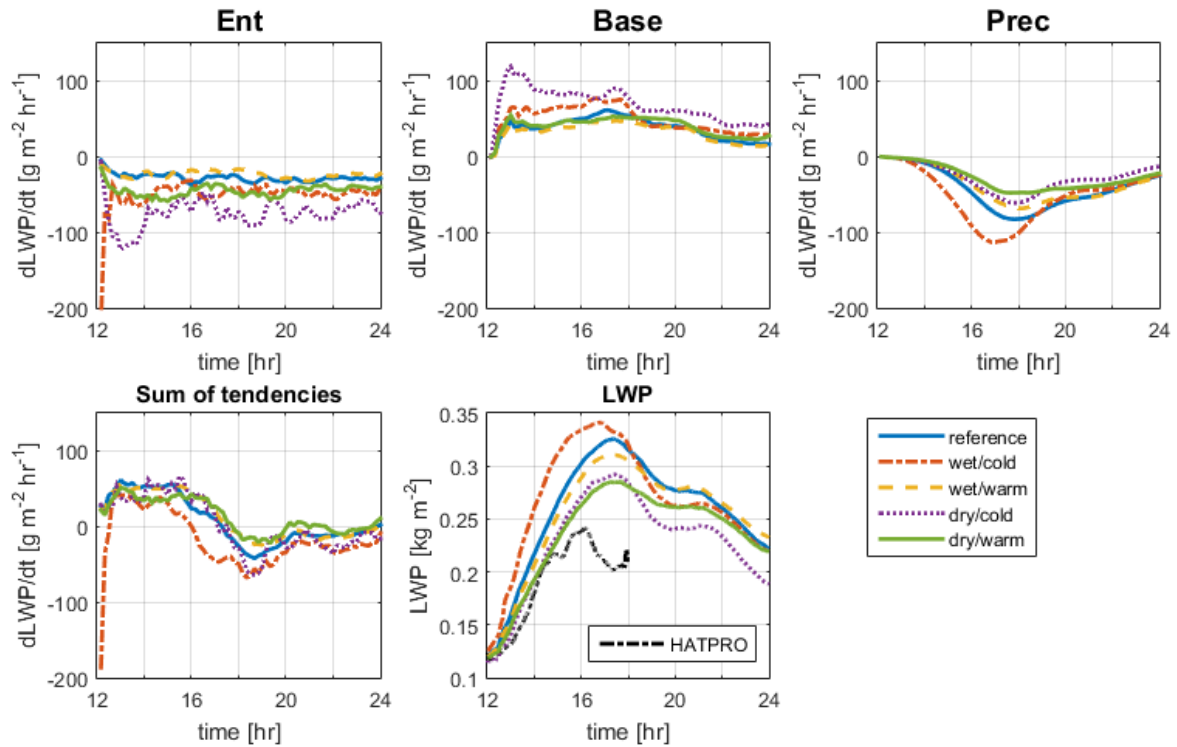
Figure 4.2 - The individual LWP tendencies for variations in the inversion jumps on February 18 2011. The legend indicates the run ID, which can be found in Table 4.3. The bottom right panel shows the estimated cloud LWP, together with the measured values. Time is in UTC.
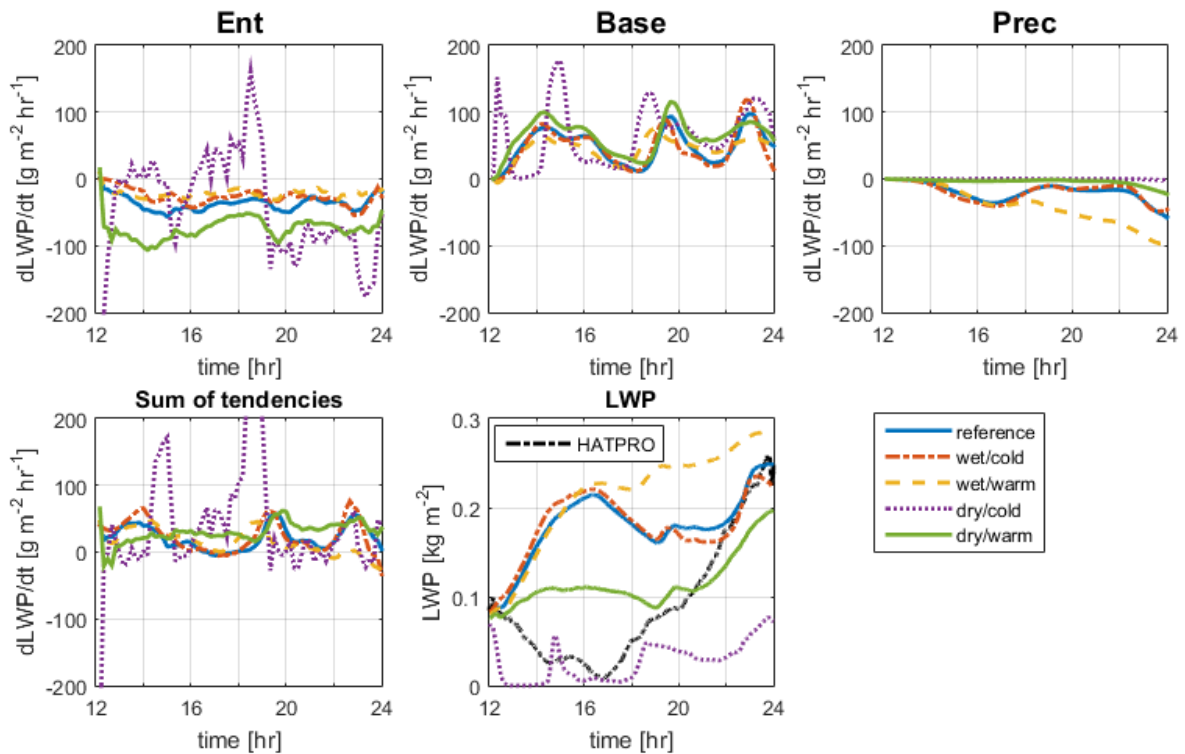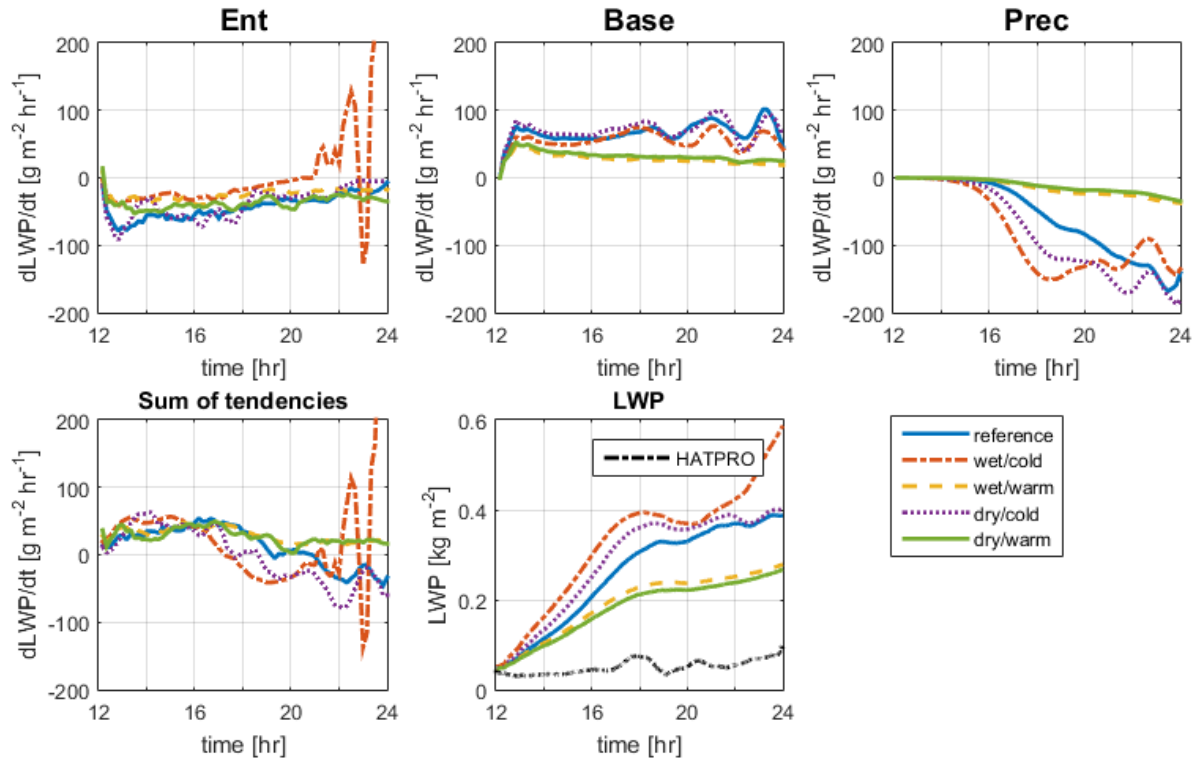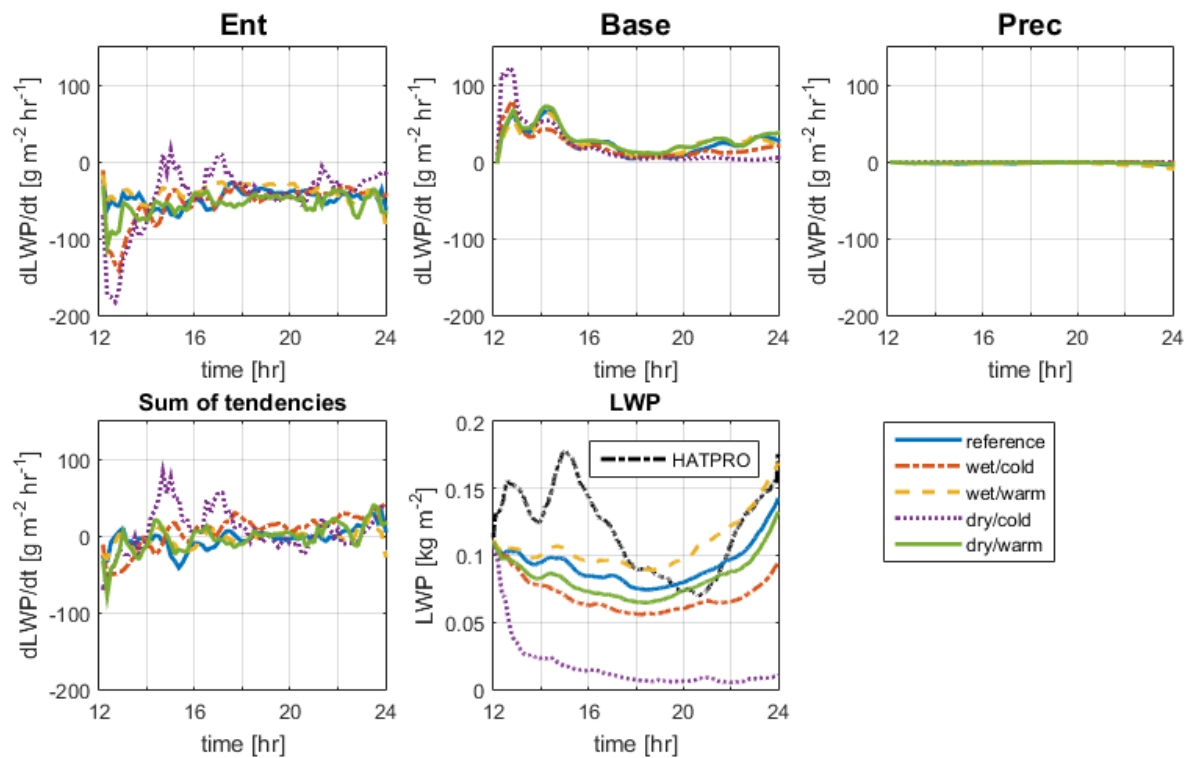

Figure 4.3 - The individual LWP tendencies for variations in the inversion jumps on November 6 2011. The legend indicates the used jumps, which can be found in Table 4.3. The bottom right panel shows the estimated cloud LWP, together with the measured values. Time is in UTC.

Figure 4.4 - The individual LWP tendencies for variations in the inversion jumps on January 29 2012. The legend indicates the used jumps, which can be found in Table 4.3. The bottom right panel shows the estimated cloud LWP, together with the measured values. Time is in UTC.

Figure 4.5 - The individual LWP tendencies for variations in the inversion jumps on March 13 2012. The legend indicates the used jumps, which can be found in Table 4.3. The bottom right panel shows the estimated cloud LWP, together with the measured values. Time is in UTC.

A similar analysis is done after changing the amount of cloud condensation nuclei present in the atmosphere, indicated by the number of cloud droplets N_c. The results are shown in Figure 4.6 - Figure 4.9.

As expected the precipitation tendency is greatly affected by the change of N_c. The LWP reduction by drizzle is largest for the lowest number of cloud droplets and smallest for the highest number of cloud droplets. March 13 is the least affected by the changes in N_c, where there is only a notable precipitation tendency for the lowest number of cloud droplets ($N_c = 50 \ cm^{-3}$). The total LWP is therefore also the least changed. For the three other days the total LWP is greatly affected. Notably, on February 18, for the run with $N_c = 50 \ cm^{-3}$ the LWP closely matches the LWP measured by HATPRO. The base tendencies show slight changes due to changes of number of cloud droplets. This is caused by a change of the θ_l fluxes and q_t fluxes due to the large increase of the precipitation flux. Recall from eq. (4.20), that the precipitation tendency is estimated by the difference of the precipitation flux at the cloud top and the cloud base. Above the clouds this flux is zero meaning that the precipitation tendency is directly linked to the precipitation flux at the cloud base. The entrainment rate is expected to go down for large drizzle rates (van der Dussen, 2014), however, this is only noticeable on November 6, on the other three days the entrainment tendencies stayed relatively similar.

In Chapter 3 it was mentioned that the number of cloud droplets could affect the amount of solar radiation reaching the earth's surface and that this might a possible explanation for the observed difference between measurements and the DALES estimates of the SWD at 12:00. This is due to the inverse proportionally of the effective radius of droplets on the optical thickness. The changes to the SWD due to the changes in N_c are displayed in Figure 4.10. It is clear that changing N_c had the expected effect on the SWD: If the number of cloud droplets is increased, the cloud layer is more reflective and less radiation reaches the surface. If the number of cloud droplets is decreased the opposite is observed; the cloud layer is more transparent and the radiation reaching the surface is increased. Mark that the change of the SWD is also caused by the thickening or thinning of the stratocumulus layer. However, at 12:00 the change in SWD due to the variations of the number of droplets is clear to see.
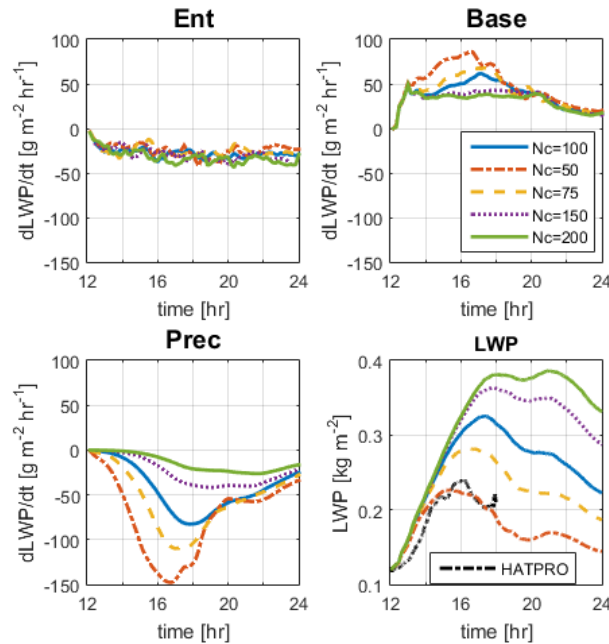

Figure 4.6 - The entrainment, base and precipitation tendencies for variations in N_c on February 18 2011. The legend shows the value for N_c used, which can also be found in Table 4.1. The right panel shows the estimated cloud LWP, together with the measured values. Time is in UTC.
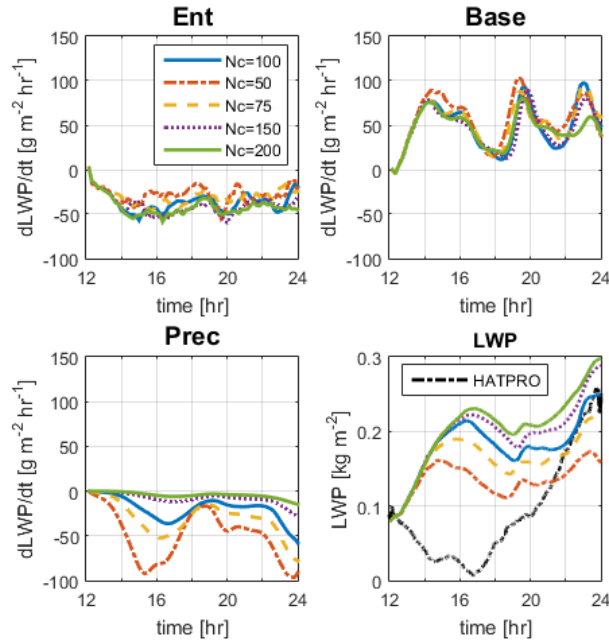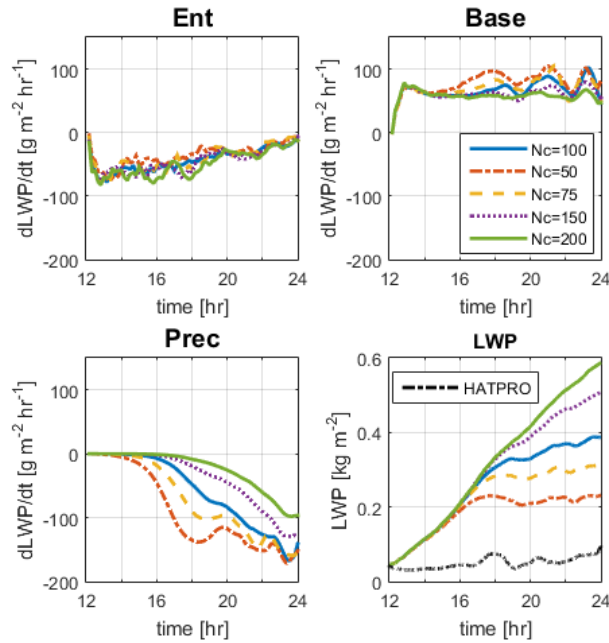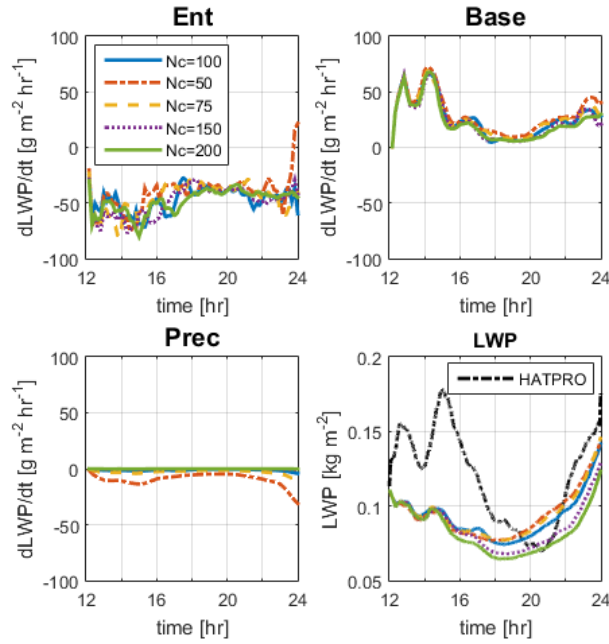
Figure 4.7 – The entrainment, base and precipitation tendencies for variations in N_c on November 6 2011. The legend shows the value for N_c used, which can also be found in Table 4.1. The right panel shows the estimated cloud LWP, together with the measured values. Time is in UTC.

Figure 4.8 – The entrainment, base and precipitation tendencies for variations in N_c on January 29 2012. The legend shows the value for N_c used, which can also be found in Table 4.1. The right panel shows the estimated cloud LWP, together with the measured values. Time is in UTC.

Figure 4.9 – The entrainment, base and precipitation tendencies for variations in N_c on March 13 2012. The legend shows the value for N_c used, which can also be found in Table 4.1. The right panel shows the estimated cloud LWP, together with the measured values. Time is in UTC.
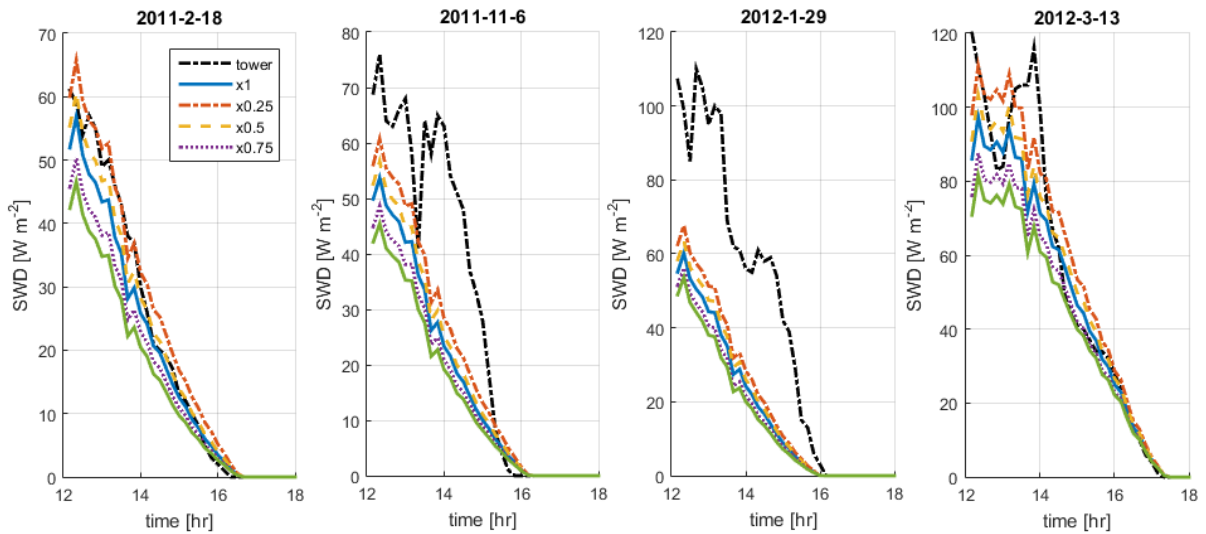
Figure 4.10 – Comparison of the shortwave down welling radiation estimated by DALES for the four winter days. Each plot shows the change in SWD due to the variations in N_c. The values measured at Cabauw are shown in black. Time is in UTC.

Finally, the last modification made is reducing the surface latent heat flux calculated by DALES. The results are shown in Figure 4.11 - Figure 4.14, which show the base and precipitation tendencies together with the LWP. Note again that the other tendencies are not displayed. These reductions greatly affect the base tendencies; the variations of multiplication factor have all reduced the base tendencies on the four days. The magnitude of the decrease in the base flux tendencies is directly linked to the magnitude of the reduction of the surface flux; runs with a factor of 0.25 have the greatest reduction in base fluxes, runs with a factor of 0.5 have the second largest reduction and the runs with a factor of 0.75 have the smallest reduction. This can also be explained by the approximately linear flux profiles. The fluxes at the inversion height are not changed, so a change to the surface flux profiles will affect the base

fluxes. The reduced thickening effect of the base fluxes is reflected in the decrease of the LWP. As a consequence less rainwater is formed and the precipitation flux is reduced.

The reduced latent heat fluxes are also compared against the measurements, shown in Figure 4.15. It is clear that by applying this crude multiplication factor the magnitude of the latent heat flux can be brought in line with the measurements. On February 18, January 29 and March 13 during the two to three hours the DALES estimates – using a factor of 0.25 – were similar to the measurements. November 6 required a factor of 0.5. After the initial hours DALES still overestimates the latent heat flux, the cause of which was already discussed in Chapter 3.

Although it is clear that reduction of the surface latent heat flux has reduced the LWP, it has not changed the incorrect estimation of the increasing LWP on November 6 and January 29.
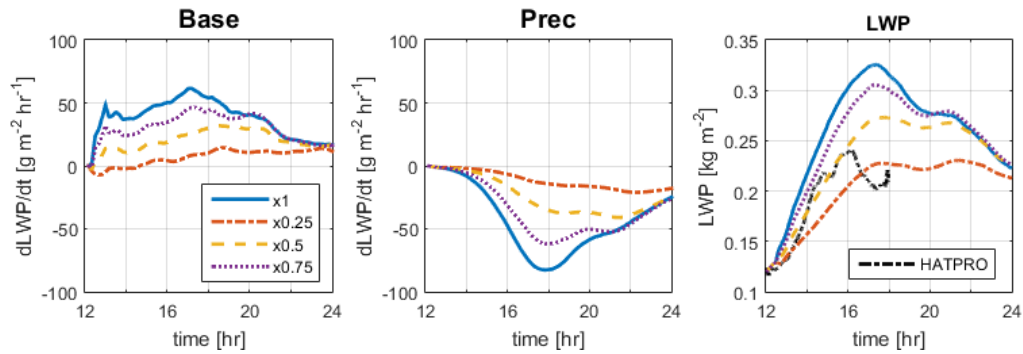
Figure 4.11 - The base and precipitation tendencies for variations in surface latent heat flux on February 18 2011. The legend indicates the scale factor, which can also be found in Table 4.1. The right panel shows the estimated cloud LWP, together with the measured values. Time is in UTC.
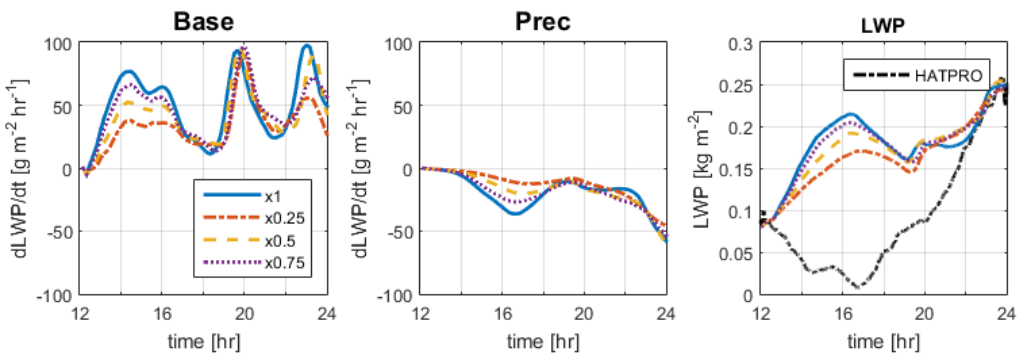

Figure 4.12 - The base and precipitation tendencies for variations in surface latent heat flux on November 6 2011. The legend indicates the scale factor, which can also be found in Table 4.1. The right panel shows the estimated cloud LWP, together with the measured values. Time is in UTC.
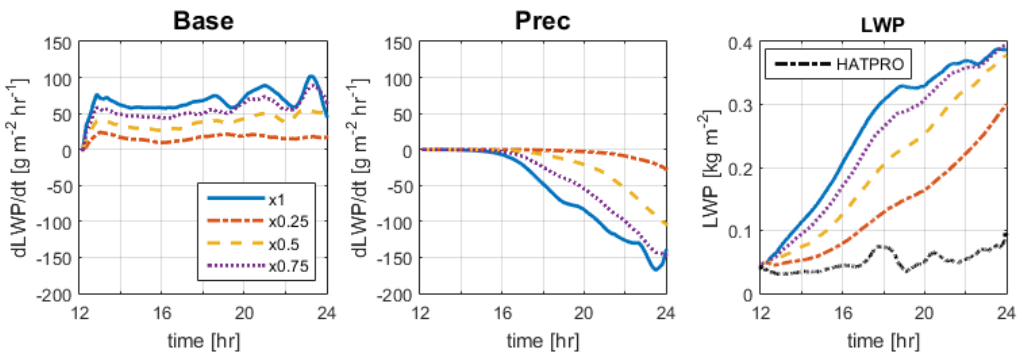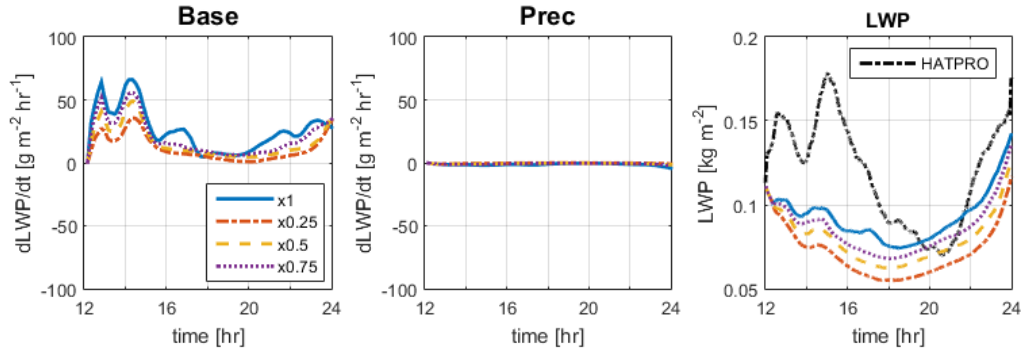

Figure 4.13 - The base and precipitation tendencies for variations in surface latent heat flux on January 29 2012. The legend indicates the scale factor, which can also be found in Table 4.1. The right panel shows the estimated cloud LWP, together with the measured values. Time is in UTC.

42

Figure 4.14 - The base and precipitation tendencies for variations in surface latent heat flux on March 13 2012. The legend indicates the scale factor, which can also be found in Table 4.1. The right panel shows the estimated cloud LWP, together with the measured values. Time is in UTC.
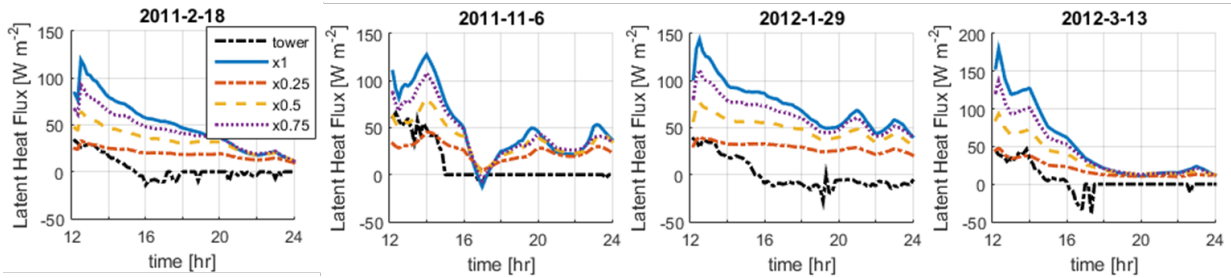
Figure 4.15 - Comparison of the latent heat flux estimated by DALES for the four winter days. Each plot shows the change in the latent heat flux due to the applied multiplication factor. The values measured at Cabauw are shown in black. Time is in UTC.

4.5   Discussion and Conclusions

In this chapter the LWP budget analysis was used to investigate the four winter cases selected in Chapter 3. This analysis separates the important tendencies of the LWP into six individual contributions. This tool proved to be a useful aid in determining which processes were responsible for the evolution of the LWP. It was applied to all four cases, however, February 18 was used to introduce and familiarise the reader with the method. It was also demonstrated that the advection tendency was relatively small compared to the dominant tendencies, which is an important conclusion for using DALES to predict stratocumulus occurrence.

Next the initialisation parameters for each run were altered slightly in order to assess the effect of the uncertainties in the initial conditions. In this study three types of variations were investigated; varying the inversion jumps, varying the precipitation by changing the number of cloud droplets and varying the magnitude of the surface latent heat flux.

Determining the actual inversion jumps will remain difficult, until they can be measured directly. However, the runs where variations were applied to the inversion jumps show that the system is very robust to these variations and that there is room for error; the contributions to the LWP tendency tend to balance each other out and prevent the stratocumulus from disappearing. In general the model results are very robust to variations, including the other two types of variations; only in two cases did the stratocumulus layer dissolve, in both cases this was caused by inversion jumps that satisfied the buoyance reversal criterion. The model demonstrates a great ability to correct itself.

The results from the variation of the number of cloud droplets (N_c) demonstrates the importance of using an accurate value for the number of aerosols in the air. The precipitation tendency was greatly affected by the change in N_c, directly influencing the thickness and the reflectivity of the stratocumulus layer. It is recommended to use actual measurements for the concentration of aerosols in the atmosphere, instead of the standard value used in this study.

The crude multiplication factor applied to the surface latent heat flux caused large changes in the turbulent flux profiles, which was reflected in large change in the base tendencies. It was also

demonstrated that the reduction in surface latent heat flux brought it more in line with the measurements done at Cabauw. This demonstrates that the surface fluxes play an important role in the evolution of stratocumulus layers. Together with fact that the current model does not capture the diurnal cycle well it is clear that using the interactive surface model should benefit future runs greatly.

Unfortunately, no clear cause was found for the incorrect LWP estimates on November 6 and January 29; none of the variations gave a clear-cut answer to the problems observed in Chapter 3. However, it clear that the estimation of the LWP can be (greatly) influenced by applying variations in the surface latent heat flux and the number of cloud droplets.
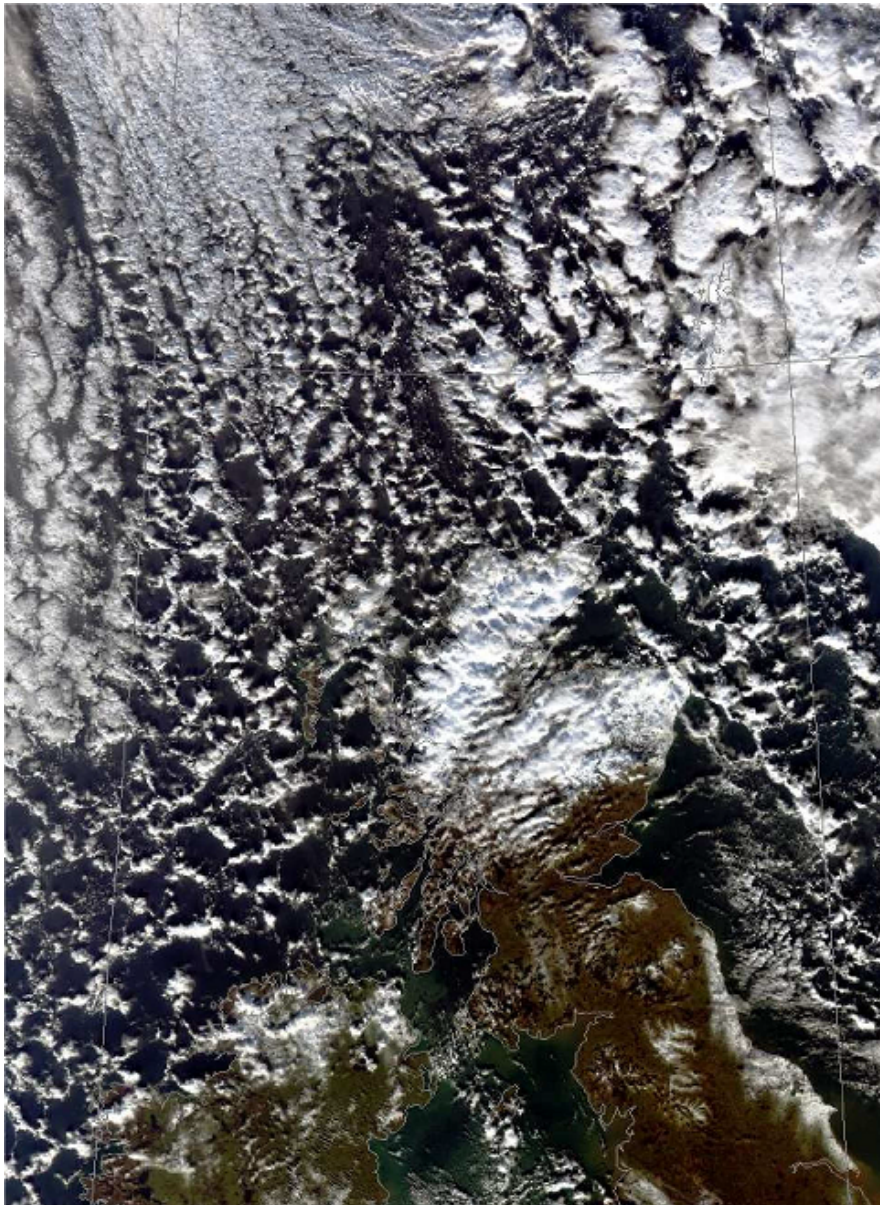
5 Spin up

Figure 5.1 - Satellite image of the Norwegian Sea during the CAO of January 31, 2010 12:53 UTC. (Src: Met office)

5.1 Introduction

A model like DALES has a spin up time. This is the time the model takes to create a turbulent flow that is dominated by the resolved motions, with only a small contribution from the sub grid scales that have to be parametrised, to the full scale turbulent motions (tens of kilometres in the horizontal plane). When the model is initialised the model starts out homogeneously horizontally (i.e. clouds are uniform throughout the domain) with small turbulent motions which will grow over time. For this reason the first few hours of the model runs are usually discarded, but even then the scales of turbulent motion can still be growing in later stages of the simulation.

Since the atmosphere is fully turbulent, ideally the model is initialised like this as well. The next sections will discuss a novel method that might achieve this. First some initial testing results are discussed, and then they will be applied to a case that might benefit greatly from such a warm start; the Cold Air Outbreak on January 31 2010, which has been investigated thoroughly in the master thesis by Frederikse (2013) as well as by others.

A cold air outbreak is a phenomenon that occurs when cold air which originates above ice is transported over a relatively warm sea surface. It is characterised by a strong wind that blows the air over a sea with an increasing surface temperature. This creates a thermal instability that gives rise to shallow convection in the boundary layer. During a cold air outbreak stratocumulus and shallow cumulus clouds are formed. The stratocumuli in such events can sometimes be recognised by their typical appearance as cloud streets. They fan out over the warmer sea and break up to form open cells with cumulus clouds (see Figure 5.1).

5.2 Theory

To analyse the growth of the turbulent motions the time evolution of the length scales present in the simulation is investigated. In particular the dominant length scales are of interest. A convenient method to find these length scales is to perform a spectral analysis. (De Roode et al., 2004).

The first step in such an analysis is to subtract the mean value of a field f from the field itself such that only the variations from the mean of the LWP are left.

$$f' = f(x,y) - \bar{f} \tag{5.1}$$

where the bar indicates the mean value and the accent indicates the variations.

The next step is to perform a 2D Fourier Transform to find the 2D spectral density $S(k_x, k_y)$.

$$\hat{f}(k_x, k_y) = \iint f(x,y) e^{-2\pi i (k_x x + k_y y)} \, dx dy \tag{5.2}$$

$$S(k_x, k_y) = \left| \hat{f}(k_x, k_y) \right|^2 \tag{5.3}$$

By transforming k_x and k_y to cylindrical coordinates one can obtain a spectral density that is only depending on k, where

$$k = \sqrt{k_x^2 + k_y^2} \tag{5.4}$$

$$k_x = k \cos(\theta), \qquad k_y = k \sin(\theta) \tag{5.5}$$

$$\theta = tan^{-1}\left(\frac{k_y}{k_x}\right), \qquad 0 \leq \theta \leq \pi \tag{5.6}$$

By integrating out the dependency on θ one is left with the spectral density that is only depending on k.

$$S(k) = \int_0^\pi S(k\,cos(\theta)\,,k\,sin(\theta))k\;d\theta \tag{5.7}$$

Note that the due to Parseval's Theorem the total variance of the field is given by the integral of S over all wavenumbers.

$$\sum_{All\;space} |f'|^2 = \int S(k)dk \tag{5.8}$$

One could simply take the wave number k with the highest spectral density to determine the dominant length scales. However, this has a disadvantage in that any discrete spectral analysis suffers from noise. Also, it is preferred to find a range of characteristic length scales, not just one.

For these reasons the Ogive is a practical tool. The Ogive is defined as the integral of the spectral density between the wavenumber k and the Nyquist frequency $k_{Ny} = \frac{1}{2\Delta x}$ with Δx the size of a grid box.

$$O(k) = \int_k^{k_{Ny}} S(k)\,dk \tag{5.9}$$

Thus the Ogive gives the contribution to the variance from all wavenumber components above wavenumber k.

To find a length scale the critical wavenumber k_c is first computed from

$$O(k_c) = \gamma \int_{k_c}^{k_{Ny}} S(k)\,dk \tag{5.10}$$

For γ a value of 2/3 is picked, indicating that 2/3 of the variance lies above the critical wavenumber. This value is taken in accordance with the article from De Roode et al. (2004)

Now a critical length scale can be computed:

$$L_{critical} = \frac{1}{k_c} \tag{5.11}$$

The critical length scale can be interpreted as the length scale for which 2/3 of the turbulent energy acts on smaller scales and 1/3 of the energy at larger scales.

5.3 Methodology

DALES has two built-in functions that could make it possible to initialise the model fully turbulent. One is the option to nudge the atmospheric profiles to a desired end state. This can also be the initial state. The slab-averaged prognostic variables φ are nudged at each time step to a prescribed value φ^{rel} with a relaxing time scale t^{rel} (src: DALES article):

$$\left(\frac{\partial\varphi}{\partial t}\right)^{rel} = -\frac{1}{t^{rel}}(\overline{\varphi} - \varphi^{rel}) \tag{5.12}$$

The reason φ^{rel} is subtracted from the mean $\overline{\varphi}$, instead from the individual values of φ, is to ensure that room for variability within the LES domain remains, and the small-scale turbulence will not be disturbed by the nudging.

DALES offers the possibility to use a time varying $\varphi^{rel}(t)$. However, since the desired end state is the initial state, the expressions simplify such that φ^{rel} is equal to the desired end state and t^{rel} is equal

to the prescribed nudge time. The expression is now easy to interpret; if $\overline{\varphi}$ equals φ^{rel}, the expression is zero and no nudging takes place. If not, the mean value is pushed into the direction of the desired end state of which the strength depends on the value of t^{rel}.

The state of the simulation is saved at a time interval specified by the user. These saved files can be used to restart the model. The model does not require any other input files to continue the simulation. This is is called a warm start. These two options are used to explore a start that has a turbulent developed field. First a model run is performed of which the profiles are being relaxed to their original state. This is referred to as the nudge run. The last hour of the nudge run is used to re initialise DALES using the warm start option. This model run will be referred to as the warm start. One modification needed to be made to the code, namely the option to reset the elapsed time when using the warm start option. The model keeps track of the time that has elapsed since the start, which is stored in the saved files. This created issues when for example a nudge of eight hours was used: the model assumed eight hours had elapsed already.

An analysis is made of choosing different relaxing times and the effect this has on a warm start compared to a normally initialised model run, referred to as the cold start.

This method is then applied to the Cold Air Outbreak. To analyse the output the length scales of liquid water path of cold start runs and warm start runs are compared to each other.

5.4 Results

5.4.1 Effect of varying the relaxation time

To investigate the effects of varying the relaxing time, three spin up runs are performed with a $t^{rel} = \infty$, 1 hour , 10 minutes and 1 minute. The model is initialised with the same profiles as the stratocumulus case on February 18 2011, which was discussed in previous chapters. The reason for doing so is the possible application of the warm start scheme to these stratocumulus cases. The domain size is 12 x 12 x 2.0 km^3 and the grid box is 120 x 120 x 200. The reason a larger domain size is picked compared to the 6.4 x 6.4 x 2.0 km^3 of the runs performed in Chapter 3 is to ensure there is enough room for large scale motions to develop. To able to perform a spectral analysis the option to dump 3D fields at particular time steps has to be turned on before running DALES. Because of the size of these files, the fields are dumped per hour starting at hour 1. The nudge runs use a constant sea surface temperature and subsidence.

The results are shown in Figure 5.2 – 5.4. It is noticeable that the desired property, namely a thermodynamic state that says quite close to the initial conditions, depends on the relaxation time as the nudge run without relaxing deviates the most. In the boundary layer the temperature and total specific humidity shift by about 0.7 K and 0.5 g/kg respectively. The biggest differences can be seen in the inversion layer, which is not surprising since the growth of the boundary layer is something that naturally occurs during the day. For $t^{rel} = 1\ min$ there is almost no difference at all, except for the corners, which are smoothened.

Figure 5.4 shows that the growth of large scale motions for the spin up runs with $t^{rel} = 1\ hr$ and $t^{rel} = 10\ min$ are practically the same. The growth of the length scales is however inhibited in the spin up run with $t^{rel} = 1\ min$. Therefore if the user desires a very small relaxation time, a trade-off might have to be made between the deviation from the initial profile and the amount of scale growth in the system.
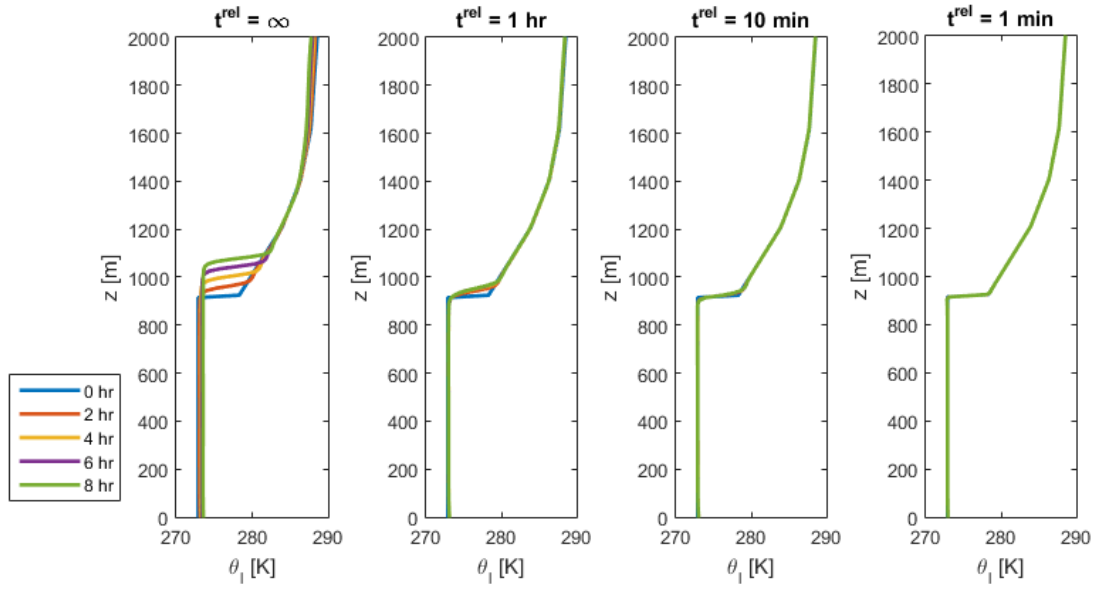
Figure 5.2 – Liquid potentential temperature at t=0,2,4,6 and 8 hours for different values of the relaxing time.
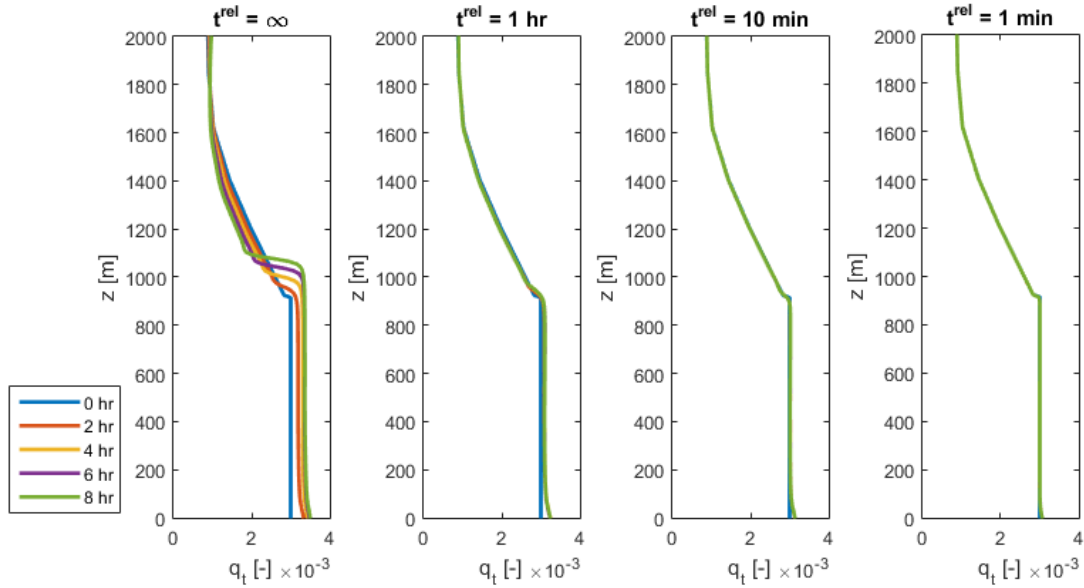

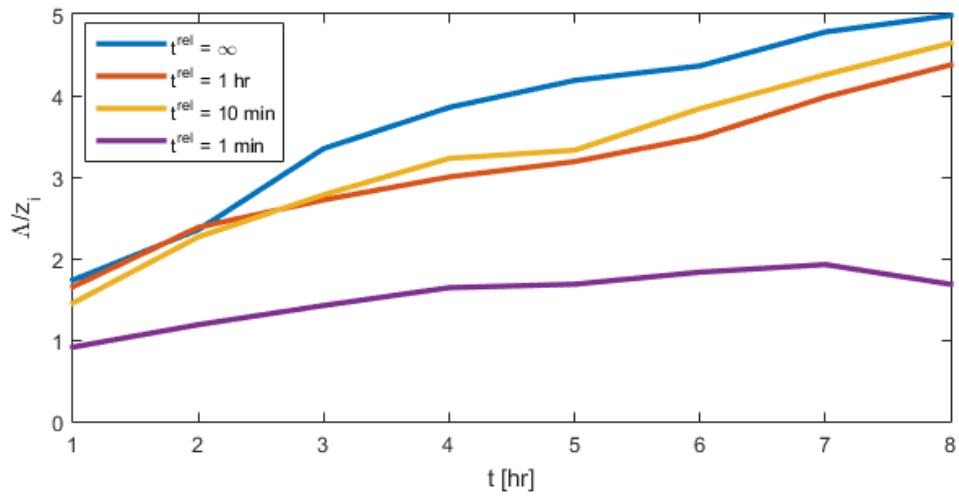**Figure 5.3** – Total specific humidity at t=0,2,4,6 and 8 hours for different values of the relaxing time.

Figure 5.4 – Evolution of length scales for different values of the relaxing time.

Because the spin up run with $t^{rel} = 1\ hr$ shows more deviation from the initial profiles than the spin up run with $t^{rel} = 10\ min$ at t=8 hr the effect of this small difference is investigated by using both spin up runs to initialise a warm start run.

Figure 5.5 and Figure 5.6 show the slab-averaged cloud base and slab-averaged LWP in time. At the start of both warm start runs the cloud base is lower and the LWP is higher than those of the reference run that was performed with the default cold start. The cloud base is 60 meters lower for the warm start run initialised with the $t^{rel} = 1\ hr$ spin up run and 20 m for the warm run initialised with the $t^{rel} = 1\ hr$ spin up run. Inspecting the change of the atmospheric profiles in Figure 5.2 and Figure 5.3 reveals this is not unexpected. The q_t profile has shifted slightly to the right introducing more humidity in the system; mostly so for the $t^{rel} = 1\ hr$ spin up run which is the reason the cloud base is lowest in the run with a warm start initialised with these profiles. This change is not compensated by a large enough positive shift in temperature. Because the cloud base is lower, the LWP has increased as well.

The general evolution of the cloud base and LWP in time of the cold run and the two warm runs show similar behaviour. Some differences can be noted; after four hours the cloud base height of both warm runs becomes higher than that of the cold run. This brings down the LWP of the warm runs to the same level of that of the cold run. The cause of this behaviour is not investigated further in this work, but using the budget analysis of chapter 4 with the original domain size would be a possible option to try to understand this behaviour.

It is expected that by using the spin up run to initialise DALES, more variation in the cloud base and LWP are present from the start, due to the turbulent motions that have carried over from the spin up run. As mentioned the model starts homogeneously in the horizontal plane meaning there is very little variation. The standard deviation of the LWP of the cold run and the two warm runs are plotted in Figure 5.7. The standard deviation of the cold run is in the order of $10^{-4}\ kg\ m^{-2}$, while the warm starts have a much larger standard deviation already; 0.029 $kg\ m^{-2}$ and 0.014 $kg\ m^{-2}$ for the warm starts initialised with the $t^{rel} = 1\ hr$ and $t^{rel} = 10\ min$ spin up runs respectively. Interestingly the standard deviation at $t = 0$ is twice as big for the warm start run ($t^{rel} = 1\ hr$) compared to the warm start run ($t^{rel} = 10\ min$), indicating the horizontal variation at the initialisation of warm start run is affected by the different relaxation times.
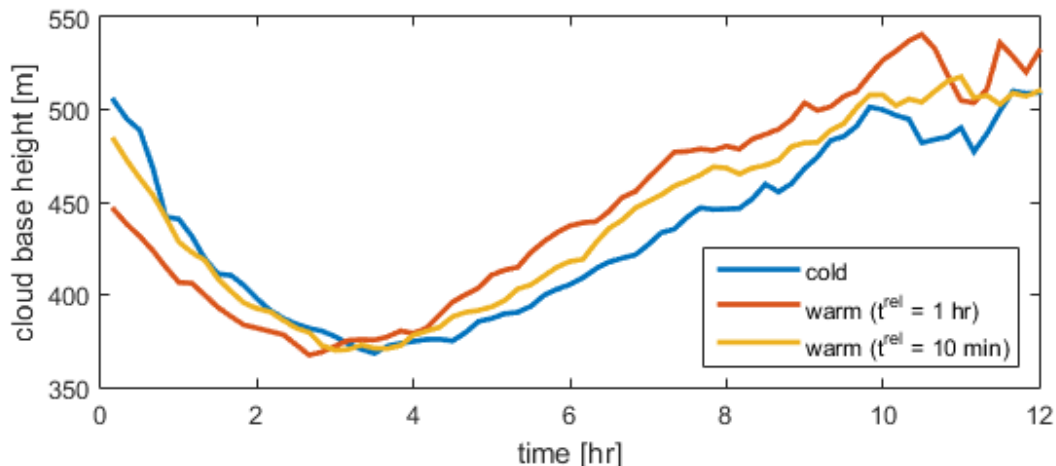

Figure 5.5 – **Cloud base evolution for a cold start (blue) and two warm starts. The warm starts are initialised with the fields from $t^{rel} = 1\ hr$ and $t^{rel} = 10\ min$ spin up runs. Time is in UTC.**
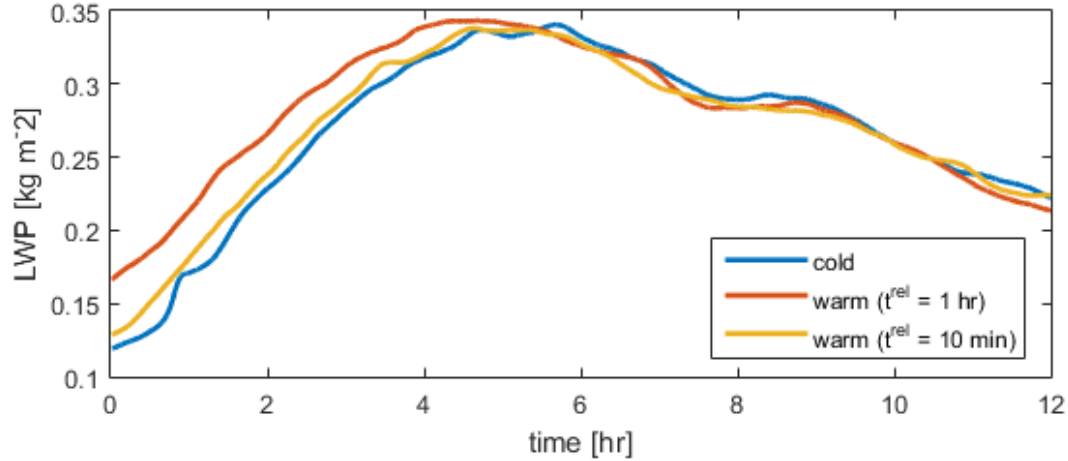
Figure 5.6 – LWP evolution for a cold start and two warm starts. The warm starts are initialised with the fields from $t^{rel} = 1\ hr$ and $t^{rel} = 10\ min$ spin up runs. Time is in UTC.
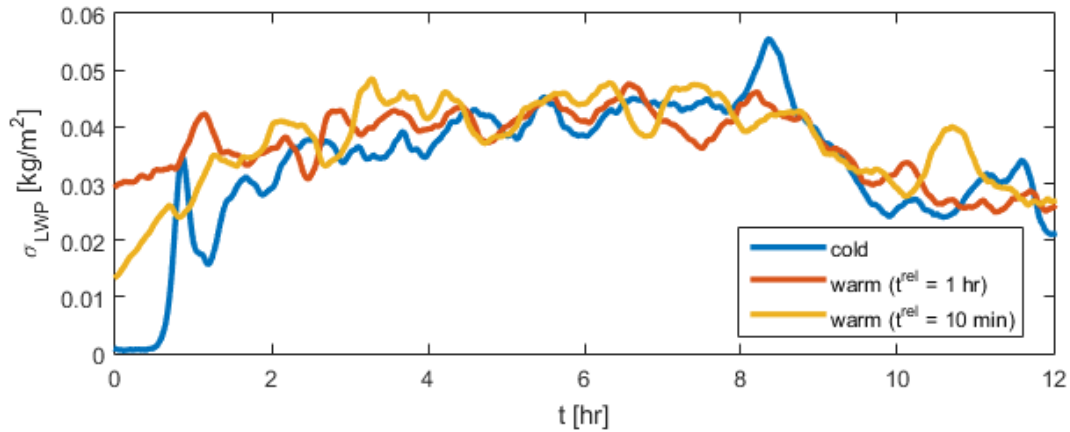

Figure 5.7 – Standard deviation of the LWP for a cold run and two warm runs. The warm starts are initialised with the fields from $t^{rel} = 1\ hr$ and $t^{rel} = 10\ min$ spin up runs. Time is in UTC.

5.4.2   Cold Air Outbreak

The developed method for the warm start initialisation is applied to the Cold Air Outbreak of January 31 2010. The model is initialised to the north west of Scotland over the Atlantic Ocean at 65 degrees latitude and -10 degrees longitude at midnight on January 31 2010. The domain size is 105.6 x 105.6 x 5 km³, using 528 x 528 x 167 points. The duration of the simulation is 14 hours. The profiles are taken from the work of Frederikse (2013).

The results for the reference (cold start) and war start run are shown in Figure 5.8 and Figure 5.9. Figure 5.8 shows the time evolution of the critical length scale as described in the previous section. Figure 5.9 shows the value of calculated liquid water path at each grid point for each hour of the simulation. It is convenient to plot the LWP because it represents the integral over the liquid water content with height over each column and represents the structure of the cloud layer. As expected the length scales grow over time, which is also clear to see from the plots of the LWP. In a cold start the fields start with little structures, but these fields grow over time to very large structures. It is not until hour 11 that the length scales stop growing.

To be able to perform a simulation with fields in which turbulence had fully developed, a spin up run is done. The same settings are used, except that the model is initialised 12 hours earlier and that the time dependent large scale forcings are turned off. The relaxing time is set to 1 hour. Based on the results from the previous section this choice ensures that after the spin up run the warm start is initialised with

large length scales and most variation in the cloud layer. The results are shown in Figure 5.8 and Figure 5.10.

Figure 5.10, $t = 2 \ hr$ shows nice mesoscale structures at the start as intended. Figure 5.8 shows that the critical length scales are also higher than those of the cold start. The dip in the length scale in the first few hours cannot be explained and requires further research. The growth of the length scales in the warm run seem to slow down compared to that of the cold run which can be explained by two things. First, the model might be saturated and cannot grow any further. Second, Frederiks (2013) shows that amplitude of the variance spectrum of the vertical velocity ($\hat{w}$) decreases for increasing length scales. This influences the growth of large scales in q_t, because the change in q_t is related to w (see eq. (5.13)) and thus the growth of lengths scales in the LWP. This could explain why the two curves show inhibited growth when large length scales are developing.

$$\frac{\partial \hat{q}_t{}'}{\partial t} = -\hat{w}' \frac{\partial \bar{q}_t}{\partial z} \tag{5.13}$$

Finally the standard deviation of the LWP and cloud base of both the cold and warm run is compared (see Figure 5.11). The reason why the plot of the cloud base starts at 1 hour is because DALES does not output the variation in the cloud base. Instead, it was calculated directly calculated from the same 3D fields used for the spectral analysis. The figure also shows the intended result; more variations in the warm run initialised with the spin up run than the cold run. Unlike the length scales, the standard deviations for the LWP and cloud base become similar for the cold and warm run after 6 hours and stay similar for the remainder of the simulations.
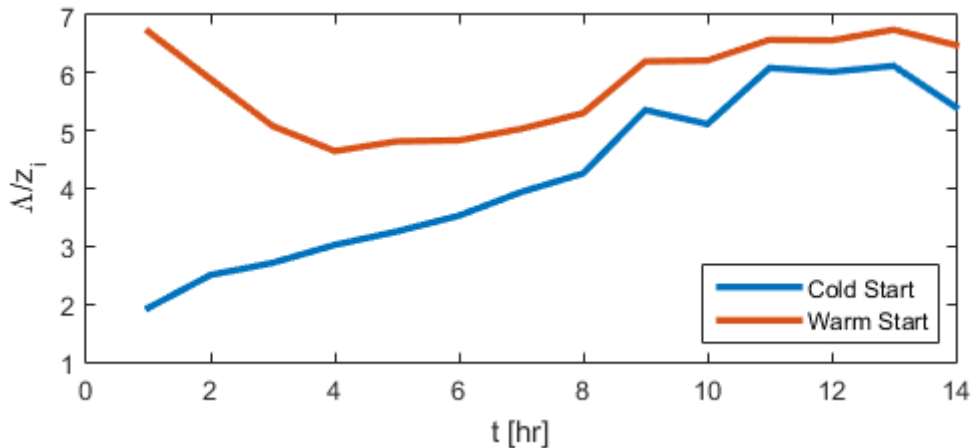

Figure 5.8 – Evolution of length scales for the cold start (blue) and warm start (red) in the case of the Cold Air Outbreak of January 31. Time is in UTC.
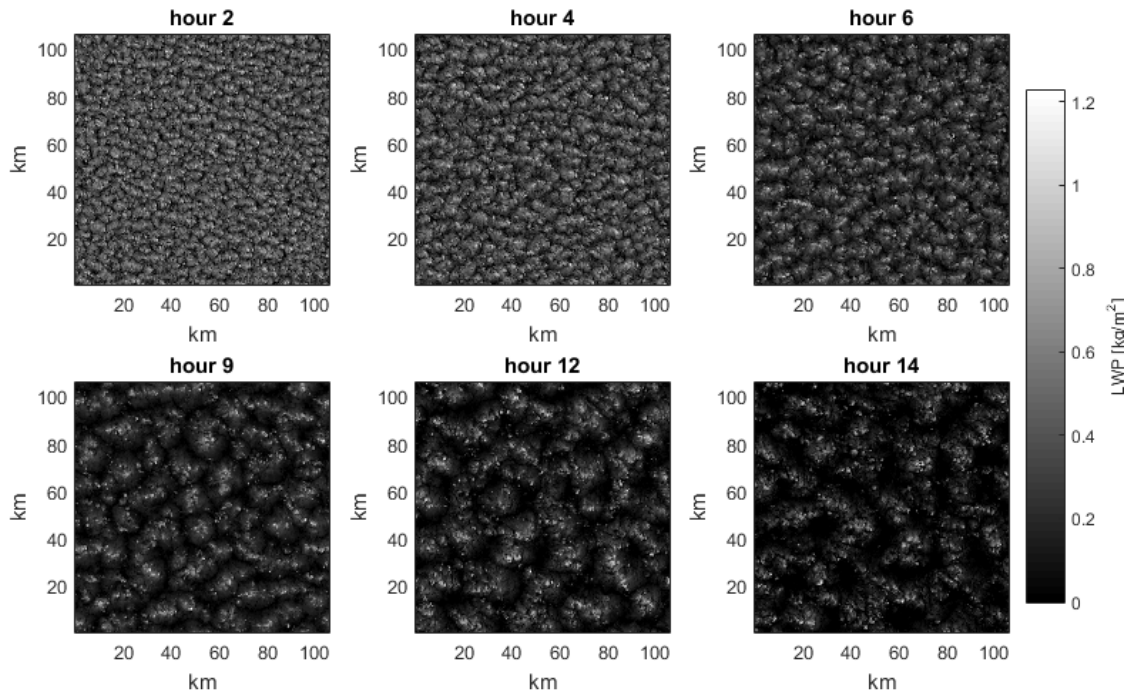
Figure 5.9 – Evolution of the LWP field for the reference run (cold start) for the Cold Air Outbreak of January 31.
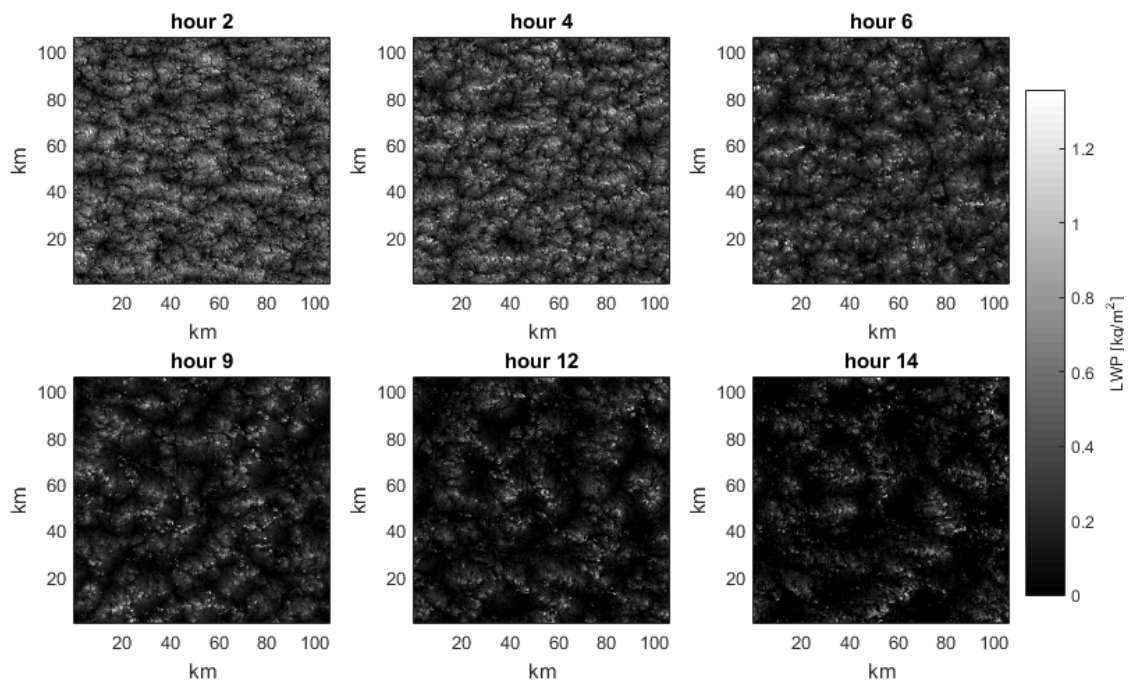

Figure 5.10 - Evolution of the LWP field using a warm start for the Cold Air Outbreak of January 31 initialised with the fields from a $t^{rel} = 1\ hr$ spin up run.
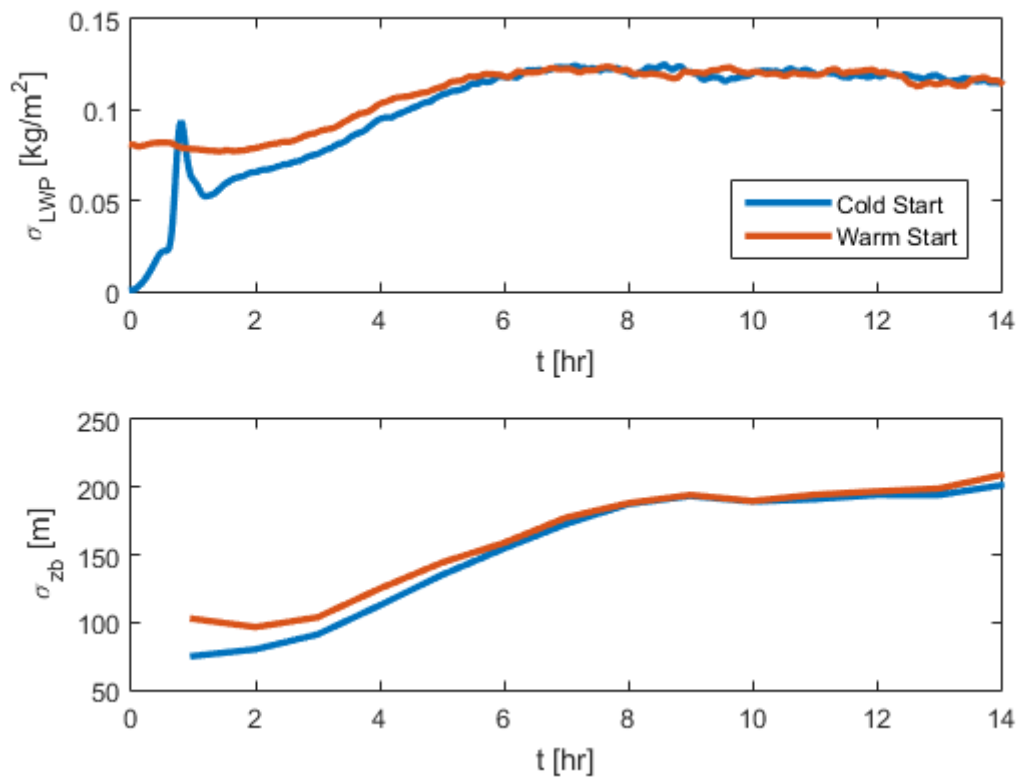
Figure 5.11 – Comparison of the standard deviation of the cold and warm run. Top shows the standard deviation of the LWP and bottom shows the variation of cloud base. Time is in UTC.

5.5 Discussion and Conclusions

In this chapter a novel method to initialise the model with fully turbulent motions was explored. The initial results are encouraging. The large scale structures formed in the spin up runs carry over to a warm start simulation, while the initial profiles stay relatively the same. In future research this approach could for example be used to investigate mesoscale fluctuations that reduces the thickness of the stratocumulus layer to less than 100 metre, decreasing the long wave radiative cooling and leading to the breakup of the layer.

The amount of deviation from the intended profiles depends on the relaxing time; the smaller the relaxing time the less deviation from the original profiles. However, if the relaxing time is picked too short the length scale growth is inhibited, which is not the intention of using a spin up run.

The warm start runs also start out with less homogeneity in the horizontal plane; there is more variation in the LWP and cloud base compared to that of a cold run. This amount of variation does seem to depend on the relaxing time, because there was less variation with shorter relaxing times.

Warm start runs show slightly different behaviour at than cold start runs. The shifts in the profiles that happen during the spin up run cause the warm runs to be initialised with different amounts of humidity and/or temperature than the original cold run. Choosing short relaxing times counters these shifts, but has a negative effect on the growth of the length scales and amount of variation.

To conclude, the spin up approach is a valid consideration when looking for a method to initialise DALES with more turbulence. As long as the relaxing time can be chosen such that the required length scales and variation have time to develop and that the profiles remain close to the prescribed profile then this work indicates that the spin up approach gives good results.

6 General Conclusions and Recommendations

The six research questions posed in the introduction can now be answered based on the results discussed in Chapters 3, 4 and 5.

- *Can the LES model be initialised by assimilating observations in addition to large scale weather model results?*

    In this work a method was developed that creates profiles for DALES based on observations obtained at the Cabauw Experimental Site for Atmospheric Research and on results from the large scale weather model RACMO. This method does not rely on radiosonde measurements. Instead the temperature and humidity profiles are based on the Cabauw tower measurements. The inversion height is estimated using the liquid water path and cloud base height measurements. Because currently radiosonde measurements are only obtained once per day, this method has as added benefit that initialisation profiles can be created starting at any time of day.

    For the four selected winter cases the developed method succeeded in creating profiles that matched well with measurements made by the radiosonde. These four cases all satisfied the four selection criteria for identifying stratocumulus occurrence. The method was not suitable for the five summer cases that were selected based on cloud cover and cloud base height, because on none of these days a well-mixed stratocumulus-topped boundary layer occurred.

- *How do the LES results compare to the observational data?*

    On February 18 2011 and March 13 2012 the DALES results compared well with the measurements. On November 6 2011 and January 29 2012 DALES could not correctly estimate the LWP. In both reference cases on these two days the results indicated an increase in the LWP, while no such increase in the LWP was observed. This is also reflected in the estimations of the incoming solar radiation, which is underestimated by DALES. A possible cause for this incorrect estimate of the LWP was attributed to the overestimation of the latent heat flux by the assumption of a saturated ground. In this study the interactive surface model in DALES was not utilised, since sufficient time was not available in the project to carefully set up the runs with the soil scheme as this requires a detailed specification of the soil properties. Instead, the surface fluxes were calculated based on the surface temperature. The latent heat flux estimated by DALES did not compare well with the measurements however; the magnitude of the latent heat flux was too high and the diurnal cycle was not captured well. Using the interactive surface model should benefit future runs greatly.

- *Does the LES model produce better predictions than the large scale weather model?*

    In three out of four cases DALES gives better predictions than RACMO. The case performed on November 6 is the only case where RACMO does better at predicting the time evolutions of the cloud base and the LWP. This might be an indication that the stratocumulus occurrence found that day is part of a large weather front, which is captured well by a model like RACMO. Interestingly, DALES predicts the incoming solar radiation better in all four cases. RACMO does a notably bad job. This is a clear sign that a model like DALES would benefit the solar industry greatly and it is therefore recommended that more research is dedicated to the use of the model for such purposes.

- *How sensitive are the model results to uncertainties in the observed initial vertical profiles?*

  To diagnose and estimate the effect of uncertainties in the initialisation parameters on the simulated LWP tendencies, variations were applied to the initialisation of DALES. The variations were changes to the inversion jumps of humidity and temperature, changes in the number of cloud condensation nuclei and changes to the by DALES calculated surface latent heat flux. The results of these variations showed that the time evolution of the LWP can be (greatly) influenced.

  The results of Chapter 4 demonstrate that the simulated stratocumulus layer is very robust to the applied variations. Out of all the model runs (48 in total, 12 for each day) two runs were found where the stratocumulus layer rapidly dissolved. In both these cases the variations to inversion jumps for the humidity and temperature satisfied the buoyance reversal criterion. The model demonstrated a great ability to compensate for the effects of a change in the inversion jumps with changes in the base flux and precipitation. The variations of the surface latent heat flux and number of cloud droplets had a great effect on the LWP, but none of these variations caused the stratocumulus layer to dissolve. Specifically, the reduction of the surface latent heat flux caused a decrease in the LWP and an increase or decrease in the number of cloud droplets caused an increase or decrease in the LWP, respectively.

- *Which conditions like the inversion jumps and the cloud droplet concentration have the biggest influence on the evolution of the model?*

  The budget analysis used in Chapter 4 revealed that the amount of cloud condensation nuclei or aerosols present in the atmosphere greatly affected the liquid water path tendency and the cloud thickness; clean air with a lower number of cloud droplets resulted in thinner clouds while air containing lots of particles resulted in thicker clouds. DALES is initialised with a standard value for the number of particles, and it is therefore recommended that in future research representative values for number of cloud droplets are used, on the basis of measured aerosol concentrations, if present.

  The surface fluxes also play an important role in the LWP tendency. In this study DALES computes these from the prescribed surface temperature assuming the surface is saturated. This is not a good assumption for simulations performed over land. It is recommended that a working surface model is used in future research.

- *How does a simulation initialised with fully turbulent motions perform compared to a simulation that is not initialised with fully turbulent motions?*

  In Chapter 5 it was shown that simulations can be initialised with fully turbulent motions. This was realised by performing spin up runs which allow turbulent motions to develop while the atmospheric profiles are kept at their initial state. This is achieved by using the option in DALES to relax atmospheric profiles to a desired state. The amount of deviation from the initial profiles depends on the value of the relaxing time scale; smaller values cause less deviations. However, the results seem to indicate that smaller values of the relaxing time scale cause less turbulent motions to develop.

  This approach is applied to the Cold Air Outbreak case of January 31 2010. The spin up run is used to initialise the warm start run. The large scale structures formed in the spin up run

carry over nicely to the warm start simulation; the critical length scale is much higher, there is a lot more variance in the cloud base height and in the liquid water path compared to the reference (cold start) run.

In future research this approach could for example be used to investigate mesoscale fluctuations that reduces the thickness of the stratocumulus layer to less than 100 m, decreasing the long wave radiative cooling and leading to the breakup of the layer.

7 Bibliography

Ackerman, A. S., M. P. Kirkpatrick, D. E. Stevens, and O. B. Toon. 2004. "The impact of humidity above stratiform clouds on indirect aerosol climate forcing." *Nature* 432 (7020): 1014-7.

Ackerman, Andrew S., Margreet C. vanZanten, Bjorn Stevens, Verica Savic-Jovcic, Christopher S. Bretherton, Andreas Chlond, Jean-Christophe Golaz, Hongli Jiang, Marat Khairoutdinov, Steven K. Krueger, David C. Lewellen, Adrian Lock, Chin-Hoh Moeng, Kozo Nakamura, Markus D. Petters, Jefferson R. Snider, Sonja Weinbrecht, and Mike Zulauf. 2009. "Large-Eddy Simulations of a Drizzling, Stratocumulus-Topped Marine Boundary Layer." *Monthly Weather Review* 137 (3): 1083-1110.

Albrecht, Bruce A. 1989. "Aerosols, Cloud Microphysics, and Fractional Cloudiness." *Science* 245 (4923): 1227-1230.

Bretherton, C. S., M. K. Macvean, P. Bechtold, A. Chlond, W. R. Cotton, J. Cuxart, H. Cuijpers, M. Mhairoutdinov, B. Kosovic, D. Lewellen, C. H. Moeng, P. Siebesma, B. Stevens, D. E. Stevens, I. Sykes, and M. C. Wyant. 1999. "An intercomparison of radiatively driven entrainment and turbulence in a smoke cloud, as simulated by different numerical models." *Quarterly Journal of the Royal Meteorological Society* 125 (554): 391-423.

Caldwell, Peter, and Christopher S. Bretherton. 2009. "Large Eddy Simulation of the Diurnal Cycle in Southeast Pacific Stratocumulus." *Journal of the Atmospheric Sciences* 66 (2): 432-449.

Carman, J. K., D. L. Rossiter, D. Khelif, H. H. Jonsson, I. C. Faloona, and P. Y. Chuang. 2012. "Observational constraints on entrainment and the entrainment interface layer in stratocumulus." *Atmospheric Chemistry and Physics* 12 (22): 11135-11152.

De Roode, S. R. 2004. Clouds.

De Roode, Stephan R., and Peter G. Duynkerke. 1997. "Observed Lagrangian Transition of Stratocumulus into Cumulus during ASTEX: Mean State and Turbulence Structure." *Journal of the Atmospheric Sciences* 54 (17): 2157.

De Roode, Stephan R., Peter G. Duynkerke, and Harm J. J. Jonker. 2004. "Large-Eddy Simulation: How Large is Large Enough?" *Journal of the Atmospheric Sciences* 61 (4): 403-421.

De Roode, Stephan R., A. Pier Siebesma, Sara Dal Gesso, Harm J. J. Jonker, Jerôme Schalkwijk, and Jasper Sival. 2014. "A mixed-layer model study of the stratocumulus response to changes in large-scale conditions." *Journal of Advances in Modeling Earth Systems* 6 (4): 1256-1270.

Deardorff, J. W. 1980. "Cloud Top Entrainment Instability." *Journal of the Atmospheric Sciences* 37 (1):131-147.

Faloona, Ian, Donald H. Lenschow, Teresa Campos, B. Stevens, M. van Zanten, B. Blomquist, D. Thornton, Alan Bandy, and Hermann Gerber. 2005. "Observations of Entrainment in Eastern Pacific Marine Stratocumulus Using Three Conserved Scalars." *Journal of the Atmospheric Sciences* 62 (9): 3268-3285.

Frederikse, T. 2013. "Simulations and explanations of large-scale structures during a Cold Air Outbreak."

Applied Sciences, TU Delft.

Haij, M. J. de, W. M. F. Wauben, and Henk Klein Baltink. 2007. *Continuous mixing layer height determination using the LD-40 ceilometer: a feasibility study, WR 2007-01;* De Bil: Royal Netherlands Meteorological Institute (KNMI).

Heus, T., A. Pier Siebesma, O. Geoffroy, C. C. Van Heerwaarden, K. Van Den Dries, A. F. Moene, J. V. G. De Arellano, H. J. J. Jonker, S. R. De Roode, S. Axelsen, and D. Pino. 2010. "Formulation of the Dutch Atmospheric Large-Eddy Simulation (DALES) and overview of its applications." *Geoscientific Model Development* 3 (2): 415-444.

Heus, T., C. Van Heerwarden, J. J. Van der Dussen, and J. Ouwersloot. 2010. Overview of all namoptions in DALES.

Klein, S. A., and D. L. Hartmann. 1993. "The Seasonal Cycle of Low Stratiform Clouds." *Journal of Climate* 6 (8): 1587.

Lilly, D. K. 1968. "Models of cloud-topped mixed layers under a strong inversion." *Quarterly Journal of the Royal Meteorological Society* 94 (401): 292-309.

Marshall, John, and R. Plumb. 2007. "Atmosphere, Ocean and Climate Dynamics an Introductory Text." Elsevier.

Moeng, Chin-Hoh. 2000. "Entrainment Rate, Cloud Fraction, and Liquid Water Path of PBL Stratocumulus Clouds." *Journal of the Atmospheric Sciences* 57 (21):3627-3643.

Neggers, R.A.J., and Siebesma A.P. 2010. The KNMI Parameterization Testbed Users Guide Version 2.0. KNMI.

Nicholls, S. 1989. "The structure of radiatively driven convection in stratocumulus." *Quarterly Journal of the Royal Meteorological Society* 115 (487):487-511.

Nicholls, S., and J. D. Turton. 1986. "An observational study of the structure of stratiform cloud sheets: Part II. Entrainment." *Quarterly Journal of the Royal Meteorological Society* 112 (472): 461-480.

Park, Sungsu, Conway B. Leovy, and Margaret A. Rozendaal. 2004. "A New Heuristic Lagrangian Marine Boundary Layer Cloud Model." *Journal of the Atmospheric Sciences* 61 (24): 3002-3024.

Randall, David A. 1980. "Conditional Instability of the First Kind Upside-Down." *Journal of the Atmospheric Sciences* 37 (1):125-130.

Randall, David A. 1984. "Stratocumulus cloud deepening through entrainment." *Tellus A* 36A (5):446-457.

Schuurbiers, M. 2014. "Forecasting stratocumulus under a strong thermal inversion and in regions of subsidence, with a large-eddy simulation model." Department of Geoscience and Remote Sensing, TU Delft.

Stevens, Bjorn. 2002. "Entrainment in stratocumulus-topped mixed layers." *Quarterly Journal of the Royal Meteorological Society* 128 (586):2663-2690.

Stevens, Bjorn, William R. Cotton, Graham Feingold, and Chin-Hoh Moeng. 1998. "Large-Eddy

Simulations of Strongly Precipitating, Shallow, Stratocumulus-Topped Boundary Layers." *Journal of the Atmospheric Sciences* 55 (24):3616.

Stevens, B., C. H. Moeng, and P. P. Sullivan. 1999. "Large-Eddy Simulations of Radiatively Driven Convection: Sensitivities to the Representation of Small Scales." *Journal of the Atmospheric Sciences* 56 (23):3963-3984.

Stevens, Bjorn, Chin-Hoh Moeng, Andrew S. Ackerman, Christopher S. Bretherton, Andreas Chlond, Stephan de Roode, James Edwards, Jean-Christophe Golaz, Hongli Jiang, Marat Khairoutdinov, Michael P. Kirkpatrick, David C. Lewellen, Adrian Lock, Frank Müller, David E. Stevens, Eoin Whelan, and Ping Zhu. 2005. "Evaluation of Large-Eddy Simulations via Observations of Nocturnal Marine Stratocumulus." *Monthly Weather Review* 133 (6): 1443-1462.

Stull, Roland B., 1988. *An Introduction to Boundary Layer Meteorology.* Kluwer Academic Publishers

Turton, J. D., and S. Nicholls. 1987. "A Study of the Diurnal Variation of Stratocumulus Using A Multiple Mixed Layer Model." *Quarterly Journal of the Royal Meteorological Society* 113 (477): 969-1009.

Uchida, J., C. S. Bretherton, and P. N. Blossey. 2010. "The sensitivity of stratocumulus-capped mixed layers to cloud droplet concentration: Do les and mixed-layer models agree?" *Atmospheric Chemistry and Physics* 10 (9): 4097-4109.

Van Der Dussen, J. J., S. R. De Roode, and A. P. Siebesma. 2014. "Factors controlling rapid stratocumulus cloud thinning." *Journal of the Atmospheric Sciences* 71 (2): 655-664.

Van Der Dussen, J. J., S. R. De Roode, and A. P. Siebesma. 2015. "How large-scale subsidence affects stratocumulus transitions." *Atmospheric Chemistry and Physics Discussions* 15 (12): 17229-17250.

Van der Dussen, J. J., A. P. Siebesma, and S. R. De Roode. 2015. "Stratocumulus transitions in present-day and future climate."

Wallace, John M., and Peter Victor Hobbs. 2006. *Atmospheric science: an introductory survey.* New York: Academic Press.

Wood, Robert. 2012. "Stratocumulus Clouds." *Monthly Weather Review* 140 (8): 2373-2423.

Wood, R. 2012. "Stratocumulus clouds." *Monthly Weather Review* (140): 51.

Wood, Robert, and Christopher S. Bretherton. 2004. "Boundary Layer Depth, Entrainment, and Decoupling in the Cloud-Capped Subtropical and Tropical Marine Boundary Layer." *Journal of Climate* 17 (18):3576-3588.

Wyant, Matthew C., Christopher S. Bretherton, Hugh A. Rand, and David E. Stevens. 1997. "Numerical Simulations and a Conceptual Model of the Stratocumulus to Trade Cumulus Transition." *Journal of the Atmospheric Sciences* 54 (1): 168.

A. Namoptions file

&RUN

iexpnr   = 000

lwarmstart = .false.

ltswitch = .false.

startfile = 'initd00h00m000.000'

runtime = 43200

trestart = 3600

dtmax   = 10

ladaptive = .true.

irandom = 43

randthl = 0.1

randqt   = 2.5e-5

nsv   = 2

/

&DOMAIN

imax   = 120

jtot   = 120

kilometreax   = 200

xsize   = 6400.

ysize   = 6400.

xlat   = 52.

xlon   = 5.

xday   = 49.

xtime   = 12.

/

&PHYSICS

z0   = 0.03

lmoist   = .true.

lcoriol = .true.

iradiation = 1

useMcICA = .true.

timerad = 10

rad_longw = .true.

rad_shortw = .true.

dlwtop   = 70.

dlwbot   = 15.

sw0   = 600.

ltimedep = .true.

/

&NAMSURFACE

ps   = 1.016100e+05

thls   = 274.187

wqfactor = 1

wtfactor = 1

albedoav = 0.24

wtsurf   = 0

wqsurf   = 0

isurf   = 2

lsmoothflux = .false.

ustin   = 0.1

/

&NAMMICROPHYSICS

```
imicro      = 2
l_sb        = .false.
l_rain      = .true.
l_sedc      = .true.
l_mur_cst   = .false.
mur_cst     = 0
Nc_0        = 1.000e+08
sig_g       = 1.2
/
&NAMBULKILOMETREICROSTAT
lmicrostat  = .true.
dtav        = 60
timeav      = 600
/
&NAMRADSTAT
dtav     = 60
timeav   = 600
lstat    = .true.
/
&DYNAMICS
llsadv   = .false.
lqlnr    = .false.
cu       = -2.
cv       = -4.
iadv_mom = 5
iadv_tke = 5
iadv_thl = 5
iadv_qt  = 5
iadv_sv  = 5
/
&SUBGRID
ldelta   = .false.
cm       = 0.12
cn       = 0.76
ch1      = 1.
ch2      = 2.
ce1      = 0.19
ce2      = 0.51
/
&NAMBUDGET
lbudget  = .false.
dtav     = 60.
timeav   = 600.
/
&NAMNUDGE
lnudge   = .false.
/
&NAMCHECKSIM
tcheck   = 6
/
&NAMSAMPLING
dtav     = 60
timeav   = 600.
lsampcl  = .false.
lsampco  = .false.
```

```
lsampup    = .false.
lsampbuup  = .false.
lsampcldup = .false.
/
&NAMTIMESTAT
ltimestat  = .true.
dtav    = 60
/
&NAMCROSSSECTION
lcross   = .false.
dtav    = 60
/
&NAMGENSTAT
lstat    = .true.
dtav    = 60
timeav   = 600
/
&NAMFIELDDUMP
lfielddump = .false.
dtav    = 3600
ldiracc   = .true.
/
&NAMSTATTEND
dtav = 60
ltend = .true.
timeav = 600.
```

B.Periods of Stratocumulus Occurrence

Date	Time	Duration	Date	Time	Duration
18-2-2011	0:00	0:12:30	**26-12-2011**	4:50	0:06:00
18-2-2011	16:50	0:07:10	**26-12-2011**	13:10	0:03:50
24-2-2011	20:30	0:04:50	**26-12-2011**	18:10	0:04:10
26-2-2011	0:20	0:03:20	**27-12-2011**	5:40	0:10:00
28-2-2011	4:50	0:14:00	**27-12-2011**	18:30	0:03:10
28-2-2011	19:20	0:03:40	**1-1-2012**	0:00	0:09:30
1-3-2011	0:00	0:03:00	**11-1-2012**	8:20	0:04:00
1-3-2011	4:40	0:05:30	**11-1-2012**	18:40	0:04:00
1-3-2011	12:00	0:03:30	**24-1-2012**	20:10	0:05:00
1-3-2011	20:30	0:03:00	**25-1-2012**	3:10	0:03:10
5-3-2011	13:30	0:03:30	**29-1-2012**	18:20	0:07:00
15-3-2011	4:20	0:03:50	**30-1-2012**	5:30	0:06:30
16-3-2011	7:30	0:03:20	**30-1-2012**	15:00	0:08:40
16-3-2011	19:40	0:17:30	**7-2-2012**	22:40	0:06:10
17-3-2011	22:10	0:07:50	**9-2-2012**	6:20	0:05:40
6-6-2011	21:10	0:08:10	**2-3-2012**	8:50	0:03:00
26-6-2011	0:30	0:03:50	**6-3-2012**	1:50	0:03:00
26-6-2011	4:30	0:05:50	**13-3-2012**	9:30	0:14:10
29-6-2011	6:50	0:03:00	**14-3-2012**	1:50	0:15:20
9-9-2011	8:30	0:04:30	**28-4-2012**	18:10	0:03:00
12-10-2011	19:10	0:04:50	**5-5-2012**	3:10	0:04:50
17-10-2011	7:10	0:04:30	**3-6-2012**	17:10	0:04:00
2-11-2011	4:50	0:05:10	**20-10-2012**	4:30	0:04:20
6-11-2011	7:40	0:04:20	**22-10-2012**	1:20	0:06:10
6-11-2011	12:10	0:04:00	**24-10-2012**	8:50	0:03:10
6-11-2011	23:10	0:05:00	**24-10-2012**	12:10	0:04:30
7-11-2011	8:20	0:06:10	**24-10-2012**	18:50	0:04:00
7-11-2011	17:00	0:10:20	**25-10-2012**	2:00	0:03:10
8-11-2011	4:00	0:04:00	**13-11-2012**	3:30	0:09:20
10-11-2011	12:10	0:23:50	**13-11-2012**	13:20	0:05:00
13-11-2011	6:20	0:05:40	**15-11-2012**	7:20	0:04:40
13-11-2011	12:30	0:04:50	**15-11-2012**	16:00	0:20:50
13-11-2011	21:40	0:04:00	**19-11-2012**	5:10	0:06:50
14-11-2011	2:30	0:03:20	**19-11-2012**	12:20	0:03:00
15-11-2011	7:10	0:03:40	**24-11-2012**	6:40	0:05:10
28-11-2011	23:50	0:08:00	**13-12-2012**	22:40	0:04:10
21-12-2011	11:00	0:03:30	**14-12-2012**	4:00	0:03:00
22-12-2011	15:00	0:04:20			

C.   Initial Profiles

2011-02-18
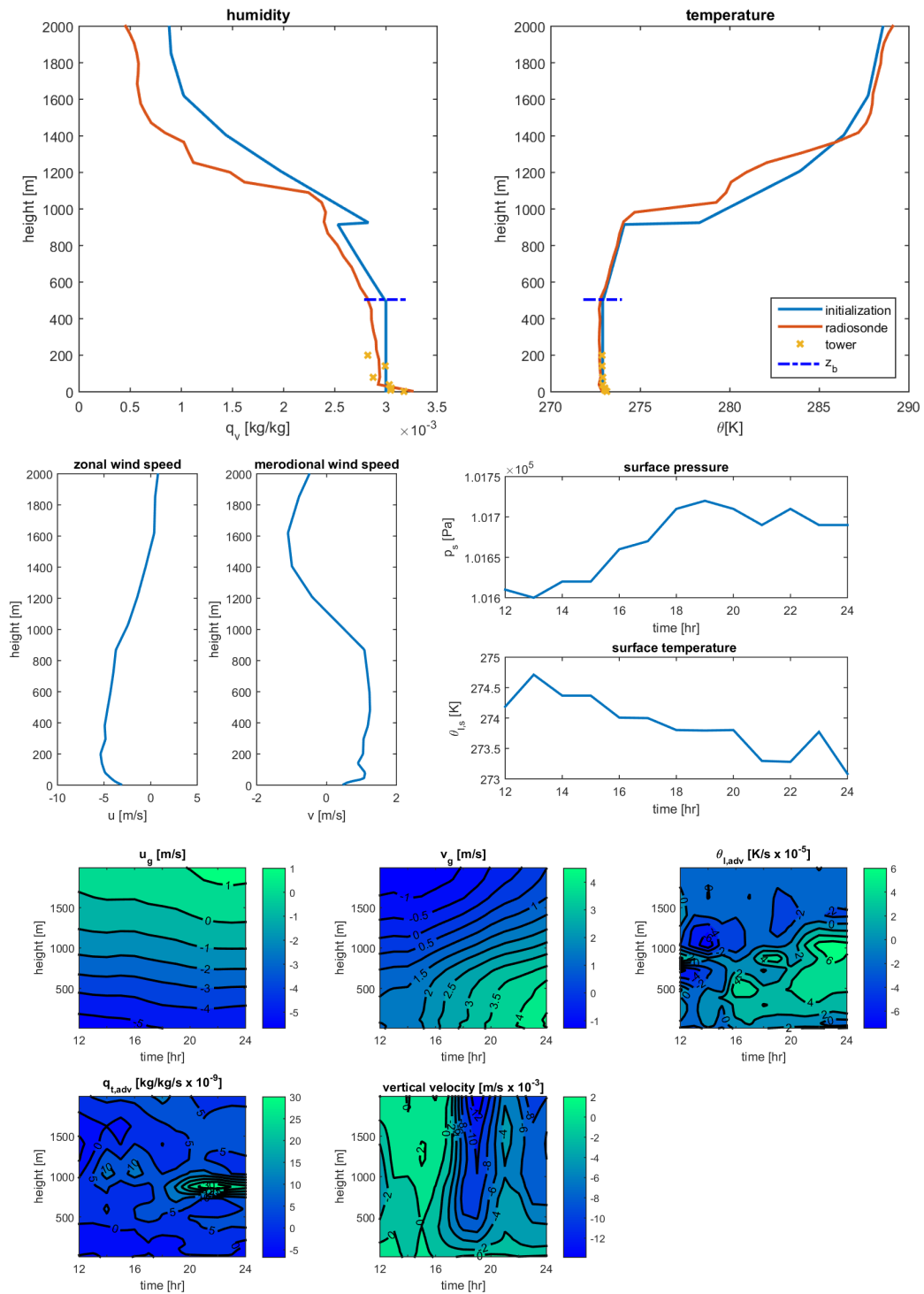
2011-06-19
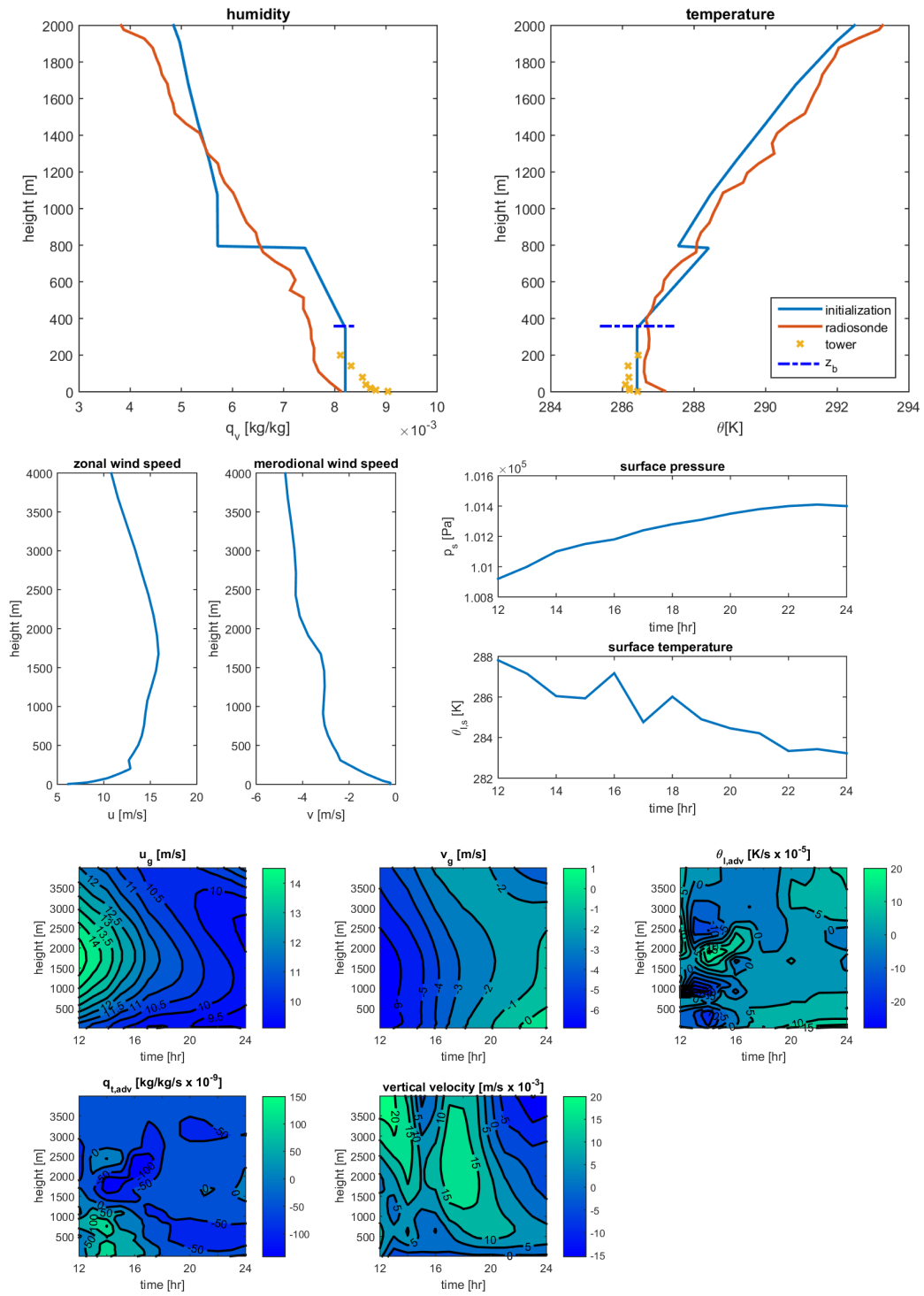
2011-06-25
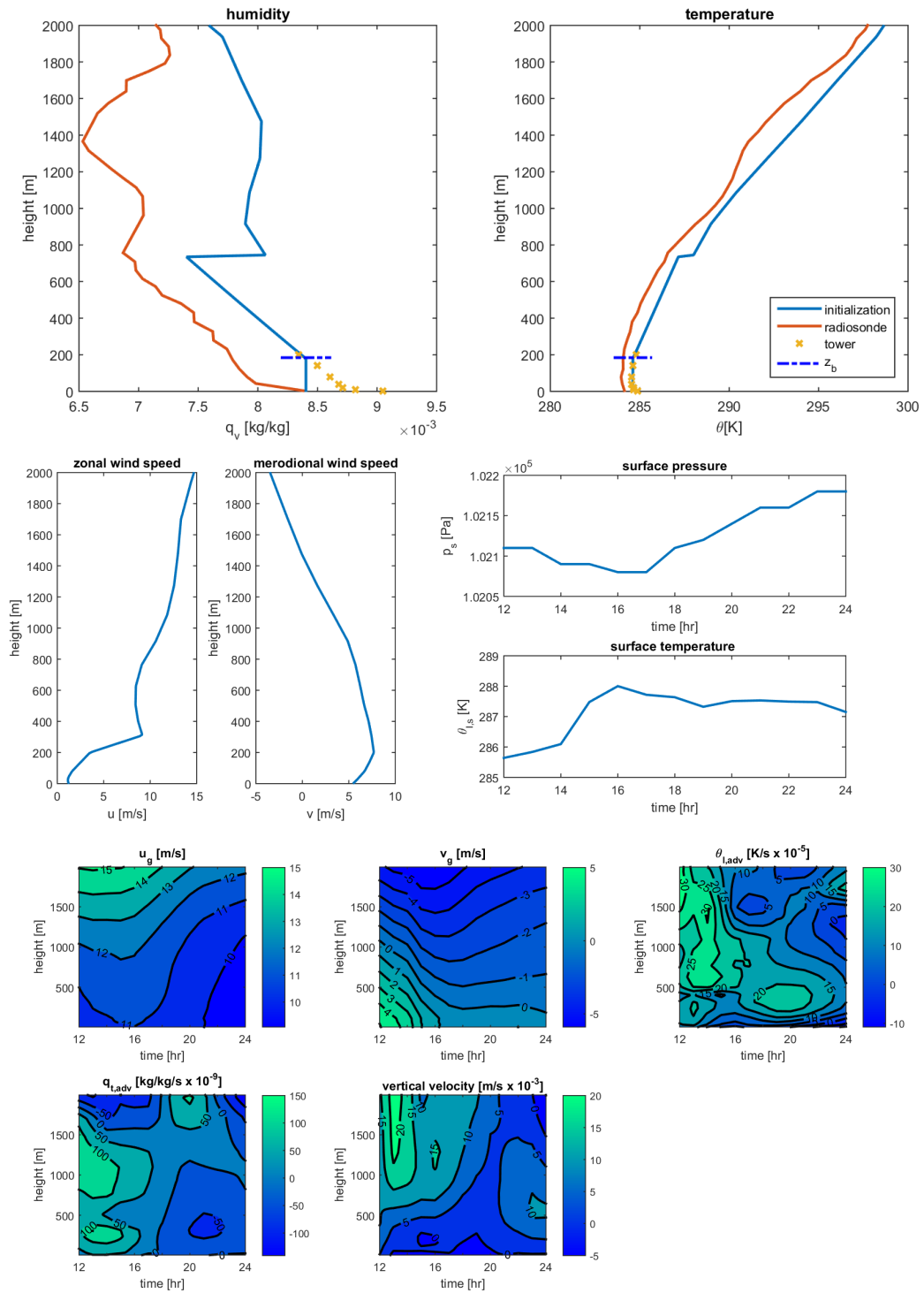
2011-08-11
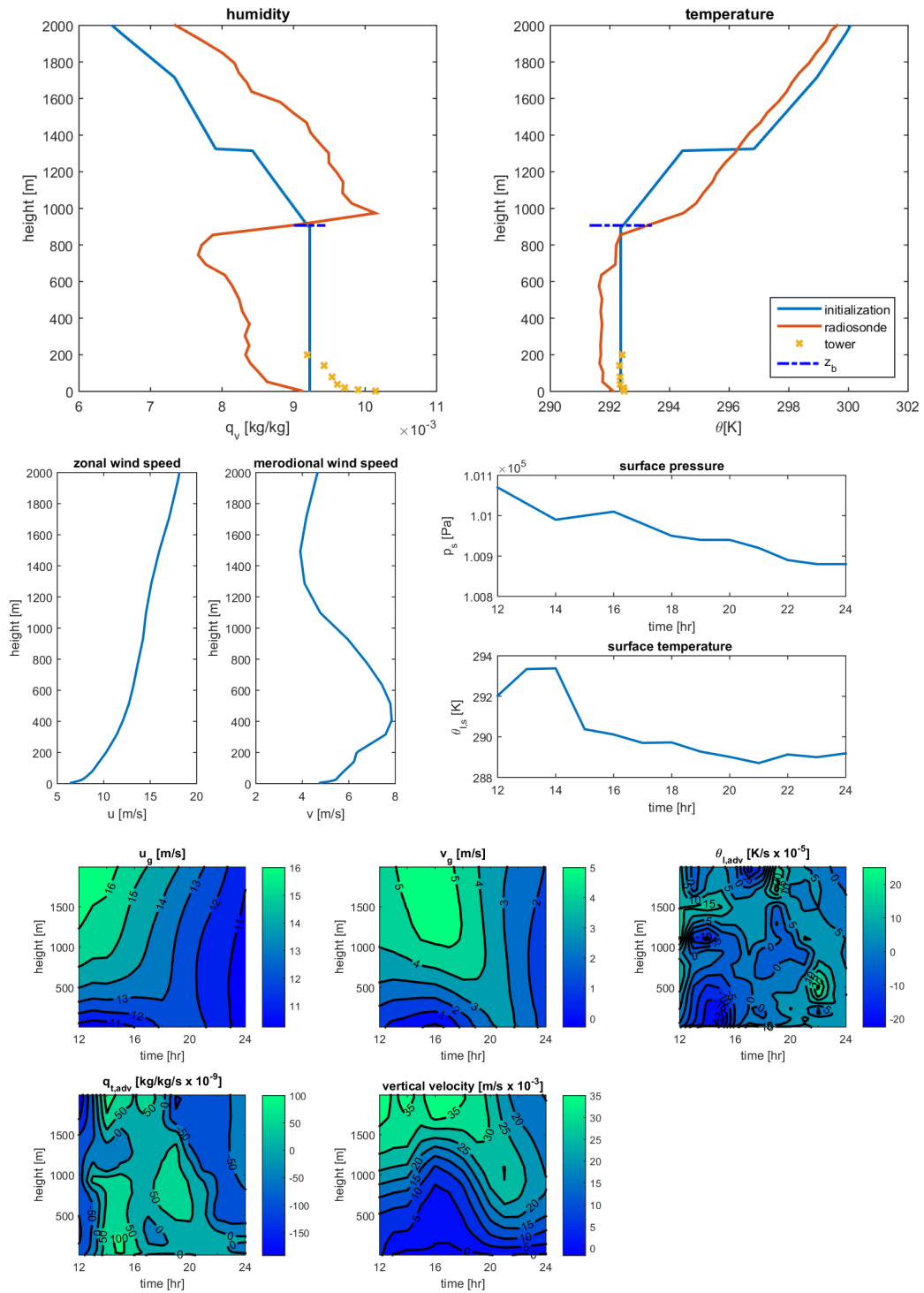
2011-11-06
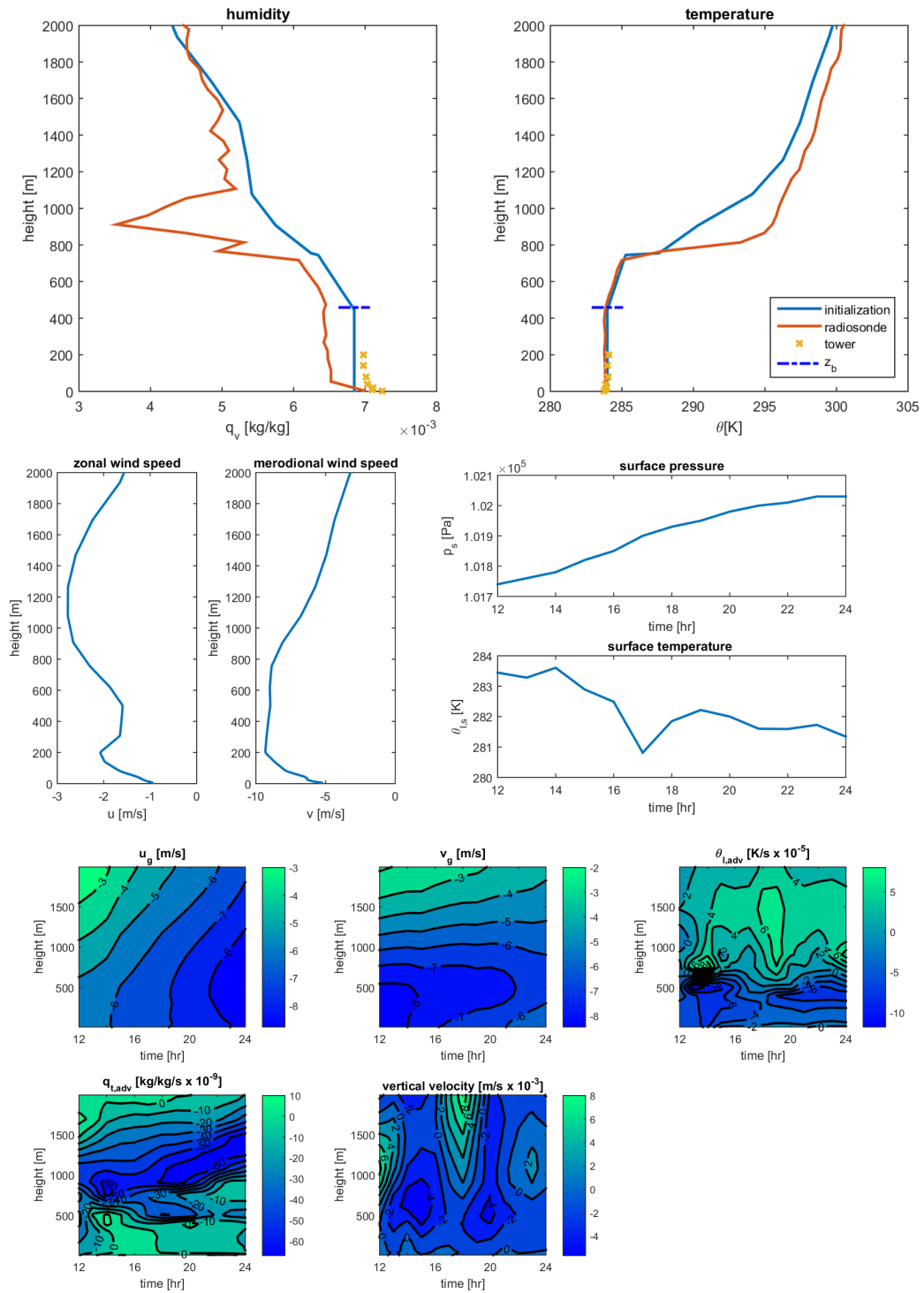
2012-01-29
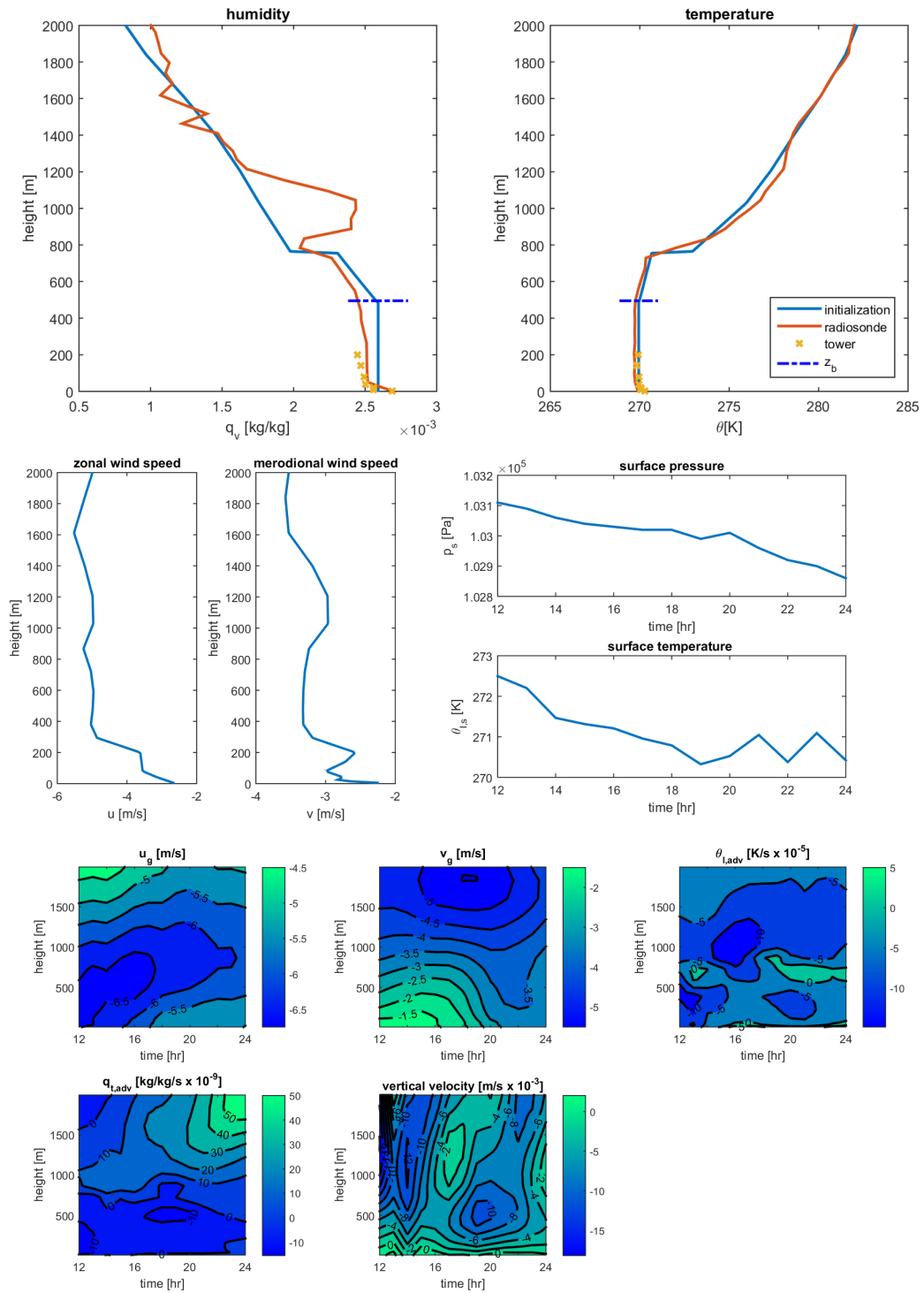
2012-03-13

2012-06-03

2012-07-31